1-1-2015

Electronic and Structural Investigation of Nanocrystal Thin Films Tuned via Surface Chemistry

Elizabeth Ashley Gaulding
University of Pennsylvania, ashley.gaulding@gmail.com

Electronic and Structural Investigation of Nanocrystal Thin Films Tuned via Surface Chemistry

Abstract
Monodisperse colloidal nanocrystals (NCs) provide an opportunity to access physical properties that cannot be realized in bulk materials, simply by tuning the particle size or shape. These NCs form the basis of an artificial periodic table that can be used as building blocks to engineer a new class of solid-state materials with emergent properties. The monodispersity offers a structural advantage for assembling NCs into an ordered superlattice, in addition to a narrow distribution of band energies which in principle promote more efficient transport when the NCs are electronically coupled in a thin film solid after undergoing surface chemistry treatments. However, previous methods for NC assembly have been limiting in their scalability, and while there has been much work in general on the effects of different ligand surface chemistries on semiconductor NC solids, little work has been done to controllably tune the Fermi level and quantify its position in order to promote better device engineering. Herein, we investigate dip-coating as a method by which to scale up NC superlattice assembly. We demonstrate large-area ordering on wafer-scale for both single component and binary nanocrystal superlattices with a diverse set of NC materials and binary crystal geometries. We confirm the extent over which these films are ordered via GISAXS, TEM, and SEM characterization. In the remainder of this work, we study the electronic effects of different ligand chemistry treatments of the NCs. We show that a sequential two step surface treatment can offer increased control over the tuning of the Fermi level and we quantify its positioning and band edge energies relative to vacuum level via a pairing of temperature dependent Seebeck measurements, cyclic voltammetry, and absorption spectroscopy. This provides a reference by which NC devices can be more precisely engineered. Furthermore, we apply that the AC magnetic field Hall effect measurement to a series of common ligand treatments used for making NC devices such as solar cells and field effect transistors to better understand their relative electronic transport properties. We demonstrate this method can be used to determine the hall mobility in these generally high resistivity, low mobility films.

Degree Type
Dissertation

Degree Name
Doctor of Philosophy (PhD)

Graduate Group
Materials Science & Engineering

First Advisor
Christopher B. Murray

Keywords
dip-coating, Hall, nanocrystals, Seebeck, self-assembly, transport

ELECTRONIC AND STRUCTURAL INVESTIGATION OF NANOCRYSTAL THIN FILMS TUNED VIA SURFACE CHEMISTRY

Elizabeth Ashley Gaulding

A DISSERTATION

in

Materials Science and Engineering

Presented to the Faculties of the University of Pennsylvania

in

Partial Fulfillment of the Requirements for the

Degree of Doctor of Philosophy

2015

Supervisor of Dissertation

_____

Dr. Christopher B. Murray
Richard Perry University Professor of Chemistry and Materials Science and Engineering

Graduate Group Chairperson

_____

Dr. Shu Yang
Professor of Materials Science and Engineering, Chemical and Biomolecular Engineering

Dissertation Committee

Dr. Cherie Kagan
Stephen J. Angello Professor of Electrical and Systems Engineering, Materials Science and Engineering, and Chemistry

Dr. Shu Yang
Professor of Materials Science and Engineering, Chemical and Biomolecular Engineering

Dr. Ertugrul Cubukcu
Assistant Professor of Materials Science and Engineering, Electrical and Systems Engineering

ELECTRONIC AND STRUCTURAL INVESTIGATION OF NANOCRYSTAL THIN FILMS TUNED

VIA SURFACE CHEMISTRY

To all my friends and family who have nourished the dreamer in me, challenged the thinker in me, and furthermore convinced me that with their combination, anything is possible.

ACKNOWLEDGMENT

Over the course of my PhD work, my advisor, Prof. Chris Murray, liked to occasionally remind his students that what makes a good scientist is a foundation of three principles (the three "C's" as he called them, passed down from one of his mentors, I believe): Creativity, Care, and Collaboration. It is this last principle for which this paragraph is dedicated. Whether in the lab or outside it, my time at Penn as a researcher was enriched by the minds and personalities that surrounded me, without which this work would not have been possible. First and foremost, I'd like to thank Prof. Chris Murray, who facilitates an open environment in the lab that allows his students to exercise the first "C": Creativity. And also for his generally positive, kind, and cheery Canadian personality, which set an important tone in lab. I would like to thank my fellow labmates, both the senior ones who helped guide me and the younger generation who brought in breaths of fresh air with their enthusiasm. Specifically, I'd like to thank Dong-Kyun Ko who first showed me around the lab and bequeathed to me the electronic instruments which I heavily utilized for my own work. Matteo, who raised not only the fashion standards in lab, but also that of research while always pursuing his "Nature paper" (which became a reality). Ben, whose high expectations of himself and people in general lead those around him to strive higher themselves. Vicky, who wasn't afraid to venture out into expertise outside our lab and whose genuine enthusiasm was addictive. I'd like to thank Prof. Cherie Kagan for her discussions and feedback on electronic transport subjects. SJ, David, Ed, Daniel, and Leo in the Kagan lab, who provided me with many opportunities to discuss and collaborate on the electronics side of the nanocrystal world.

Outside of Penn, I had the privilege of collaborating with Prof. Jason Baxter and his students at Drexel and explore the area of ultrafast spectroscopy. I also thank Dr. Fernando Camino for his guidance in using the Lakeshore AC Hall system at Brookhaven National Lab.

Outside of the country, I had the unique opportunity and pleasure to spend a few months over two summers at the CEA in Grenoble, France working with Dr. Peter Reiss, Dr. Dmitry Aldakov, and Dr. Jérôme Faure-Vincent.

I would also like to thank my friends outside of lab, who enriched my spirit in other ways that contributed to my enjoyment of the PhD experience. First, the MSE crew, as we have always been incredibly supportive of each other from year one as we navigated through classes and quals: Elaine, Jason, Rahul, Ryan, Sharon, and Stella. Secondly, those friends who helped me explore the great outdoors through hikes and climbs, and my inner mind through riveting conversations: Isaac, Kim, Mike, Tyr, and particularly…Nick.

And finally, thank you, Mom and Dad, for encouraging my growing mind as a child and for laying down a path for me through which I could succeed.

ABSTRACT

ELECTRONIC AND STRUCTURAL INVESTIGATION OF NANOCRYSTAL THIN FILMS TUNED VIA SURFACE CHEMISTRY

Elizabeth Ashley Gaulding

Dr. Christopher Bruce Murray

Monodisperse colloidal nanocrystals (NCs) provide an opportunity to access physical properties that cannot be realized in bulk materials, simply by tuning the particle size or shape. These NCs form the basis of an artificial periodic table that can be used as building blocks to engineer a new class of solid-state materials with emergent properties. The monodispersity offers a structural advantage for assembling NCs into an ordered superlattice, in addition to a narrow distribution of band energies which in principle promote more efficient transport when the NCs are electronically coupled in a thin film solid after undergoing surface chemistry treatments. However, previous methods for NC assembly have been limiting in their scalability, and while there has been much work in general on the effects of different ligand surface chemistries on semiconductor NC solids, little work has been done to controllably tune the Fermi level and quantify its position in order to promote better device engineering. Herein, we investigate dip-coating as a method by which to scale up NC superlattice assembly. We demonstrate large-area ordering on wafer-scale for both single component and binary nanocrystal superlattices with a diverse set of NC materials and binary crystal geometries. We confirm the extent

over which these films are ordered via GISAXS, TEM, and SEM characterization. In the remainder of this work, we study the electronic effects of different ligand chemistry treatments of the NCs. We show that a sequential two step surface treatment can offer increased control over the tuning of the Fermi level and we quantify its positioning and band edge energies relative to vacuum level via a pairing of temperature dependent Seebeck measurements, cyclic voltammetry, and absorption spectroscopy. This provides a reference by which NC devices can be more precisely engineered. Furthermore, we apply that the AC magnetic field Hall effect measurement to a series of common ligand treatments used for making NC devices such as solar cells and field effect transistors to better understand their relative electronic transport properties. We demonstrate this method can be used to determine the hall mobility in these generally high resistivity, low mobility films.

TABLE OF CONTENTS

LIST OF TABLES:

LIST OF ILLUSTRATIONS

1 INTRODUCTION

1.1 Unique physical properties and applications for semiconductor QDs

Monodisperse colloidal nanocrystals (NCs) provide an opportunity to access physical properties that cannot be realized in bulk materials, simply by tuning the particle size or shape. These NCs form the basis of an artificial periodic table that can be used as building blocks to engineer a new class of solid-state materials with emergent properties. Furthermore, NCs offer ease in thin film manufacturing via their solution processablity, negating the necessity for ultra clean, high vacuum methods. They provide a gateway to access unique physical phenomena, such as quantum confinement in semiconductors.(*1–4*). This has lead to the exploration of exotic phenomenon such as multiple exciton generation (MEG)(*5–7*) and hot carrier extraction(*8*) in lead chalcogenide NCs for the possibility of breaking through solar cell efficiency barriers. However, arguably the most useful property that quantum dots allow us to tune is the material bandgap. The electronic bandgap is an inherent material property that historically could only be manipulated via material composition, which has its limitations in dopant/alloy solubility before phase separation and requires a precise degree of control. Whereas the bandgaps of cadmium selenide (CdSe) and lead sulfide or selenide (PbS, PbSe) can be tuned over the entire visible and near infrared spectrum, respectively, simply by changing the size of the quantum dot.(*9, 10*) This is possible because of these materials' particularly large Bohr radii, which results in quantum confinement of the wavefunction at NC sizes below 10

nm. The net result is a widening of the bandgap from its bulk value as states from the band edge are removed (**Figure 1.1**).

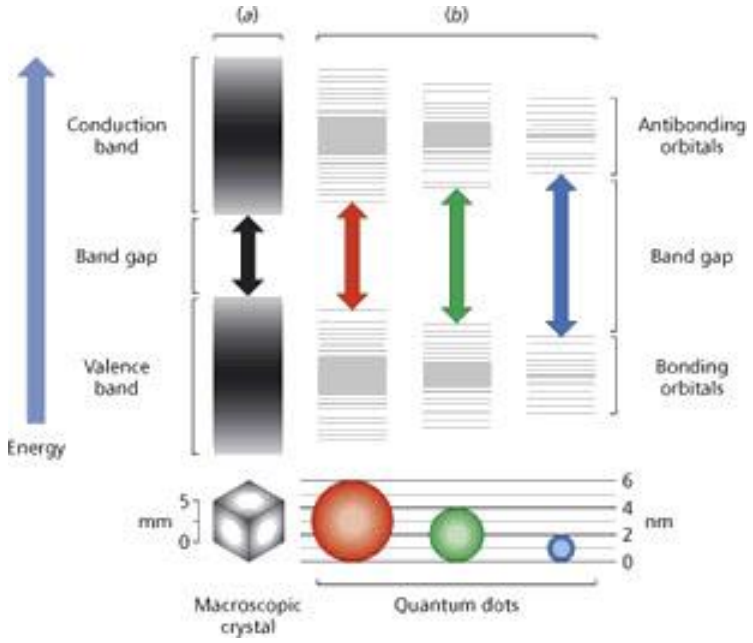

Figure 1.1 *Schematic showing the widening of the material's bandgap from bulk (left) to quantum confined as energy levels are removed from the conduction and valence bands* .(*11*)

The quantization of the edge states results in the emergence of discrete peaks in the absorption spectrum (where the bandgap is typically defined as the energy of the first peak) as well as a sharp emission peak from near the edge of the first absorption feature. As the NC decreases in size, this absorption (and emission) peak shifts towards smaller wavelengths, tuning the optoelectronic properties. A striking example of this is CdSe, which has a bulk bandgap in the red of 1.74 eV. This bandgap can be tuned across the entire visible spectrum, as shown in **Figure 1.2**.

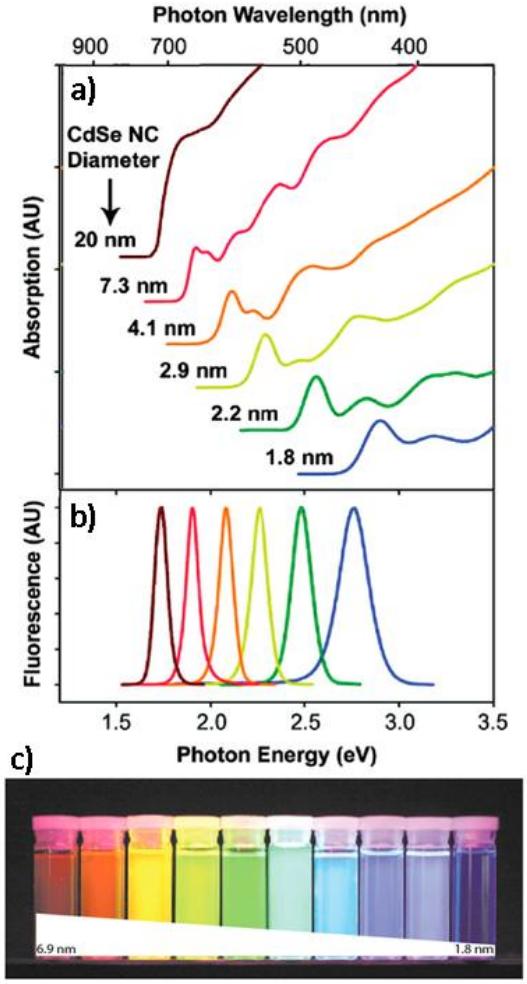

Figure 1.2 *The effects of quantum confinement on CdSe: a) tuning of the absorption band edge, b) emission peaks,*(*12*) *and c) photo of the NC solutions when illuminated with UV light.*(*13*, *14*)

This capability has lead to quantum dots being applied to a wide range of applications such as emitters in today's electronic screens,(*15*) detectors,(*16*) and tags in bioimagery(*17*) just to name a few. **Figure 1.3** shows a solution processed solar cell, selective target imaging of cancer cells, a display screen, and a flexible ring modulator circuit, all made from various quantum dots. The work contained within this thesis is

motivated particularly by the promise of NC quantum dots' integration into electronic devices such as field effect transistors (FETs),(*18–20*) thermoelectric devices,(*21–23*) and photovoltaics.(*24–27*)

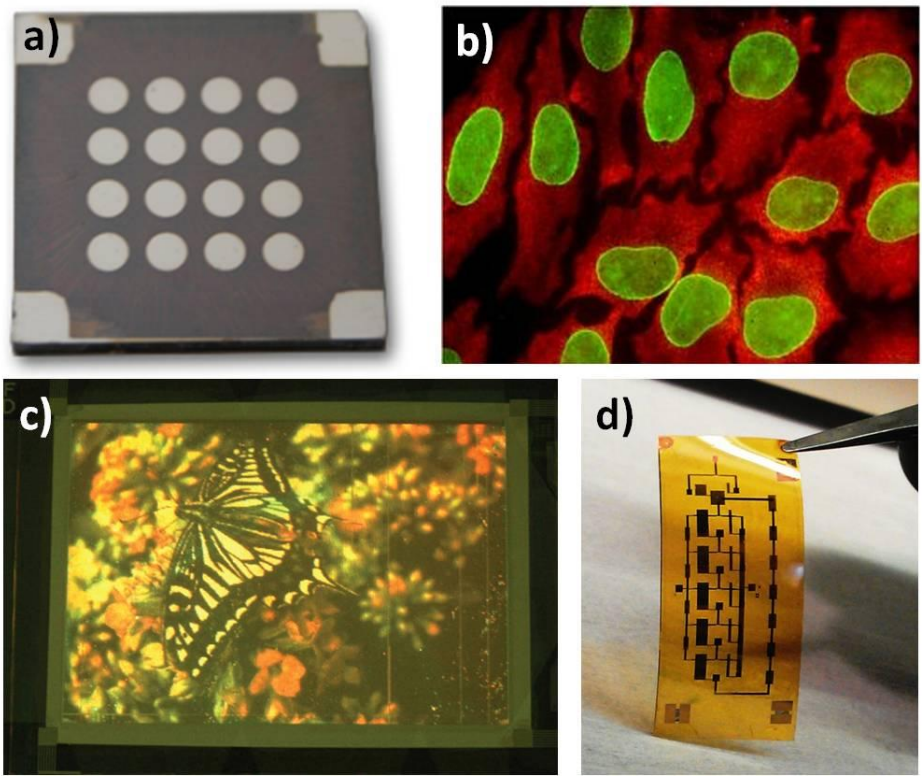

Figure 1.3: *Applications of quantum dots including a) solution processable solar cells,(*28*) b) selective bio-labeling of cancer cells,(*17*) c) enhanced color displays (prototype),(*15*) d) flexible, printable electronics.(*29*)*

For quantum confined NCs, monodispersity is important for uniform energy level coupling without resulting in the washing out of quantum confinement. If the NC sample is too polydisperse in diameter, the first absorption peak is broadened as there is a wider distribution of energy states between individual quantum dots. This, in theory, hinders

carrier transport when the NCs are deposited in a film. Uniform nanocrystal size is also necessary for particle assembly, where the particle size dispersion should ideally be < 10%. Uniform nanocrystal size, plus nanocrystal assembly in the solid phase can be likened to 1) having equivalent atoms in a material and 2) having those atoms arranged in a crystal as opposed to amorphous structure. This is why quantum dot NCs are sometimes referred to as "artificial atoms."

Although we want to capitalize on the effects of quantum confinement, for device applications, we need the NCs to electronically communicate to one another. General synthesis procedures (detailed in a later section) result in NCs whose surfaces are coated with long hydrocarbon molecules referred to as ligands.(*9*, *10*, *30*) These ligands help control nucleation and growth during the chemical reaction that forms the NCs and also helps keep them dispersed in organic solvents such as hexane, octane, toluene, or chloroform so that they can be solution processed. However, these long molecules (typically ~2 nm in length) result in insulating as-deposited films because the NCs are spaced too far apart for electrons to transport from one NC to the next through the film. In order to produce electrically conducting NC films, these "native" ligands are therefore exchanged via surface chemistry, either in solution(*31*–*33*) or solid phase(*34*–*37*) (before or after deposition onto a substrate) for smaller species that bring the NCs closer together. **Figure 1.4** shows the effects of electronic coupling between quantum dots in an organized superlattice.(*38*) For spacing above 3 nm, the energy levels remain discreet, yet

as the NCs are brought closer together, there is some degree of wavefunction overlap that results in energy level splitting and the formation of "minibands."

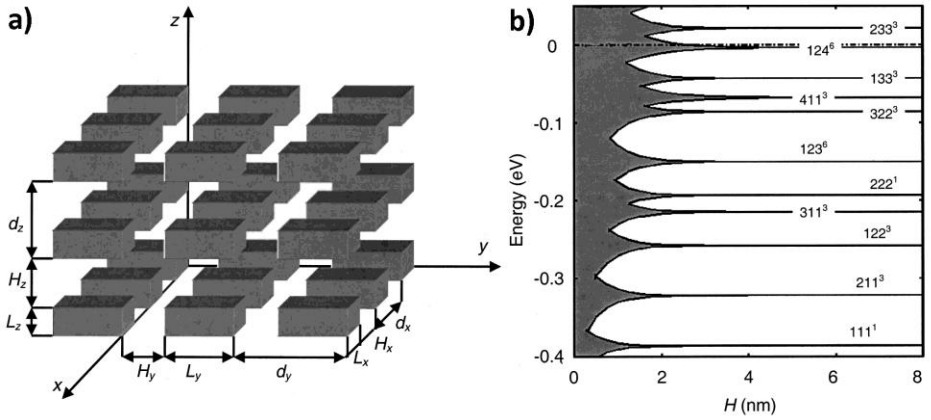

Figure 1.4: *Demonstration of a) quantum dot superlattice and b) miniband formation as the interparticle spacing is decreased for germanium quantum dots.(*38*)*

Figure 1.5 shows the dependence of the transition from localized to delocalized carriers for CdSe and PbSe NC superlattices as a function of both particle size and inter-particle spacing based on theoretical calculations.(*39*) A clever study was performed in which inter-particle NC spacing was modulated by substitution of dithiols with different hydrocarbon chain lengths. The authors found that the carrier mobility within the PbSe NC films increased exponentially as particle spacing decreased.(*40*)

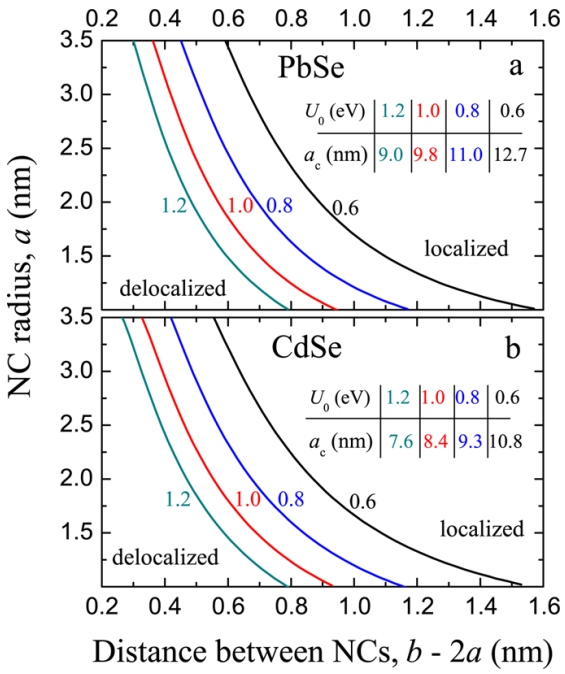

Figure 1.5: *Phase diagram showing the boundary between localized and delocalized carriers as dependent on NC size and inter-particle spacing for a) PbSe and b) CdSe.(*39*)*

There has been a huge breath of research on a diverse set of ligand exchange treatments.(*31–37*) While the ligand length obviously plays an important role in terms of inter-particle spacing, the influence of the chemistry at the actual surface of the NC also greatly affects the electronic properties of the NC solid. This effect is so profound, that different ligands have actually been found to change the dominant carrier type of the NC film. This behavior can at least in part be explained by the ligand's effects on the surface stoichiometry of the nanocrystals.(*19*, *41*, *42*) Not surprisingly, because of the very large surface to volume ratio in NC solids, the surface plays a very important role in dictating the overall properties of the film. Electronic, structural, and optical characterization of

these nanocrystal films prepared using different chemical processes is paramount for their integration into modern electronics.

As alluded to in the theoretical work exhibited in **Figure 1.4** and **Figure 1.5**, having nanocrystal order is beneficial for carrier transport in the same way as crystalline materials are to amorphous ones: order promotes delocalization. Furthermore, in a simpler, geometric sense, it maximizes the number of nearest neighbors between which transfer can occur.(*43*) Increased conductivity and device performance has been demonstrated in ordered PbS(*44*) NC films and PbTe/Ag_2Te(*45*) binary superlattice nanocrystal films compared to their disordered counterparts. And in non-electronically conductive, quasi-quaternary NC films comprised of two core/shell nanocrystals, order into a superlattice clearly shows an enhancement in energy transfer compared to random mixtures as monitored by time dependent photoluminescence measurements.(*43*) However, the process and scale of NC superlattice assembly make it difficult to thoroughly study the promising phenomenon of these materials.

1.2 Summary of Thesis Content

This thesis contains two areas of focus: First, Chapter 0 will focus on NC superlattice assembly and using dip-coating as a new method of NC deposition that allows control of NC order on the nanoscale over wafer-scale areas. We explore different substrate treatments and vary the dip-coating withdraw speed to maximize the degree of NC assembly and control film thickness. We demonstrate that this method can be applied to a library of different NC materials and binary NC superlattice structures. We

extensively characterize the degree of NC order over the entire substrate via transmission electron microscopy (TEM), scanning electron microscopy (SEM), and grazing incidence small angle X-ray scattering (GISAXS). Secondly, Chapters 0 and 4 will examine the effects of ligand surface chemistry on the electronic properties of PbSe NC solid films. We use temperature dependent Seebeck measurements as a form of electronic spectroscopy to quantitatively characterize how these different ligand treatments effect the Fermi level position relative to the transport band. We couple these measurements with cyclic voltammetry to complete the energy level diagram and determine the work function of the NC films, an essential parameter in the design of electronic devices. We also use Hall effect measurements paired with van der Pauw conductivity measurements to determine the NC films' Hall mobility and estimate carrier concentration. Although a classic technique used for investigating the electronic properties of films, the traditional DC Hall measurement has practical limitations when applied to low, mobility, high resistivity materials. The challenges in characterization and defining the physics behind the Hall effect in NC films is similar to those of historically studied amorphous or disordered materials. We overcome the practical limitations of making the Hall measurement by implementing the AC magnetic field Hall measurement technique and discuss our results in the context of existing data and theory for disordered materials.

1.3 Summary of Nanocrystals and Their Synthesis

The work herein focuses primary on lead chalcogenide NCs, particularly for the electronic properties studies. However, one of the motivations of the assembly work was

to demonstrate the diversity of the method for use of various materials. Below is a summary of the syntheses of the materials used throughout this work.

Spherical lead chalcogenide nanocrystals are some of the easiest quantum dots to synthesize in terms of producing a high quality product. Progress over the years has produced syntheses that result in a product with a very narrow size dispersion, in high yield, and tunable in size over a wide bandgap range from about 0.5 – 1.5 eV in PbS(*10*) to 0.5 – 2.1 eV in PbSe.(*25*, *30*, *46*) As with most organic-capped NC syntheses, a metal salt (i.e. lead(II) oxide, lead(II) acetate, or lead(II) chloride), is added to an organic solvent (typically 1-octadecene or squalene) along with a coordinating ligand (typically oleic acid or oleylamine). This solution is heated to 120°C under vacuum for 1 – 1.5 hrs in a 3-neck flask on a Schlenk line to remove air and water. The flask is then switched to nitrogen and the heat turned up or down to the desired injection/nucleation temperature. The solution is held at high temperature for the desired time (anywhere from 30 sec to an hour) before either removing the heat and allowing the solution to naturally cool, or by quenching the reaction by immersing the flask in a water or ice bath (typical for obtaining smaller sizes). The reaction solution is transferred into an evacuated Schlenk tube via cannula and transferred into a nitrogen filled glovebox. The solution is then divided into centrifuge tubes and an appropriate “anitsolvent” (acetone, acetonitrile, or an alcohol), which causes aggregation of the NCs. The NCs are then precipitated via centrifugation and redispersed in the desired organic solvent, depending on the end use (i.e. tetrachloroethylene for spectroscopy, octane for spin-coating, toluene for dip-coating,

hexane for liquid-air assembly and general storage). **Figure 1.6** shows a schematic of this overall process.

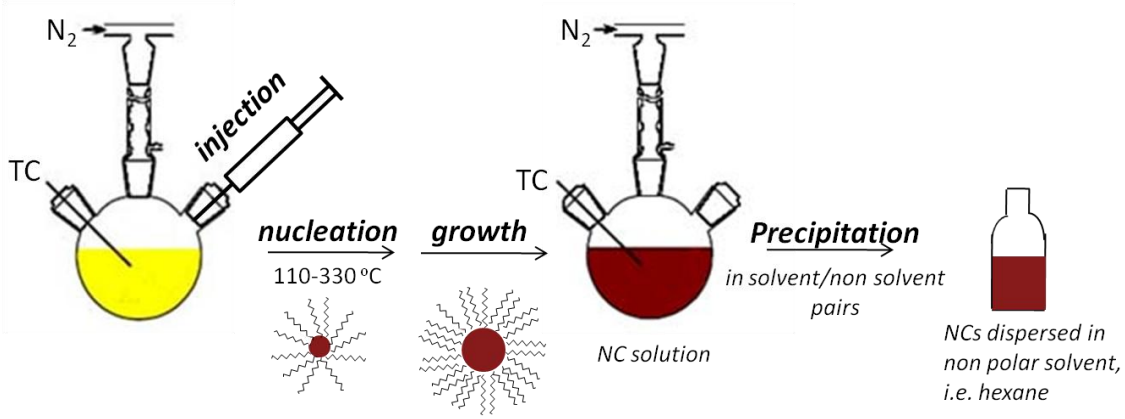

Figure 1.6: *Schematic of a general hot-injection method colloidal NC synthesis.*

As with most quantum dot syntheses, the size of the NCs is determined by a combination of precursor injection temperature, duration of the reaction time, precursor reactivity, and the ratio of the ligand to the metal precursor. **Figure 1.7** shows a series dependence of NC size based on varying both the injection temperature and oleic acid to lead ratio with a reaction time of 30 seconds for all batches.

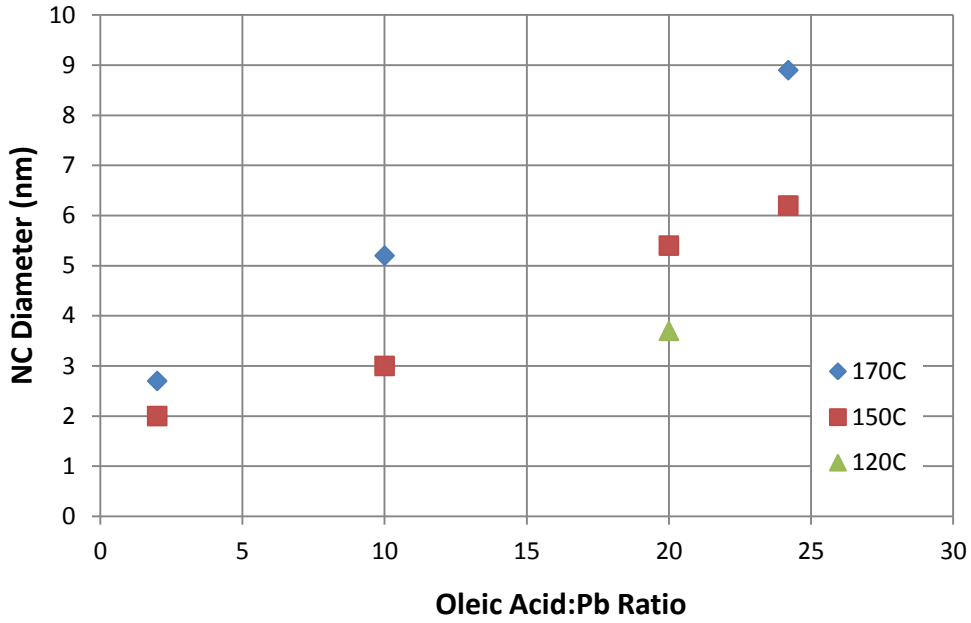

Figure 1.7: *The effects of varying the oleic acid to lead ratio and injection temperature for the Hines et al*(*10*) *PbS synthesis.*

1.3.1 PbS Spheres

Synthesis of PbS NCs used within this work was based on the work of Hines and Scholes.(*10*) For the small, 3.3 nm PbS used in the assembly work, 1.88 g of lead oxide (PbO), 55.2 mL of 1-octadecene (ODE), and 5.2 mL of oleic acid (OA) where added to a 125 mL 3 neck flask and heated at 120°C under vacuum on a Schlenk line for 1.5 – 2 hrs to remove air, water, and form lead-oleate. After this time, the solution turned from a light yellow-orange opaque color of the PbO to a clear, colorless solution. The flask was then put under nitrogen and the temperature decreased to 110°C. At this temperature, 20 mL of a (TMS) and ODE (21 uL TMS:1 mL ODE) solution was rapidly injected into the

3-neck flask. The reaction solution was kept at temperature for 30 sec after which the heating mantle was removed and the flask allowed to cool naturally to room temperature. The solution was then transferred to an evacuated Schlenk tube via cannula and transferred into a nitrogen filled glovebox where it was split into six centrifuge tubes. The NCs were precipitated by acetone (35 mL/tube) and centrifuged at 8000 rpm for 5 min. The resulting pellet was then redispersed with 3 mL of toluene/tube and precipitated again with a 1:1 ratio of acetone:methanol (3 mL:3 mL/tube). The pellet was dispersed again with toluene (3 mL/tube) after which, for the third precipitation, 3 mL of ethanol was added per tube. After this last centrifugation, the NCs were redispersed in a total of 20 mL of hexane and stored in a fridge within the glovebox.

1.3.2 PbSe Spheres

For the electronic measurement studies:

Synthesis of 6.0 nm PbSe nanocrystals used a previously published method with a slight modification to improve yield(*46*, *47*). Synthesis was performed under nitrogen using a Schlenk line system and transfer of the reaction solution to a Schlenk tube *via* cannula. A solution of 892 mg PbO, 3 mL of oleic acid, and 20 mL of ODE was heated to 120 °C and degassed for 1.5 hours under vacuum. Afterward, the temperature was raised to 160 °C, at which 8 mL of 1M TOP-Se combined with 69 µL of diphenyl phosphine (DPP) DPP helps to greatly improve product yield.(*46*) was rapidly injected into the solution. After 80 sec of reaction time, the solution was quenched to room temperature using an ice bath. The nanocrystals were purified within a nitrogen glove box by first adding 2 mL of

hexane to the reaction solution, then precipitating the solution with 1:1 ethanol/butanol and centrifuging at 8000 rpm for 3 min and then redispersing in 4 mL of hexane. The wash process was repeated two more times before the nanocrystals were dispersed in 10 mL of hexane and stored in the glove box in the dark. Before deposition, the nanocrystal solution was dried under vacuum to remove the hexane, and then re-dispersed in octane at the desired concentration.

For dip-coating:

The different sizes of PbSe NCs (4.5, 5.4, 8.2 nm),(*30*, *46*) were achieved by varying the selenium precursor injection temperature and reaction time.

1.3.3 Bi Nanocrystal Spheres

Bi (18 nm),(*48*) spheres followed the Yarema *et al* synthesis with little or no modification.

1.3.4 $CoFe_2O_4$ Spheres

$CoFe_2O_4$ (16 nm)(*49*) spheres followed the Bao *et al* synthesis with little or no modification.

1.3.5 $MnFe_2O_4$ Cubes

For the $MnFe_2O_4$ cubes (13 nm), (*49*) the following variations of the original publication were used: 3.6 g MnFe-Oleate, 1.0 mL oleic acid, 20 mL ODE; a heating ramp rate of 3.3 °C/min to 315 °C; a reaction time of 60 minutes. Size selective precipitation was used to acquire a final dispersion of monodisperse cubes.

1.4 Frequently Used Characterization Methods

UV-Vis – Measurements were performed on either an Analytical Spectral Devices QSP 350-2000 or Cary 5000 spectrophotometer (Agilent Technologies) in transmission mode. Solution measurements were made with nanocrystals dispersed in tetrachloroethylene in a 1 cm quartz cuvette.

FTIR – Measurements were performed on a 6700 Fourier transform infrared (Thermo-Fischer) spectrometer in transmission mode.

WAXS – Wide angle x-ray data was taken using a Smartlab Rigaku system operating at 40 kV, 30 mA, and in PB/PSA mode.

SAXS – Small angle x-ray data was acquired in transmission, under vacuum on a multi-angle x-ray diffractometer system equipped with a Bruker FR591 rotating anode operated at 40 kV and 85 mA, Osmic confocal optics, Rigaku pinhole collimation, and a Bruker HiStar Multiwire detector at a distance of 54.0 cm.

TEM – Routine imagining was done on a JEOL 1400 microscope operating at 120 keV. High resolution imaging was done on a JEOL 2100 microscope operating at 200 keV. TEM samples were prepared on a carbon film, 300 mesh copper grid (Electron Microscopy Sciences).

AFM – Atomic force microscopy (MFP-Bio-3D, Asylum Research) was performed to determine the sample thickness for the van der Pauw and AC Hall calculations.

SEM – Unless otherwise noted, scanning electron microscopy was conducted using a JEOL 7500F instrument at 5 keV, 10 uA emission current, and a probe current of 9.

2 SCALE UP AND STRUCTURAL CHARACTERIZATION OF NANOCRYSTAL SUPERLATTICE ASSEMBLY

2.1 Nanocrystal Assembly Methods

Current methods of NC film deposition have evolved around a need for either large-scale production or small-scale control. Spray-coating(*50*) and spin-coating(*51*, *52*) are used to deposit NCs over wafer-scale areas, but lack control over the nano to micron scale structure. Several methods have been developed over the years to assemble nanocrystals into ordered superlattices such as antisolvent precipitation,(*53*, *54*) depletion attraction,(*55–58*) slow evaporation,(*54*, *59–64*) DNA-mediated assembly,(*65–68*) or by liquid–air interfacial assembly.(*54*, *69–71*) While these techniques have advanced the control over superlattice formation, each poses challenges in scalability and compatibility with device manufacturing processes from either lack of film planarization, film continuity, large material consumption, or deposition speed. Deposition *via* assembly on and transfer from a Langmuir-Blodgett trough can form highly-ordered films over larger areas, but typically forms only a monolayer,(*70*, *72*, *73*) which is generally too thin for many devices. A summary of these techniques to form ordered superlattices are show in **Figure 2.1**.

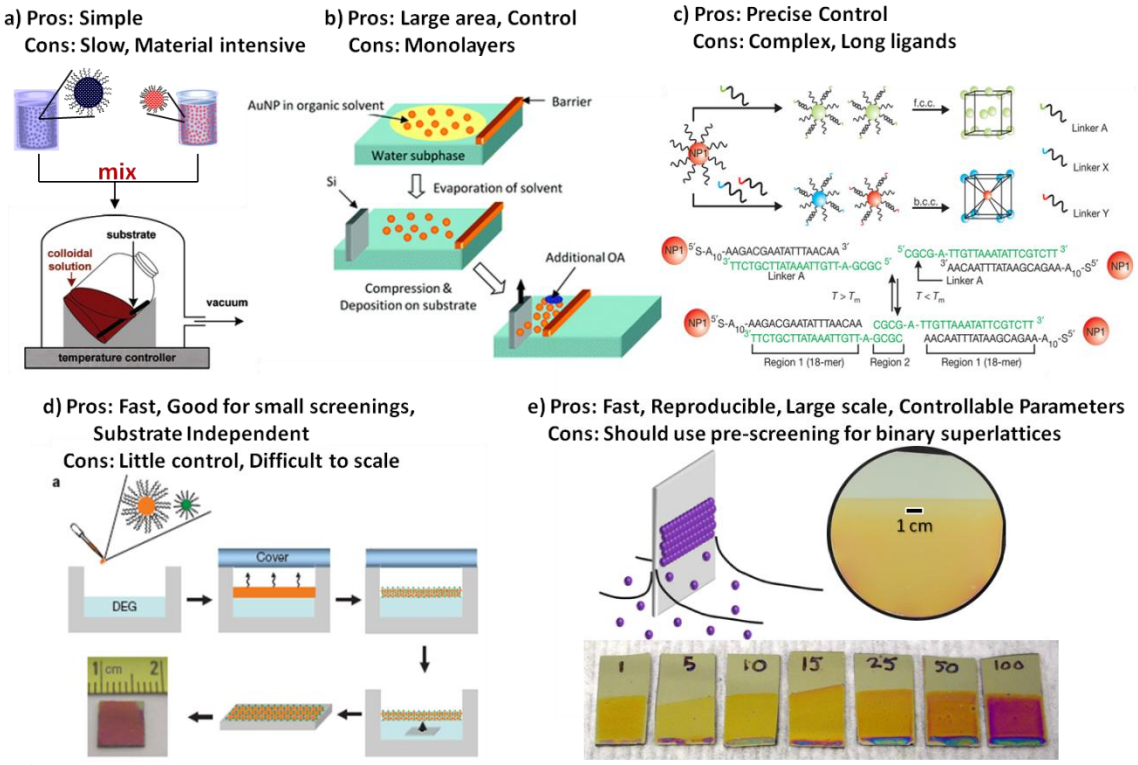

Figure 2.1: *Different methods of NC assembly a) slow evaporation(*59*) b) Langmuir-Blodgett trough (*73*) c) DNA functionalization(*65*) d) liquid-air interface(*71*) e) dip-coating.*

The first step towards combining three-dimensional superlattice order with large-area deposition has been demonstrated by doctor-blading of $Fe_xO/CoFe_2O_4$ core/shell NCs.(*74*) However, there is still a need to develop new methods which combine large-area deposition with nanoscale control.

2.2 A New Approach: Wafer-Scale Assembly of Binary Superlattices Via Dip-Coating

Deposition of NCs from their colloidal dispersions *via* dip-coating offers control over several of the parameters important to film formation. NC organization, film uniformity, and film thickness have the potential to be tuned by varying the solvent, NC concentration, substrate surface treatment, and withdrawal speed. Dip-coating has been utilized previously for deposition of high-quality NC based electronics,(*4*, *24*, *35*, *75*, *76*) but the work to date that explores dip-coating as a method for control over NC superlattice assembly is limited.(*77*, *78*) In chapter, we demonstrate that dip-coating can be used to deposit ordered, polycrystalline superlattices of a variety of NC materials over 4" (100 mm) wafer scales. We show that film thickness can be controlled by varying the withdrawal speed to deposit films from submonolayer to several multilayers. The combination of TEM, SEM, and grazing incidence small angle X-ray (GISAXS) shows that the ordered superlattice structure observed at the nanoscale by microscopy extends over the entire dip-coated area.

Combining different NC materials to form multi-component systems allows for the creation of heterostructures that can be modulated on the nanoscale in films that extend over the macroscale. We present the first demonstration that NC assembly *via* dip-coating can be extended to form several binary nanocrystal superlattices (BNSLs) including AlB_2, $NaZn_{13}$, $CaCu_5$, and $MgZn_2$ structures, exhibiting the versatility of dip-coating for depositing a variety of NC materials and superlattice structures.

Lead selenide (PbSe)(*30*, *46*) was chosen as the pilot material for optimizing the dip-coating conditions because of its particularly narrow size distribution. Different dispersing solvents and substrate treatments commonly used in NC deposition were explored. We investigated (3-mercaptopropyltrimethoxy)silane (MPTS, 95%), hexamethyldisilathiane (HMDS, 98%), and n-octyltriethoxysilane (OTS) as treatments to functionalize glass and thermally oxidized Si wafers. The MPTS treatment was performed by immersing cleaned substrates into a 5 vol% MPTS in toluene solution overnight. The substrates were then rinsed in toluene before sonication in isopropanol for 15 min to break up any polymerized chains. HMDS treatments were performed using a vial of the functionalizing chemical heated at 120°C degrees under static vacuum. OTS treatment was performed using a vial of the functionalizing chemical heated at 120°C degrees under static vacuum. We also investigated alumina-coated silicon wafers prepared by ALD funcationalized by immersion in an 0.005 M N-octadecylphosphonic acid (ODPA) in 2-propanol solution for over 16 h,(*79*) and gold coated Si wafers were treated in 0.05 M Dodecanethiol (DDT, 98%) in ethanol overnight. Octane (frequently used for spin-coating(*41*, *80*, *81*)), hexane (used for liquid-air interfacial assembly(*71*)), and toluene were investigated as solvents for dip-coating. While some degree of assembly was observed in all cases, toluene provided the best balance between solvent drying rate and substrate wetting properties to produce the most ordered grains of nanocrystals (NCs) extending over the largest area. Therefore, we focus primarily on

assemblies deposited from toluene dispersions, which were found to favorably wet OTS-treated surfaces, facilitating long-range, planar order.

Additionally, we studied how dip-coating withdrawal speed affects the film thickness and coverage on the substrate. **Figure 2.2** shows a series of PbSe NC thin films deposited by dip-coating from a NC solution in toluene onto OTS-treated substrates at withdrawal rates of 1, 5, 15, 25, 50, and 100 mm/min. The 100 mm/min withdrawal rate is rapid in comparison to typical dip-coating processes. The film color shows the optical uniformity and the color change reflects thickness-dependent interference as the films become thicker at increasing withdrawal speeds, which is quantified by a shift in the energy of the film reflectance spectrum **Figure 2.2**.The proportional relationship of withdrawal speed to film thickness is likely due to higher withdrawal speeds wicking up a thicker solvent film along the substrate surface. The slowest withdrawal speed of 1 mm/min, is an exception to this trend and results in a film thicker than that formed at 5 mm/min. At the slowest withdrawal rates, the solvent evaporates across the substrate faster than the withdrawal speed as illustrated in **Figure 2.2**.

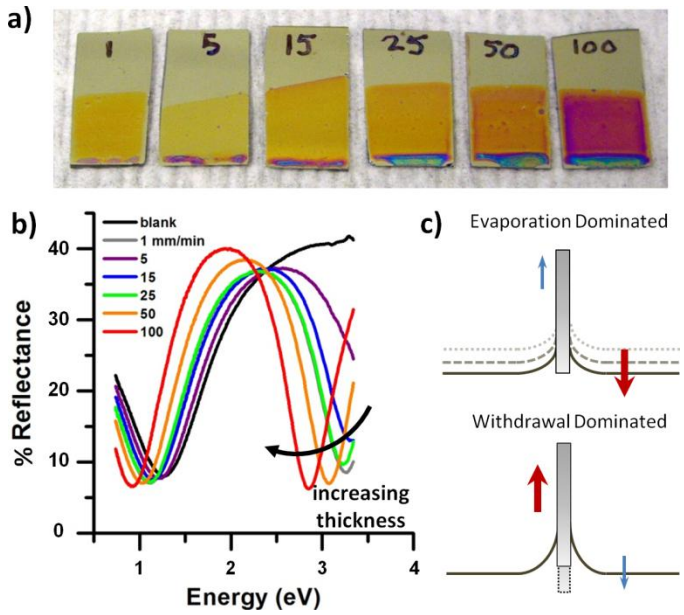

Figure 2.2: *a) Photograph and b) reflectance measurements of PbSe NC thin films deposited by dip-coating OTS-treated, Si wafers with 250 nm of thermal oxide into PbSe NC dispersions in toluene at withdrawal speeds 1 (grey), 5 (violet), 15 (blue), 25 (green), 50 (orange), and 100 (red) mm/min. The reflectance spectrum of an uncoated substrate is shown for comparison (black). c) Schematic illustrating the two different deposition mechanisms: interface movement over the substrate surface* via *solvent evaporation* versus *substrate withdrawal.*

In addition to reflectance measurements used to monitor changes in the film thickness, AFM scans of the PbSe NC films dip-coated at different withdrawal rates were performed as shown in **Figure 2.3.** Films increase in thickness as the withdrawal rates are increased between 5-100 mm/min. In between rates of 1-5 mm/min, the film thickness

increases again, due to the solvent evaporation rate exceeding the withdrawal rate. On average, film roughness is between 1-2 monolayers.

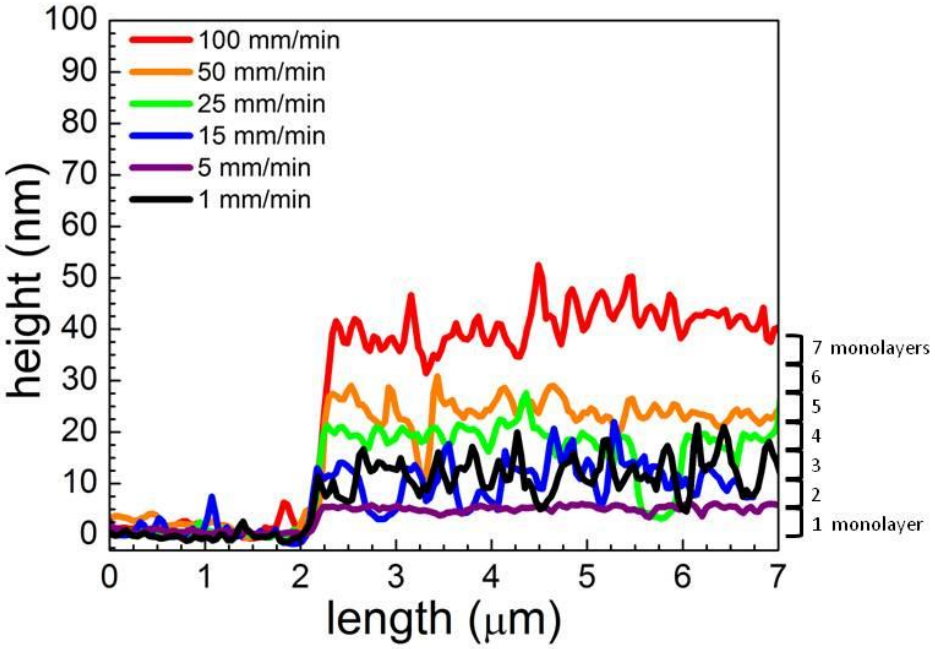

Figure 2.3: *AFM scans of dip-coated PbSe NC films shown in Figure 1a.*

Figure 2.4a shows a superlattice of PbSe NCs formed by dip-coating from a 25 mg/mL toluene dispersion. Using the optimized conditions found in the deposition of PbSe NC superlattices, the dip-coating process was repeated with other NC materials: monodisperse spheres of cobalt ferrite ($CoFe_2O_4$)(*49*) and bismuth (Bi),(*48*) and cubes of manganese ferrite ($MnFe_2O_4$).(*49*) Assembly of NCs into ordered superlattices was confirmed by TEM and SEM (**Figure 2.4a-h**). GISAXS measurements, which probe the film over a ~3 mm^2 area per measurement, confirm that polycrystalline superlattice structures extended over the substrate (**Figure 2.4i-l**). The data taken from several spots of each sample show diffraction patterns commensurate with hexagonally close-packed

structures for the spherical particles or simple cubic packing of cubic particles. Formation of ordered superlattice films from dispersions of semiconductor, magnetic, and semi-metallic NCs of spheres and cubes confirms that the dip-coating method can be used to form ordered arrays from a variety of NCs. The results we report explore only a small fraction of the available parameter space and materials variety that can be accessed.

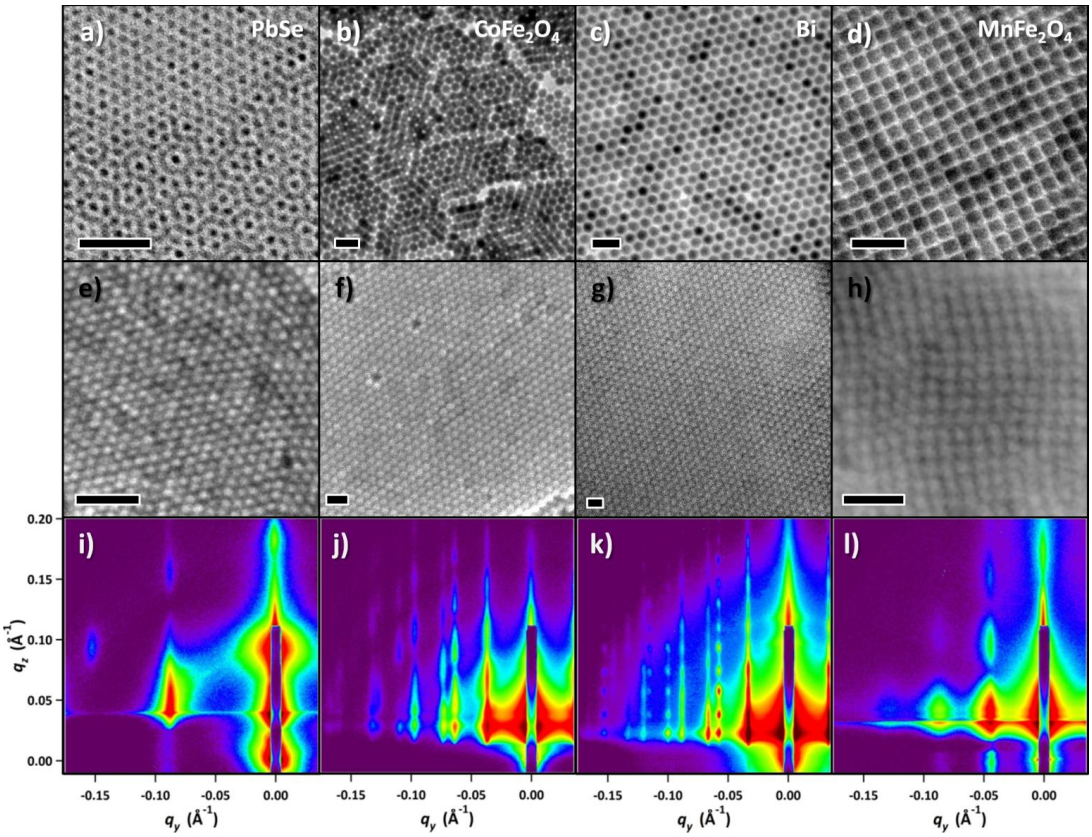

Figure 2.4: *Single component superlattices showing a-d) TEM, e-h) SEM, and i-j) GISAXS of, left to right: PbSe spheres, $CoFe_2O_4$ spheres, Bi spheres, and $MnFe_2O_4$ cubes. Scale bars are 50 nm.*

One of the major advantages of dip-coating is the ability to scale deposition. **Figure 2.5** shows the deposition of a PbSe NC film onto a standard 4" (100 mm) oxidized silicon wafer. The submerged portion of the wafer shows optically-uniform coverage and SEM images taken at several areas across the film show that the ordering is consistent over the entire wafer.

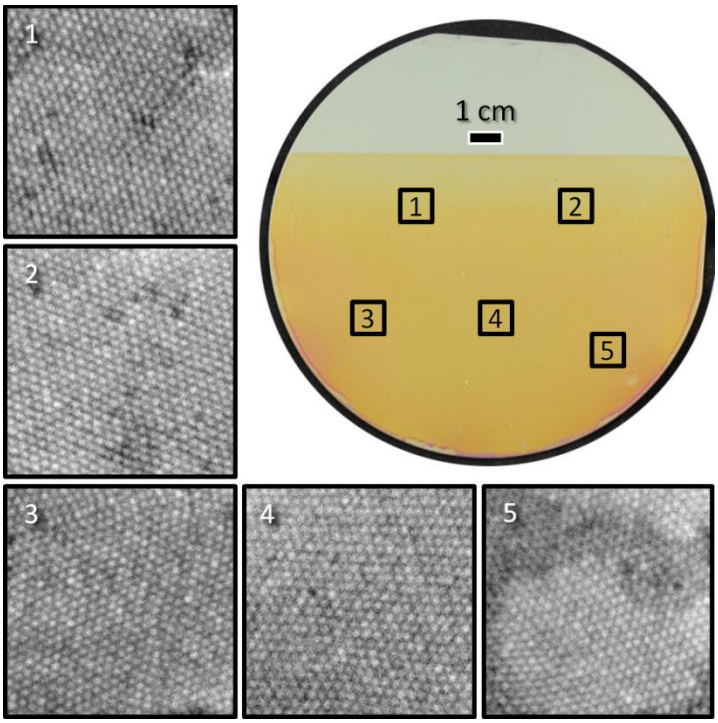

Figure 2.5: *SEM images of different 50,000 nm^2 areas across a PbSe NC superlattice. The file was assembled on a 4" (100 mm) oxidized Si wafer by dip-coating into a toluene dispersion and withdrawing at a rate of 25 mm/min.*

We extended this methodology to the deposition of more complex binary crystal structures. Using PbSe and lead sulfide (PbS)(*10*) NCs, we deposited four BNSL phases: $CaCu_5$, AlB_2, $MgZn_2$, and $NaZn_{13}$. The $CaCu_5$ and $MgZn_2$ phases were formed by mixing

5.4 nm PbSe and 3.4 nm PbS (**Figure 2.6a,b**). An AlB_2 phase was formed with 8.2 nm PbSe and 3.4 nm PbS (**Figure 2.6**). A fourth phase of $NaZn_{13}$ was formed from 8.4 nm PbSe and 3.4 nm PbS (**Figure 2.6d**). All films displayed in **Figure 2.6** were deposited from toluene dispersions at a withdrawal speed of 50 mm/min except for the AlB_2 phase, which was withdrawn at 25 mm/min. All of these phases have been previously observed using at least one other method of BNSL crystallization referenced at the beginning of this manuscript. Previous work has shown, with certain semiconductor-semiconductor NC combinations, that formation of BNSL via slow evaporation appears to be largely entropically driven, in general agreement with the non-interacting hard-sphere model.(*82*, *83*) This can be argued for the AlB_2, $MgZn_2$, and $NaZn_{13}$ phases. However, the hard-sphere model alone cannot be used as an argument for the formation of the $CaCu_5$ phase, which is less entropically favorable than phase separation and close-packed assembly of the single NC components.(*82*, *84*) It is therefore likely that, as with other BNSL structures observed whose formation cannot be described by entropy alone, that particle-particle(*59*, *85*, *86*) and ligand-ligand(*77*, *87*) interaction play important roles in BNSL formation. This fact, along with the island grain nature of the films, suggests that similar dynamics are likely involved in BNSL formation using dip-coating and that a similar range of crystal structures could be accessed. However, the increased control over thin film deposition via variation of the dip-coating speed could lead to possible increased yield of less thermodynamically favorable BNSL structures that are more difficult to access using more traditional methods.

It should be noted that before mixing larger volumes of the two NC dispersions for dip-coating, the different NC combinations were first screened *via* the liquid-air interfacial method on diethylene glycol (DEG) to confirm BNSL formation.(*71*) The mixtures were roughly stoichiometric, with excess of the smaller component. Small volumes of the NCs (10-100 uL) in hexane were mixed at different NC molar ratios to find the most ideal concentration and molar ratio conditions for BNSL formation. 20 uL of these solutions were then dropped and dried on DEG to form films for screening. For example, PbSe and PbS NCs (larger and smaller components, respectively) stock solutions would be used in a series of different volume mixtures (usually varying the volume of one component while keeping the other constant), which results in a series of NC molar ratios. The combinations with the most ordered BNSL assembly over the largest area would then be mixed at larger volumes for dip-coating. The $MgZn_2$ and $CaCu_5$ phases, for example, frequently co-exist together with the same NC superlattices, but the dominance of one phase or the other can be tuned by varying the molar ratio of the two NCs. For the $CaCu_5$ structure, 3.4 nm PbS (21 mg/mL) and 5.4 nm PbSe (27 mg/mL) were mixed at a 1:1 volume ratio, resulting in a 5.3:1 NC molar ratio.

All withdrawal speeds explored (10, 15, 25, 50, 100 mm/min) result in BNSL assembly, again with faster rates resulting in thicker, more continuous films. Further investigation of the $CaCu_5$ structure shows a film with small voids at the grain interstices and crystal grain sizes on the order of ~0.25-5 um^2 **(Figure 2.6e,f)**. GISAXS **(Figure 2.6g)** and transmission SAXS (inset, left) measurements confirm the polycrystalline

$CaCu_5$ crystal structure slightly compressed along the *c*-axis, consistent over the entire substrate. There is no evidence of single-component superlattice impurities, although tiny fractions of $MgZn_2$-type structures can be observed by TEM.

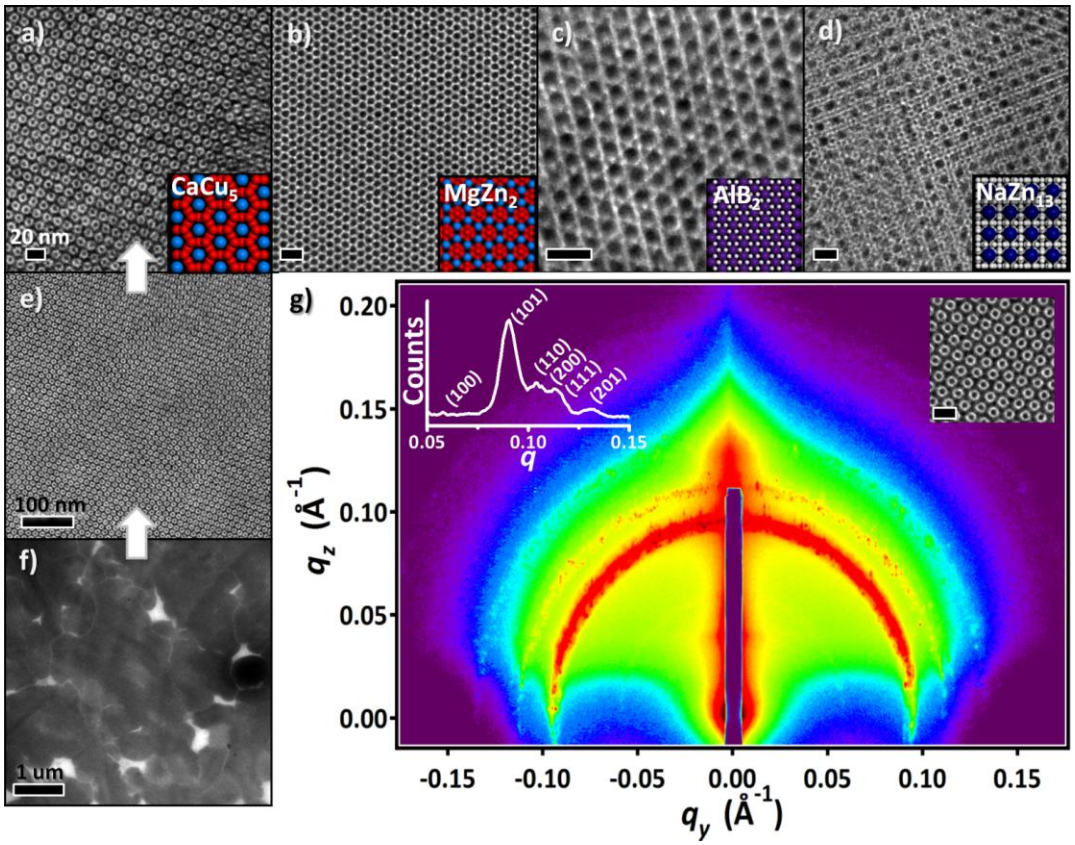

Figure 2.6: *Dip-coated BNSL assemblies of: 5.4 nm PbSe and 3.4 nm PbS a) in a $CaCu_5$ structure and b) in a $MgZn_2$ structure, c) 8.2 PbSe and 3.4 nm PbS in an AlB_2 structure, and d) 8.4 nm PbSe and 3.4 nm PbS in an $NaZn_{13}$ structure. Scale bars are 20 nm. e), f) Lower magnification images of the $CaCu_5$ structure. g) GISAXS of $CaCu_5$ structure with insets of transmission SAXS (left) and higher resolution TEM (right) [scale bar: 20 nm].*

To demonstrate large-area BNSL formation on a substrate relevant for device fabrication, we dip-coated a 1" (25 mm) OTS-treated, oxidized Si wafer into a solution of 4.5 nm PbSe and 3.4 nm PbS. A polycrystalline $MgZn_2$ BNSL film is formed over the entire submerged area as shown *via* SEM imaging **(Figure 2.7a-c)**. The microstructure of the films is mostly continuous. However, fine cracks, or amorphous regions dominated by the excess smaller component, typically define the grain boundaries, as also observed using other BNSL assembly methods.(*43*, *71*, *74*)

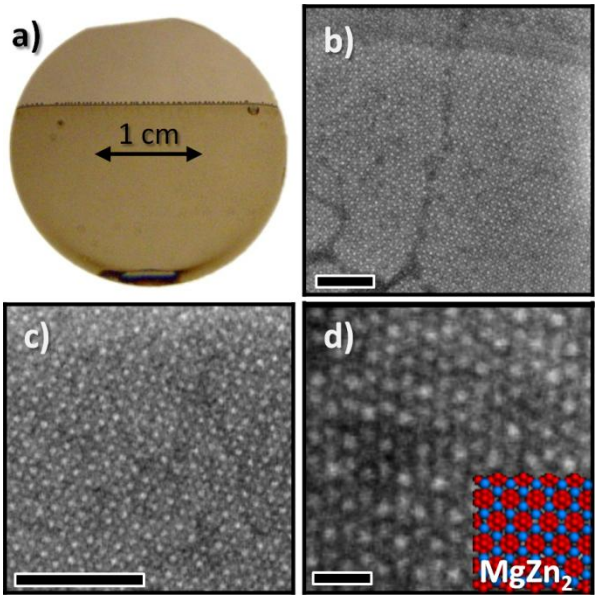

Figure 2.7: *a) Photograph of a 25 mm diameter, thermally oxidized Si wafer dipped into a co-dispersion of PbSe and PbS NCs at a withdrawal rate of 25 mm/min. SEM images showing a polycrystalline $MgZn_2$ phase BNSL. Scale bars are 100 nm for b), c) and 20 nm for d).*

Figure 2.8 and **Figure 2.9** show the film grain morphology at lower magnifications. Increasing the grain size will minimize discontinuities at the grain boundaries and improve the overall film quality. Further optimization by fine tuning parameters such as the large to small NC ratio, ligand concentration, substrate wetting properties, and solvent evaporation rate are likely to lead to larger grain size. The films were predominantly structurally pure, though coexistence of $CaCu_5$ and $MgZn_2$ phases was occasionally observed, as documented previously.

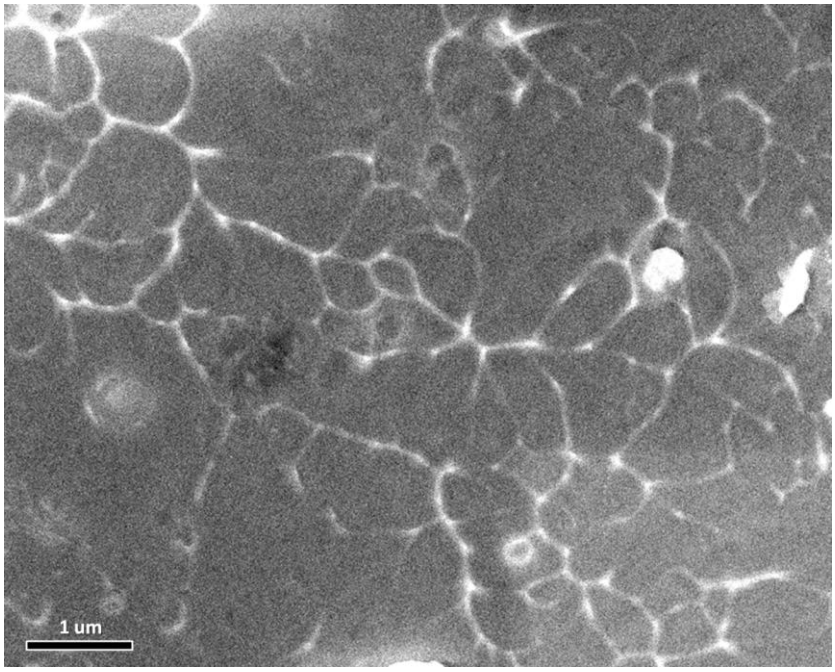

Figure 2.8: *SEM of $CaCu_5$ PbSe/PbS BNSL showing island grain morphology of the structure in* ***Figure 2.6g*** *for which GISAXS was measured.*

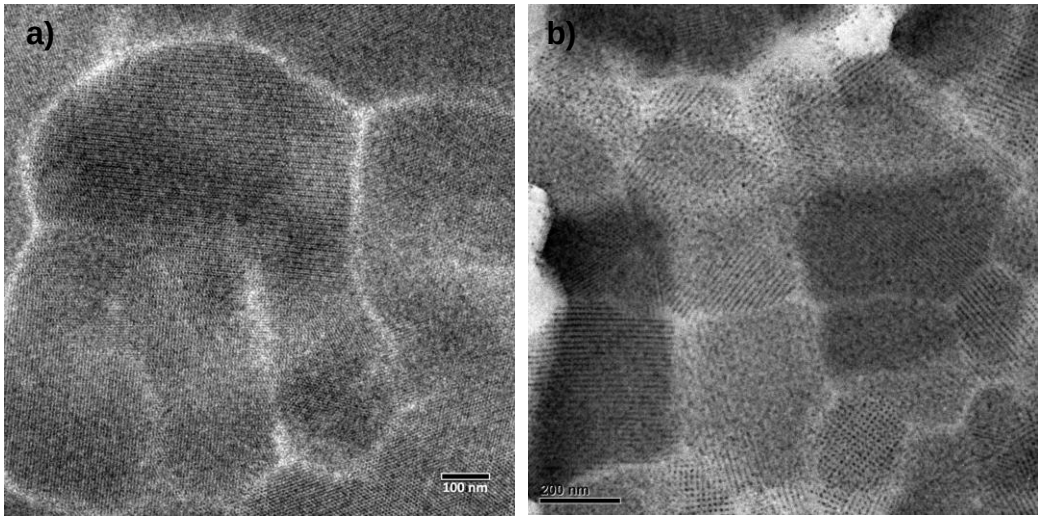

Figure 2.9: *TEM image showing grains of a) $CaCu_5$ structure in different crystal orientations, dip-coated from a solution of 5.4 nm PbSe and 3.4 nm PbS in toluene, b) $NaZn_{13}$ structure dip-coated from a solution of 8.4 nm PbSe and 3.4 nm PbS in toluene.*

In conclusion, we show that long-range ordered single component and binary NC superlattices can be formed *via* the simple process of dip-coating. High quality films are formed by beginning with monodisperse NCs and by dip-coating with the proper selection of solvent, substrate surface treatment, and substrate withdrawal speed. Film thickness can be varied by adjusting the dip-coating withdrawal rate as confirmed by AFM measurements. The crystal structures of the films have been characterized *via* TEM, SEM, and GISAXS measurements, showing formation of superlattice structures over the entire dip-coated area. The studies herein exhibit that dip-coating is a versatile method by which assembly of a diverse set of NC materials and superlattice structures can be achieved at wafer scale using an automated system. Assembly of NCs on these

scales provides an opportunity to better investigate the properties and potential applications of these unique materials.

2.3 Experimental Details Specific to Work Presented in Chapter 2

2.3.1 Dip-coating

Dip-coating was performed using a KSV Instruments, Model 1000 IUD robotic system installed in a nitrogen filled glovebox.

2.3.2 GISAXS

GISAXS was completed at the X9 beamline at Brookhaven National Lab using a 13.5 eV source, MarCCD detector, and a beam width of 200 microns. Data was collected at several points for each sample.

2.3.3 Reflectance

Reflectance measurements were performed using a J.A. Woollam M2000 spectroscopic ellipsometer with a silicon wafer standard.

Additional Methods: Details on chemical synthesis of the nanocrystals can be found in Section 1.3. Additional measurement techniques and chemicals used can be found in the Appendix.

2.3.4 SEM

SEM imaging of the Bi, $MnFe_2O_4$, and $CoFe_2O_4$ NCs was performed on a JEOL 7500F microscope at the Penn Nanoscale Characterization Facility at an accelerating voltage of

5 keV and a working distance of 3.0 mm. Imaging of the PbSe NCs and BNSL films was performed on a Zeiss Ultra-55 at the INAC, CEA Grenoble, France.

2.3.5 TEM

High resolution imaging was done on a JEOL 2100 microscope operating at 200 keV. TEM samples were prepared on a carbon film, 300 mesh copper grid (Electron Microscopy Sciences).

3 USING TEMPERATURE DEPENDENT SEEBECK MEASUREMENTS TO INVESTIGATE HOW SURFACE TREATMENTS TUNE THE FERMI LEVEL IN QUANTUM DOT FILMS

As mentioned in the introduction of this work, surface chemistry plays an important role in dictating the electronic properties of NC solid films. Not only do the ligands help electronically couple the nanocrystals by bringing them closer together spatially, but the ligand's effect on the surface chemistry and stoichiometry of the NCs can influence the material's carrier type, concentration, and mobility. For applications such as photovoltaics, thermoelectrics, and transistors, it is further necessary to controllably tune the doping of the QD solids to form n and p junctions or gradients. The notion of doping NCs is not new and has been explored over the last twenty years. Many efforts have been made to randomly dope in impurity atoms into the internal core of NCs.(*88–90*) This has proven to not be a trivial task due to the tendency of the NCs to either self purify dopant atoms to the surface or concentrate them to the very center in order to minimize energy of the already strained NC internal crystal structure. However, in a QD solid film, the properties of the individual NCs matter less and it is the overall behavior of the collection of QDs in the film that is important for device design.

3.1 Designing Surface Chemistries to Controllably Dope PbSe NC Films

A collaboration that begun in Prof. Cherie Kagan's lab showed that after electronically coupling the NCs together by exchanging them with ammonium thiocyanate (SCN) in actetonitrile, that one could tune the carrier type by adding excess lead (for n-type) or selenium (for p-type) to the NC film. The first exploration of this idea was performed via more traditional evaporative methods, analogous to how intrinsic silicon wafers are doped n- or p-type via vapor phase diffusion of phosphorous or boron into the bulk film. 6 nm PbSe nanocrystals in a 5:1 octane:hexane mixture were spin-coated into a solid film and ligand exchanged with ammonium thiocyanate. A very small amount (<10 angstroms) of either lead or selenium was evaporated onto the film at a very slow rate. This resulted in a switch from ambipolar characteristics in FET measurements, to either n-type for lead rich films or p-type from selenium films, as shown in **Figure 3.1**.

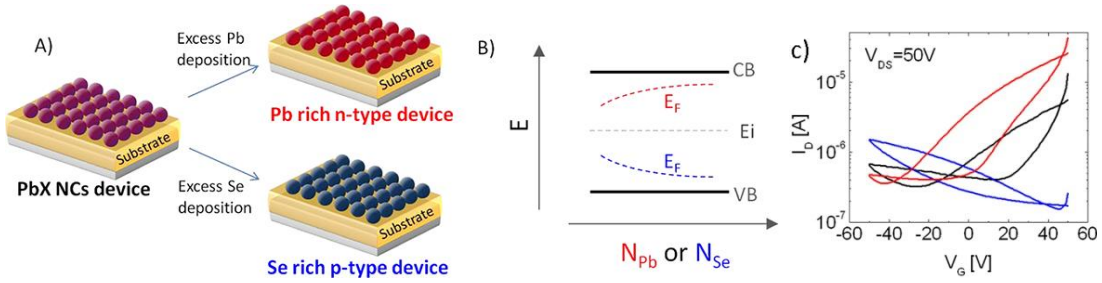

Figure 3.1: *a) Schematic of p- and n-doping of PbSe NC FET devices via thermal evaporation of either lead or selenium, b) its suggested effect on the Fermi level, c) FET characteristics of as deposited (black), Pb rich (red) and Se rich (blue) NC films.(*19*)*

In extension to the evaporative work, a different approach was taken to modify the surface chemistry via solution methods. In this case, spin-coated PbSe films were first

exposed to either sodium selenide (Na_2Se), sodium sulfide (Na_2S), or potassium hydrogen sulfide (KHS), which resulted in chalcogenide rich surfaces as confirmed by inductively coupled plasma atomic emission spectroscopy (ICP-OES), energy dispersive X-ray (EDX), and X-Ray photoemission spectroscopy (XPS). These films show degenerative p-type behavior via FET measurements. The films are then exposed to lead chloride ($PbCl_2$) in oleylamine (OLA) at elevated temperatures between 65-85°C for varying amounts of time. This acts to compensate the degenerate p-doping, with FET measurements first showing less degenerate p-type (1 hr, 65°C), ambipolar (1 hr, 65°C), and finally n-type (12 hr, 65 °C) behavior after $PbCl_2$ treatment(*41*) as shown in **Figure 3.2**. The n-type, Na_2Se → $PbCl_2$ sequentially treated films showed electron FET mobilities up to 4.5 $cm^2/V{\cdot}s$, with greatly increased stability as compared to the Pb evaporative method.

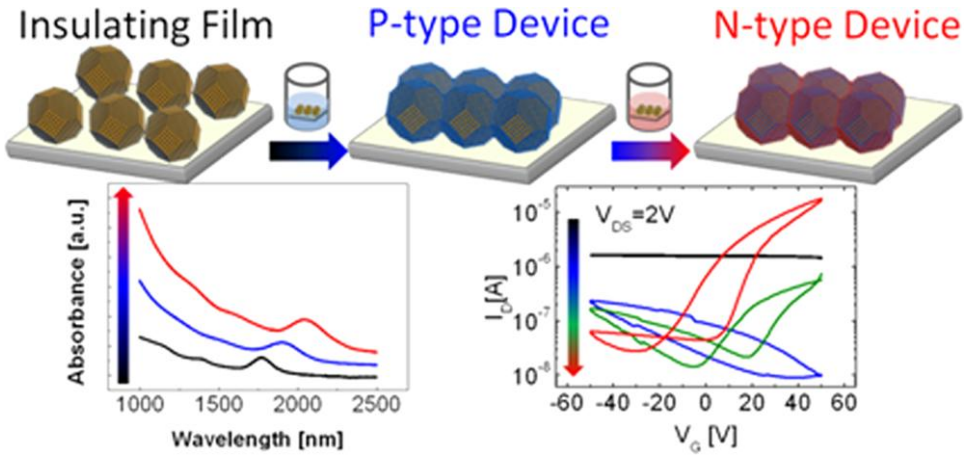

***Figure 3.2**: a) Schematic showing the sequential exposure of PbSe NC films to first a Na_2Se chemical treatment (black, degenerate p-type) followed by a $PbCl_2$ treatment for 1 hr (blue, p-type), 6 hr (green, ambipolar), and 12 h (red, n-type) at 65 °C.*(41)

In a complementary study also in collaboration with the Kagan group, similarly prepared films were studied using time-resolved microwave conductivity (TRMC). This is a measurement using photogenerated carriers and provides information about the carrier lifetime and collective mobility. The mobility values first went down from the Na_2Se only ligand treatment with progressive $PbCl_2$ exposure, then increased slightly after the film transitioned from ambipolar to n-type FET behavior, as shown in **Figure 3.3**. Carrier lifetime of the first time constant continued to decrease with prolonged $PbCl_2$ treatment, from 252 ns (Na_2Se only) to 47 ns (Na_2Se + 24 hr $PbCl_2$ treatment).(*91*)

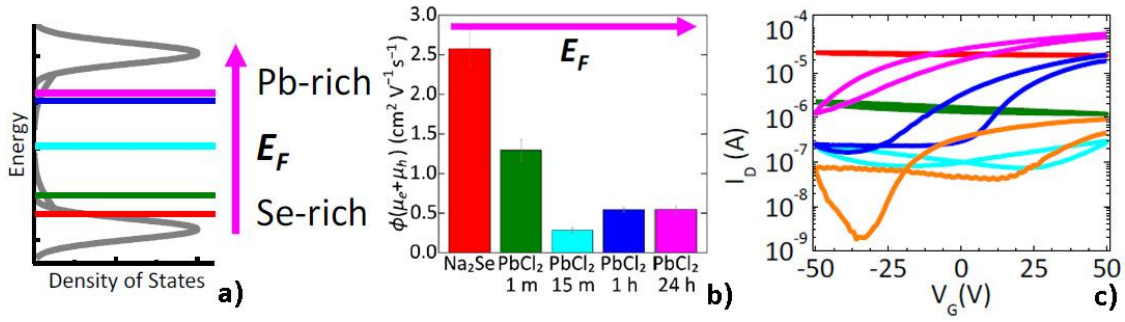

Figure 3.3*: a) Schematic qualitatively describing the shift of the Fermi level after initial Na_2Se treatment followed by different exposure times to $PbCl_2$, b) TRMC mobility values for the specified treatments, c) the complementary FET curves (orange is MPA treated).* *(*91*)*

Though all of these techniques provide invaluable insight into carrier transport, they do not provide quantitative data about where the Fermi level is within the bandgap and where the energy levels are relative to vacuum. Knowing these values, i.e. the material's work function, would provide a reference valuable for electronic device

design. In the following study, we controllably tune the Fermi level of lead selenide (PbSe) QD films from degenerately p-type, back towards the center of the bandgap via simple solid phase surface chemistry treatments of the QD solid films using a variation of the approach described in the above studies. We achieve this by first exchanging the insulating native molecules with ligands that highly p-dope the film, then controlling exposure of the film to a metal salt that acts to compensate dope the QD film back towards the center of the bandgap as suggested by in the studies above. We also investigate two other common ligands used for transistors and solar cells, SCN, and tetrabutylammonium iodide (TBAI). We *quantitatively* monitor this shift of the Fermi level position electronically with temperature dependent Seebeck measurements, which also provide unambiguous determination of the carrier type and whether it's semiconducting or degenerate in behavior.

Fundamentally, doping controls the position of the Fermi level, which can be thought of as a material's chemical potential. It is a parameter necessary to control in semiconductors in order to engineer any junction device. It dictates whether a transistor operates as n or p channel, controls the available open circuit voltage in solar cells, and provides free carriers mobile for conduction in thermoelectric devices. Despite the wide range (0.5-1.9 eV)(*10*, *30*, *46*) tunability of the bandgap in lead chalcogenide QDs due to quantum confinement and fine control over nanocrystal size, controlling the doping density and monitoring subsequent changes in the Fermi level has remained a challenge. Much research has focused on using different surface ligand chemistries, both in

solution(*31–33*) or solid phase,(*34–37*) to remove bulky native ligands on the QD surfaces and produce conductive films. However, many of these surface treatments offer little control over the exact positioning of the Fermi level, which is not only sensitive to the specific ligand chemistry, but also to the ligand concentration,(*92*) treatment time,(*41*, *91*) and even dispersive solvent.(*93*) Furthermore, several of the common ligand treatments leave the QD surfaces very sensitive to oxygen exposure(*19*, *35*, *41*, *94*) resulting in undesirable time dynamics of the Fermi level where it's pushed continuously closer to the valence band due to oxygen doping resulting in highly p-doped behavior. This inevitably leads to degradation of device performance, such as a decrease in open circuit voltage in QD solar cells(*95*) or low on/off ratios in FETs.(*41*) In the last few years, there has been progress in introducing new ligand chemistries that better "passivate" the QD surfaces. These approaches have tended to focus on lead or cadmium metal salt treatments, such as $CdCl_2$and PbI_2 in solar cells(*93*, *96*, *97*) and $PbCl_2$ in FETs,(*41*, *91*) either in solution or post QD deposition. These treatments have been shown to produce more efficient, time-stable QD devices, presumably by decreasing the QD surfaces' susceptibility to oxygen. Capitalizing on the idea that different ligands not only affect the position of the Fermi level, but also the material's electron affinity,(*98*) scientists have pushed the efficiency of QD solar cells by engineering a type of "graded" cell where different layers of QDs within the active layer are treated with different ligands, even purposefully exposing one layer to oxygen to more heavily p-dope the layer.(*28*, *99*) While there has been some work to qualitatively investigate the type of

doping resulting from various ligands via FETs,(*19*, *41*, *91*) the n- or p-type behavior of FETs can be manipulated by more favorably injecting one type of charge via contact metal selection.(*100*) High energy (21.22 eV) measurements via UPS have offered the first effort to quantify the effect of different ligand treatments on QD film energy levels.(*98*)

In this study, we use a series of purely electronic measurements to *quantify* the energy level positions of several common solid exchange ligand treatments. We further expand upon the previously published work described above, first to produce conductive, highly p-doped lead selenide (PbSe) films using sodium sulfide (Na_2S) in methanol, then to compensate dope the material using a second step in which the films are exposed to lead chloride ($PbCl_2$) in ethylene glycol for different time intervals. We quantify how these surface treatments affect the positioning of the Fermi level relative to the transport band via temperature dependent Seebeck measurements.

3.2 Background of the Temperature Dependent Seebeck Measurement

The Seebeck coefficient (*S*), an important parameter commonly referenced in thermoelectric, is informative about the material's electronic transport properties as well. The Seebeck coefficient sign is generally accepted to provide unambiguous determination of the majority carrier type, (+) for holes and (-) for electrons. Larger Seebeck coefficients are associated with low carrier concentration semiconductors where as small coefficients with metals and degenerate semiconductors. A schematic of the physical principle of the Seebeck measurement is shown in **Figure 3.4**. A temperature gradient is

applied across the material, making the distribution of carriers within the material's density of states vary over the length of the sample. In applying this concept to a series of temperature dependent Seebeck measurements, we can use this technique to learn about the transport energy levels within the material.

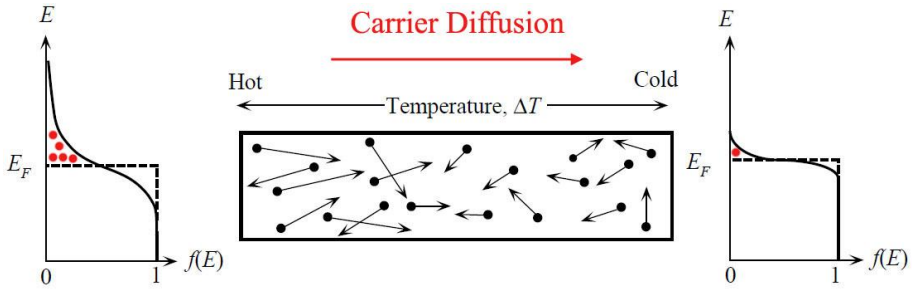

Figure 3.4: *A schematic of the potential across a heated material created by a difference in distribution of the carriers above the Fermi level as the temperature increases. Adapted from Kasap et al.*(*101*)

More specifically, temperature dependent measurements can identify whether the material behaves as a semiconductor ($S \propto 1/T$) or metallic/degenerate ($S \propto T$).(*21*, *101–104*) The Seebeck coefficient is defined as the voltage drop (V_{oc}) over the constant temperature difference (ΔT) maintained across a material Equation 1.

Equation 1

$$S = \frac{V_{oc}}{\Delta T} = -\frac{k}{q}\int \frac{E_T - E_F}{kT}\frac{\sigma(E)}{\sigma}dE$$

Where k is Boltzman's constant, q is the elemental charge, T is temperature, $\sigma(\varepsilon)$ is the energy dependent conductivity, E_T is the transport energy level, E_F is the Fermi level. For semiconductors, Equation 1 simplifies to:

Equation 2

$$S = -\frac{k}{q}\left[\frac{E_T - E_F}{kT} + \frac{\int_0^\infty \frac{\varepsilon}{kT}\sigma(\varepsilon)d\varepsilon}{\int_0^\infty (\varepsilon)d\varepsilon}\right]$$

The first term can be thought of as the energy necessary to activate transport (or carrier's potential energy), and the second term as the additional kinetic energy of the carrier as it travels through the material. The second term is also referred to as the heat of transport constant (*A*). As the Fermi level approaches and enters the band, the first term becomes vanishing and we derive Mott's formula for metals and degenerate semiconductors:

Equation 3

$$S = -\frac{\pi^2 k^2}{3q} T\left[\frac{d(ln\sigma(\varepsilon))}{dE}\right]_{E=E_F}$$

3.3 Studies to Quantitatively Construct an Energy Level Diagram

We are able to complete the layout of the energy level diagram for the various treatments by pairing the temperature dependent measurements with cyclic voltammetry (CV) and to determine the position of the valence band relative to vacuum and optical absorption measurements to determine the material bandgap. We investigate the ligands tetrabutyl ammonium iodide (TBAI), ammonium thiocyanate (SCN), Na_2S, and a $Na_2S/PbCl_2$ dual treatment to control the positioning of the Fermi level. For the $Na_2S/PbCl_2$ dual treatment, PbSe spin-cast films were first exposed to a 30 second treatment of 1 mM Na_2S in methanol, followed by either a 3 min, 15 min, 30 min, or 24 hours at 85°C treatment with 50 mM $PbCl_2$ in ethylene glycol. These are commonly used

ligand treatments for FETs(*19*, *41*) and solar cells.(*97*, *105*) Temperature dependent Seebeck measurements reveal p-type ($S > 0$) carrier transport for all treatments, and semiconducting ($S \propto 1/T$) behavior above 220K (**Figure 3.5a**). There is an apparent turnover from semiconducting to degenerate behavior for SCN, Na_2S, and Na_2S followed by a mild (3 min) treatment of $PbCl_2$ as the temperature decreases, which will be discussed in further detail below. Unfortunately, the high film resistivity resulting from the 24 hour at 85°C $PbCl_2$ treatment prohibited its temperature dependent Seebeck measurement. **Figure 3.5b,c** shows the temperature dependent conductivity measurements of the films.

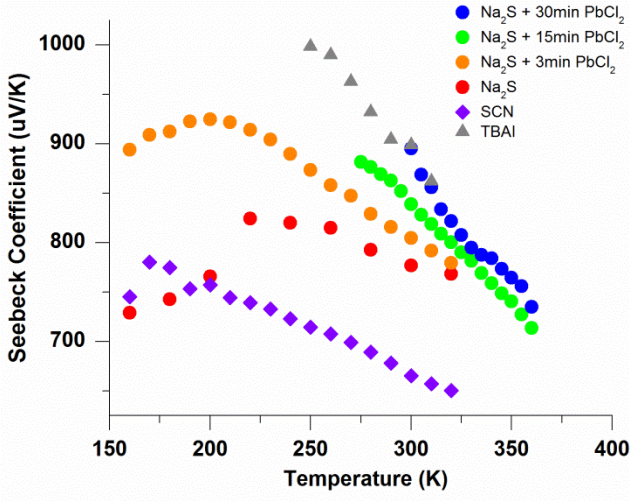

Figure 3.5: *Temperature dependent Seebeck measurements of the various ligand treatments: (red) Na_2S, (orange) Na_2S + 3 min $PbCl_2$, (green) Na_2S + 15 min $PbCl_2$, (blue) Na_2S + 30 min $PbCl_2$, (pink) Na_2S + 24 hrs at 85°C $PbCl_2$, (purple) SCN, (grey) TBAI.*

The turnover behavior of the temperature dependent Seebeck measurements for the SCN, Na_2S, and Na_2S + 3 min $PbCl_2$ treated films is peculiar and was an unanticipated observation. It is believed that this behavior could be contributed to the Fermi level being pushed into the band edge due to temperature dependence of the bandgap. Opposite that of most materials, the bandgap of the lead chalcogenides shrinks with decreasing temperature ($E_g \alpha T$). SCN and Na_2S are two of the more conducting ligand treatments that result in some of the highest reported FET mobilities in PbSe NC films,(*19, 41*) This is generally attributed to high p-doping of the material. If the Fermi level of these PbSe NC films is close enough to the band edge, a significant enough decrease of the bandgap could further push the Fermi level towards and even into the valence band, resulting in degenerate behavior (**Figure 3.6**). The change in bandgap for bulk lead selenide is 0.57 meV/K, or by 57 meV from 300 – 200K (Δ100 K). Studies of PbSe nanocrystals have shown there to be a dependence of the optical bandgap proportional to temperature, which becomes less pronounced as the NCs decrease in size and eventually becomes inversely proportional when the NCs become 2.3 nm in diameter.(*106, 107*) The largest diameter PbSe NC reported in these studies is 5.1 nm, which shows a temperature dependence of ~10 meV/100 K.(*106*) The NCs used in this work are ~6 nm in diameter. Therefore, dE_g/dT would be expected to be even greater than that of the 5.1 nm NCs and is a plausible explanation for this interesting behavior given the calculations of the Fermi level energies reported below.

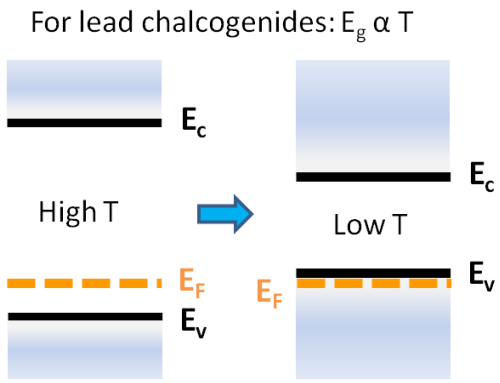

Figure 3.6: *Schematic demonstrating the shrinking of the bandgap with decreasing temperature that could explain the semiconducting to degenerate switch in behavior.*

In order to calculate the energy difference between the transport and Fermi levels (E_T-E_F) for semiconducting materials, it is clear from Equation 2 that we can plot the Seebeck coefficient versus inverse temperature. From a linear fit of the data, we determine E_T-E_F from the slope, while the y-intercept gives us the heat of transport constant, *A*. The semiconducting (S α 1/T) portion of the curves in **Figure 3.5** are plotted accordingly in **Figure 3.7a**.

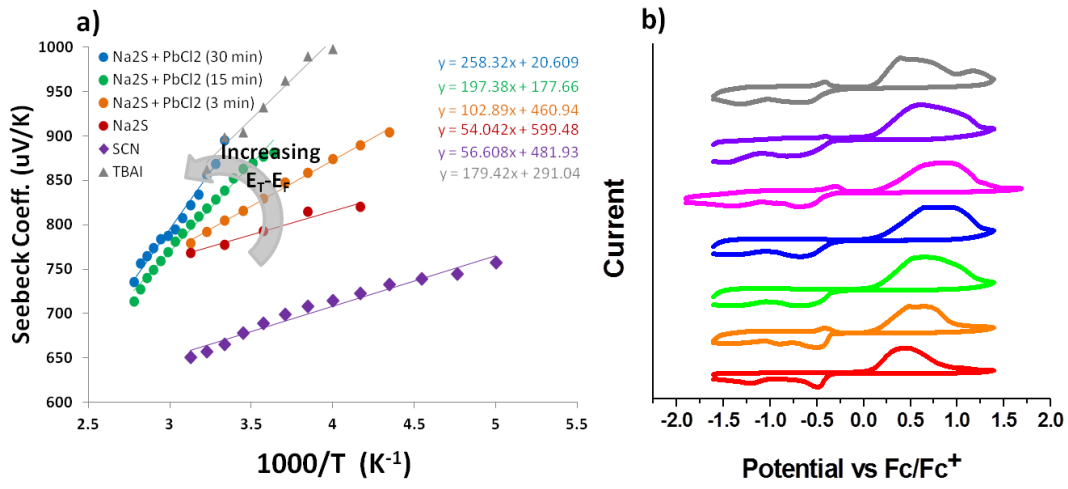

Figure 3.7: *a) linear fits of the Seebeck coefficient vs. inverse temperature from which* E_T-E_F *and the heat of transport coefficient (*A*) can be derived. b) Cyclic voltammetry of the surface treatments. Color coding is consistent between both plots: (red)* Na_2S*, (orange)* Na_2S *+ 3 min* $PbCl_2$*, (green)* Na_2S *+ 15 min* $PbCl_2$*, (blue)* Na_2S *+ 30 min* $PbCl_2$*, (pink)* Na_2S *+ 24 hrs at 85°C* $PbCl_2$*, (purple) SCN, (grey) TBAI.*

SCN and Na_2S only treatments show the shallowest slopes, translating to the most highly p-doped out of the treatments explored, where as TBAI shows a steeper slope, indicating its Fermi level is more towards the mid-gap. The most interesting phenomenon is the clear dependence of slope on the increasing $PbCl_2$ treatments from none (Na_2S only) to 30 min. This trend from shallow to steep slope indicates a type of "compensation doping" effect, nearly degenerate to intrinsic, from $PbC1_2$ treatment. The E_T-E_F (slope) and *A* (y-intercept) values derived from the linear fits of **Figure 3.7a** are listed in **Table 1**.

Ligand	E_T-E_V (meV)	E_k (meV/K)
TBAI	179.42	291.04
SCN	56.61	481.93
Na_2S	54.04	599.48
Na_2S + $PbCl_2$ (3min)	102.89	460.94
Na_2S + $PbCl_2$ (15 min)	197.38	177.66
Na_2S + $PbCl_2$ (30 min)	258.32	20.609

Table 1: *Showing the slope (*E_T-E_F*) and y-intercept (*A*) extracted from a linear fit of the plots in* ***Figure 3.7a****.*

The numerical values reiterate what is already apparent in the plot: The position of the Fermi level relative to the valence transport band edge increases, from 54.0 to 258 meV, with increasing $PbCl_2$ treatment. SCN has a Fermi level position similar to Na_2S (56.6 and 54.0 meV, respectively), and TBAI is less p-doped (E_T-E_v = 179.4 meV) in between the 3 and 15 min $PbCl_2$ treatments. This provides quantitative evidence for discreet control over the doping of NC films. Furthermore, $PbCl_2$ treatments have demonstrated respectable long term stability, making it a potential improved substitute for TBAI treatment.(*41*)

Although E_T-E_F provides quantitative information about the degree of doping and energy transport within the NC film, coupling this with CV measurements provides on an absolute scale where the band edges are relative to vacuum. This is more valuable from a device engineering perspective because ultimately it is the material's work function that determines band-bending within a heterojunction device. CV has previously been shown

as a useful tool in determining the band edges of NC films.(*100*, *108–110*) The measurement is done air-free in a non-aqueous electrolyte solution within a nitrogen filled glovebox. The CV curves (**Figure 3.7b**) are normalized to the ferrocene/ferrocenium redox couple, which has a known value of -4.8 eV relative to vacuum. Details of the measurement setup are outlined in Section 3.4.4. In theory, the conduction and valence bands of the NC film can then be calculated relative to vacuum level based on the reduction/oxidation peaks. But because the oxidation peak is highly unstable,(*100*) we use the value of the reduction peak for the absolute conduction band energy, then use the optical bandgap to place the valence band. With these three measurements: temperature dependent Seebeck for E_T-E_F, CV for the absolute energy of the conduction band, and optical bandgap to position the valence band, we can now piece together the energy level diagram resulting from the various surface treatments on an absolute scale. This diagram is presented in **Figure 3.8**.

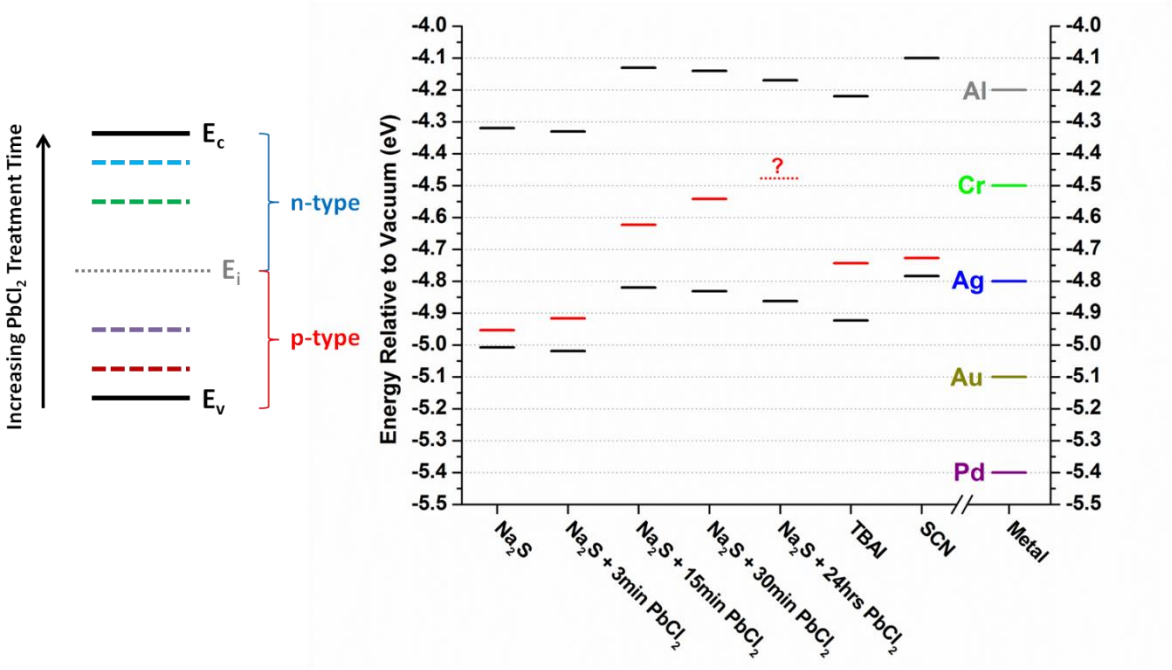

Figure 3.8: *The complete, absolute energy diagram of the PbSe NC films with various surface chemistry treatments compiled from temperature dependent Seebeck, CV, and absorption measurements.*

The relative positions of the band edges for SCN and TBAI are in agreement with eachother from previous reports.(*98*, *100*) The positioning of the Fermi level within the bandgap shows p-type, in agreement with the Seebeck coefficient sign, with the Na_2S + 30 min $PbCl_2$ treatment coming very close to the center (“intrinsic”) position. As mentioned previously, we could not achieve a temperature dependent Seebeck measurement of the 24 hr $PbCl_2$ treated film. This was due to its high resistivity, but could also be because of the Fermi level being very close to the true intrinsic value. If this were the case, there would only be a very weak or non-existent Seebeck effect because holes and electrons diffuse in opposite directions, therefore if there is an equal number of

them, the voltage drop equates to zero. It is worth noting that while a very thorough study was done to document the energy levels of PbS films with various ligand treatments (two overlap with this study) via UPS and absorption spectroscopy,(*98*) all of the films appeared n-type (Fermi level above mid-gap), which is contradictory to previous reports that most ligand treatments, with the exception of TBAI,(*111*) behave p-type.(*19*, *31*, *41*, *112*) This discrepancy could be due to the different measurement techniques (UPS vs. CV and T-dependent Seebeck). We believe that our data offers the advantage of being purely electronic in nature and within conditions of a working device for which one would want to integrate these materials. SCN also appears particularly highly p-doped. Previous reports from FETs have shown SCN treatment to result in degenerately p-type to ambipolar to n-type channel behavior as the work-function of the metal electrode is selected to be closer to vacuum.(*19*, *112*) The sign of Hall measurements for SCN is positive (see Section 4). Susceptibility of SCN to oxygen exposure, even within and N_2 glovebox, could play a role for this apparent degenerate behavior, though care was taken to replicate the same conditions (time between preparation and measurement) as the FET measurements. It should also be noted that film and operating conditions significantly differ for FET versus Seebeck measurements. The FET measurements are on a very thin film (20 – 40 nm), whereas the Seebeck (and Hall measurements) are on thicker films (200 – 500 nm). Furthermore, Seebeck measurements are not gated or affected by the choice of metal contact. Despite prolonged exposure (> 24 hrs) to $PbCl_2$ at elevated temperature (85°C), we were never able to actually observe a negative Seebeck

coefficient indicative of n-type behavior. However, increased $PbCl_2$ exposure clearly not only tunes the Fermi level within the bandgap, but also has a slight effect on the position of the conduction band relative to vacuum. This was also seen in the UPS study and is attributed to a change in the NC surface dipole, which affects the electron binding energy therefore shifting the band edge relative to vacuum.(*98*) These results clearly demonstrate why creating a grated QD solar cell by stacking films treated by a more highly p-doping ligand (i.e. EDT or MPA)(*28, 80, 81, 99*) with a more "intrinsic" ligand such as TBAI is beneficial and how $PbCl_2$ may provide a more stable, tunable alternative to TBAI.

In conclusion, we show within this study that the temperature dependent Seebeck measurement is a useful tool in quantifying how the position of the Fermi level relative to the electronic transport level changes with different surface chemistry treatments using an electronic method. When coupled with an electronic CV measurement and absorption spectroscopy, an energy level diagram can be compiled from which one can then specifically engineer device junctions based on the material's work function. Furthermore, we show that by using a Na_2S surface treatment followed by controlled exposure to $PbCl_2$ one can, not just qualitatively, but quantitatively, tune the PbSe film from almost degenerate p-type to close to instrinsic. We believe that this method will be useful in investigating the doping effects of any new ligand treatments that may arise in following years.

3.4 Experimental Details Specific to Work Presented in Chapter 3

3.4.1 PbSe NC Synthesis

6 nm PbSe NCs with a first optical absorption peak at 1728 nm (0.72 eV) were synthesized following the procedure described in Section 1.3.2 except at a scale of 1.78 g PbO, 40 mL ODE, 6 mL OA, an injection of 16 mL of TOP-Se + 138 uL of DPP at 150°C, and a reaction time of 10 min before allowing the solution to naturally cool after removing the heating mantle.

3.4.2 Film Deposition and Ligand Exchange

Coverglass slides (Gold Seal No. 2, 22x22 mm) were pretreated by first sonicating in a DI water/detergent solution for 20 min, followed by sonication in a 1:1:1 mixture of DI water:acetone:ethanol solution, treatment under UV-ozone with pure O_2 for 30 min, then finally submerged in a 1 vol% mixture of MPTS in anhydrous toluene for ~12 hours. Substrates were then rinsed with toluene and sonicated in ethanol for 5 min. The coverglass was fixed to a ~1x1 inch piece of glass with a gel-pack square and mounted on the spin coater. The ligand solutions were prepared as: 27 mM (10.1 mg/mL) TBAI in methanol, 130 mM (10 mg/mL) SCN in ACN, 1 mM Na_2S in methanol, 50 mM $PbCl_2$ in ethylene glycol. 2 drops of the nanocrystal solution (~35 mg/mL in 5:1 octane:hexane) were dispensed on the surface and immediately spun at a rate of 800-1500 rpm until the film dried. 6 drops (~300 uL) of the ligand exchange solution were dispensed onto the film surface, enough to completely cover, and allowed to sit for 30 sec. The solution was then spun off until dry, then rinsed with ~6 drops of pure solvent (same as the dispersive

solvent). The subsequent treatments with $PbCl_2$ after Na_2S treatments were as follows: the substrate was covered with the solution, then allowed to sit for the specified time (3, 15, or 30 min) then rinsed first with ethylene glycol, then twice with acetone. This was repeated to produce a film of 8 layers. For the 24 hour $PbCl_2$ treatment, the film was first built up to the 8 layers with 15 min $PbCl_2$ treatment after each layer, then the film was immersed in the $PbCl_2$ solution for 24 hours at 85°C on a hotplate.

3.4.3 Seebeck Measurements

Seebeck measurements were taken with an MMR system Seebeck stage using the SB-100 and K-20 controllers. The films were carefully scored with a diamond scribe then cleaved into a section about 2.5 x 5 mm. The film was them mounted onto the Seebeck stage with silver paint (Leitsilber 200) opposite the reference wire (constantan), also mounted with silver paint. A picture of the sample stage is shown in **Figure 3.9**.

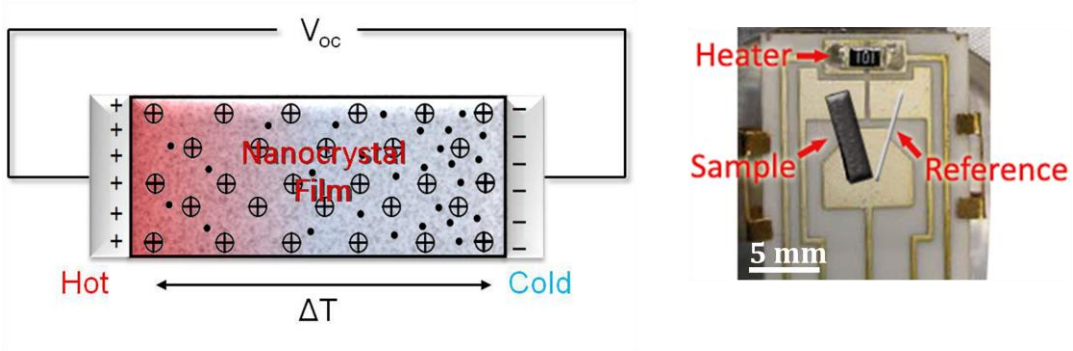

Figure 3.9: *Schematic of the Seebeck effect (left) and a picture of the Seebeck heating sample stage (right).*

3.4.4 Cyclic Voltammetry

CV measurements were performed using an electrochemistry workstation (Epsilon, C-3 cell stand). The setup is a three-electrode system system operated in an organic electrolyte of 10 mM of tetrabutyl ammonium hexafluorophosphate (TBAHP) in acetonitrile. NC films are deposited on Pd-coated Si substrates (working electrode). The reference electrode is $Ag/AgNO_3$ (10 mM, non-aqueous electrolyte). A Pt wire is used as the auxiliary electrode. All potentials are calibrated in reference to the ferrocene/ferrocenium redox couple measured in the same system. All steps are carried out in a N_2 filled glovebox.

4 APPLYING AC HALL AND SEEBECK MEASUREMENTS TO PROBE THE ELECTRONIC PROPERTIES OF LEAD SELENIDE NANOCRYSTAL FILMS

Traditionally, Hall effect measurements, coupled with resistivity measurements, are used to determine fundamental electronic properties of materials, such as carrier type, carrier concentration, and mobility. This is because the Hall effect measurement probes free (non-trapped) carriers.(*113*) However, electronic carrier mobilities in nanocrystal thin films are typically orders of magnitude lower than their traditional bulk counterparts.(*40*, *114*) The DC Hall measurement, that is, with a DC magnetic field, has practical limitations when it comes to measuring low mobility (≤1 $cm^2/V{\cdot}s$), high resistivity films where the resulting hall voltage is weak. Yet NC materials in this mobility range (10^{-4}-1 $cm^2/V{\cdot}s$) produce some of the most efficient NC solar cells and are therefore of interest to characterize.(*19*, *24*, *32*) We explore the AC magnetic-field Hall measurement as a technique by which to probe the electronic properties of NC materials in this regime from which we determine the mobility, Hall sign, and estimate the carrier density. It is important to note that in materials where transport is dominated by hopping or other heat activated transport mechanisms, such as in the case with amorphous semiconductors and many nanocrystal systems, an accepted model for describing the physics behind the Hall effect has not been well established.(*115*, *116*) One may also observe the Hall "sign anomaly,"(*117–119*) where the Hall coefficient shows the opposite

sign to the majority carrier. Therefore, we also couple the Hall measurements with Seebeck measurements to remove this ambiguity.

The most frequently exploited method to measure transport properties of NC films has been to extract them from FET devices.(*120–122*) This technique is useful when applied to semiconductor materials which can be gated. The mobility can be calculated for both electrons and holes in films that exhibit ambipolar FET behavior. However, FET measurements are not suited for highly degenerate materials which show poor gating,(*19*, *41*) or materials which exhibit large hysteresis.(*123*) Furthermore, in FET operation, both the gate bias, which shifts the Fermi level, and choice of metal contact can promote charge injection, affecting carrier density.(*100*) Additionally, transport within an FET device occurs in a very thin channel layer where traps at the nanocrystal/dielectric interface can significantly affect carrier lifetime,(*124*, *125*) and mobility.(*116*) THz(*126*, *127*) and microwave conductivity(*76*, *91*) measurements have also been applied to determine the mobility and lifetime of carriers in NC films. While these techniques have the advantage of being contactless, they produce an average of the transport properties from both the electrons and holes and are very local in nature. The Hall effect measurement can be used as a complimentary method to those referenced above in determining transport properties of films, particularly for materials unsuited for FET measurements and where macroscopic properties are relevant on the device scale. It is the traditional method of choice for determining transport properties for applications

such as photovoltaics, thermoelectric devices, and LEDs, where there is no operational bias to promote charge injection.

Within this study, we use the AC magnetic-field Hall measurement to extract electronic properties of the carriers in nanocrystal thin films and couple these with Seebeck measurements to confirm the carrier type. We investigate a library of different ligand chemistries including those commonly used for nanocrystal thin film solar cells, such as 1,3-benzenedithiol (BDT),(*25*, *128*) ethanedithiol (EDT),(*35*, *129–131*) and tetrabutyl-ammonium iodide (TBAI).(*32*, *111*) Additionally, we measure films treated with ammonium thiocyanate (SCN),(*52*, *132*, *133*) sodium sulfide (Na_2S),(*20*, *41*, *124*, *134*) and sodium sulfide (Na_2Se)(*41*) previously used for higher mobility nanocrystal FET devices. We also investigate $ZnCl_2$ as new metal halide ligand treatment.

There are two different types of Hall measurements that are characterized as "AC Hall." The applied excitation current can be an AC signal, while the magnetic field remains static, resulting in an oscillating Hall voltage.(*115*) On the other hand, the excitation current can remain DC while an oscillating magnetic field is applied, also resulting in an oscillating Hall voltage. We apply the latter technique, which has advantages over the former because it decouples the true Hall voltage from the misalignment voltage, which becomes significant for low mobility, high resistivity films. This allows us to apply small excitation currents (down to nA) to minimize resistive heating and for an equilibrium to stabilize. We can then measure small hall voltages down to μV.

4.1 The Hall Effect in Low Mobility Materials

As previously mentioned, the Hall effect has been the historical method in determining the carrier type (holes or electrons), mobility (μ), and carrier concentration (η) of electronic materials. The principle behind the Hall measurement is to measure the current deflection within the film when a magnetic field is applied in the normal direction. If we have the Van der Pauw setup illustrated in **Figure 4.1**, an electric field (E_x) is applied across the diagonal between electrodes 2 and 4 to create a steady state current (I_x). A magnetic field (B) is applied normal to the film. This magnetic field induces the Hall electric field (E_y) which deflects carriers in the y-direction.

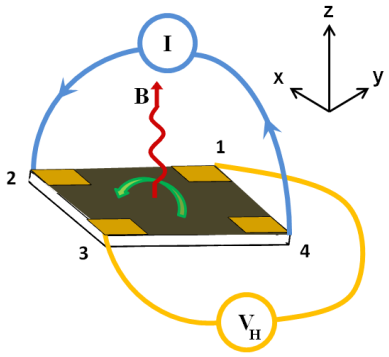

Figure 4.1: *A schematic of the Hall measurement using the Van der Pauw setup.*

The Hall coefficient (R_H) is defined using these set of measurable parameters:

Equation 4

$$R_H \equiv \frac{E_y}{I_x B} = \frac{V_H d}{I_x B}$$

Where V_H is the Hall voltage and d is the sample thickness. The transverse carrier velocity of the deflected carriers is defined as $v_\perp \equiv \mu_H v B$. Thus we have a definition of

the Hall mobility, which essentially describes the fraction of carriers that are influenced by the presence of the magnetic field. The degree of deflection felt by the carriers is defined as the Hall angle:

Equation 5

$$\theta_H \equiv \frac{v_\perp}{v} = \frac{\mu_H v B}{v} = \mu_H B$$

However, there is no net current flow across the y-direction. Instead, a space charge develops, which is the measured Hall voltage (V_H). For the net current to equal zero, the deflection of carriers by the magnetic field must be balanced in the y-direction and therefore:

Equation 6

$$\frac{E_y}{I_x/\sigma} = -\mu_H B$$

Where σ is electrical conductivity defined as

Equation 7

$$\sigma = \eta q \mu_\sigma$$

with η as the carrier density and μ_σ the "conductivity" mobility (also sometimes referred to as the "drift" mobility). If we insert the definition of the Hall coefficient into Equation 6, the definition of the Hall mobility simply becomes:(*135*, *136*)

Equation 8

$$\mu_H = -\sigma R_H$$

Therefore, we can calculate the Hall mobility by coupling Hall and conductivity measurements. If we substitute the definition of electrical conductivity into Equation 8, we receive a familiar form of the Hall coefficient:

Equation 9

$$R_H = -\frac{\mu_H}{\eta q \mu_\sigma}$$

Equation 10

$$r_H = \frac{\mu_H}{\mu_\sigma} \therefore R_H = -\frac{r_H}{\eta q}$$

r_H is commonly referred to as the Hall factor and is the ratio of the Hall and conductivity mobilities, which is generally taken to be unity, but can vary between 0.5-1.5 depending on the scattering mechanism.(*137*) This is discussed in more detail below.

Where a divergence arises between interpreting Hall measurements for classic materials with high mobility, delocalized carriers and low mobility materials with thermally activated transport (such as amorphous semiconductors) is in the determination of carrier type and density, as well as the lack of a universal model describing the physical mechanism of how the Hall effect is generated. The classic model used to determine the carrier type and density assumes an ordered, periodic crystal structure represented by Bloch functions from which one can generate energy bands and apply the effective mass approximation for free carriers. In these systems, the Hall and conductivity mobilities are usually very similar values, therefore $r_H \approx 1$ and the carrier concentration can easily be calculated from Equation 9. Dopant atoms act as electron donors or

acceptors and, importantly, as scattering sites for transport because they disrupt the continuity of energy levels within the otherwise regular crystal lattice (i.e. $\mu \propto 1/\eta$).

However, the models for interpreting the underlying physics of the Hall effect in systems with a large degree of disorder are diverse (after all, there are *many* ways in which a system can be disordered) and less understood.(*138*) There is a lot of research between the mid-60's and 70's studying the Hall effect in disordered materials such as amorphous silicon (a-Si),(*139*) amorphous chalcogenides,(*119*) and transition metal oxides.(*138*) A few of the theories include: the Mott-Cohen-Fritzsche-Ovshinsky model,(*119*, *140*, *141*) where carrier transport in disordered systems is viewed as taking place via two parallel paths: one that is high mobility through extended states, and the other through hopping between localized states where transport is phonon assisted. The dominance of the low mobility transport mechanism is explained by a high density of localized states within the hopping transport regime as compared to the higher energy (i.e. higher activation energy) extended states. Another is the Random Phase Model (RPM),(*138*, *142*) where transport is believed to take place in extended states with the mean free path is larger than atomic spacing, but too short for the Bloch theorem to apply (i.e. phase coherence is lost from atom to atom).

Most of the models that diverge from the classic, delocalized carrier picture can be placed into two categories: 1) materials with transport in continuous "band" states, but where the bandwidth is narrow ($< kT$) or, 2) materials where carriers are largely localized and therefore transport occurs via a thermally activated (phonon assisted) hopping

mechanism. The second scenario has generally been deemed appropriate in describing temperature dependent conductivity studies of NC solids where conduction is clearly thermally activated.(*135*)

One of the key aspects to comprehend about systems with thermally activated transport is that μ_σ and μ_H are generally *not* equivalent. This is because the mechanism by which carrier transport is affected by a magnetic field versus an electric field is fundamentally different in localized systems. Instead of behaving as a free carrier, a thermally activated carrier can be modeled as a small polaron, meaning the charge carrier is highly localized and is strongly coupled to atomic displacements.(*135*, *136*) In polaron hopping transport, heat manifest as lattice vibrations (phonons) creates a constant fluctuation of the site energy distributions. When a configuration arises where the energy difference between the currently occupied site and a nearby site coincide, the carrier has the opportunity to "hop" to that site. An illustration of this process is shown in **Figure 4.2** where the carrier is at an initial site (a), then shared between the initial and final sites (b) before re-equilibrating at the final site (c).(*136*)

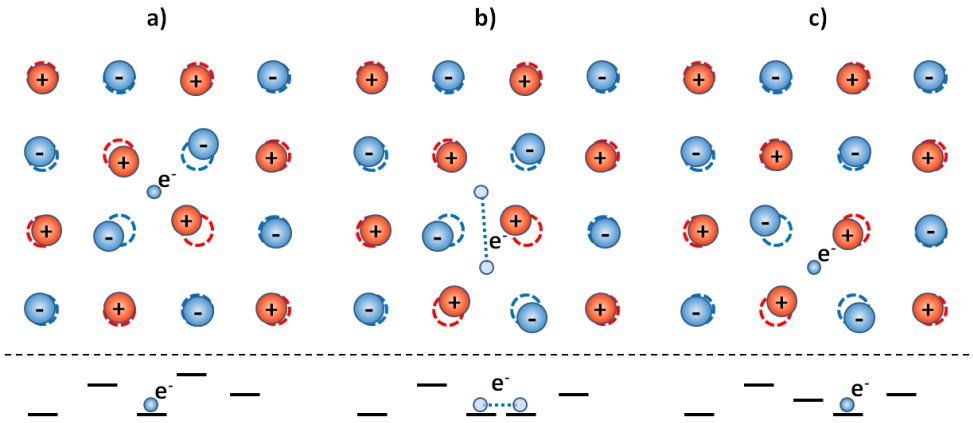

Figure 4.2*: *Schematic representation of the "hop" of a carrier from one localized site to another.

It may appear that this transport mechanism excludes the possibility of any influence on the carrier's direction from a magnetic field. However, higher order processes (ones that involve 3 or more sites) are certainly subject to a magnetic field and that effect isn't necessarily small. In fact, in systems dominated by hopping conduction, it is common for $\mu_H > \mu_\sigma$.(*135*, *136*) **Figure 4.3** shows how within a 3 site model (for both a triangular and square lattice), a carrier can take two distinguishable paths, which could be influenced by the Hall field.

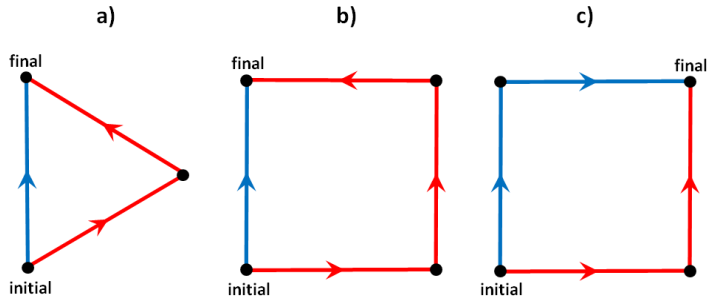

Figure 4.3: *Different hopping conduction paths between initial and final sites in a triangular and square lattice. The scenarios in a) and b) show distinguishable, asymmetric paths, whereas c) show two equivalent paths.*

Another way to look at the manifestation of the Hall effect in the hopping regime is the direct influence of the magnetic field on the polarons themselves, which, as a type of bound dipole, will adjust to the field, possibly resulting in a lower energy path that would not have existed otherwise. In other words, in the classic model with extended states, the carrier feels a "continuous" effect of the magnetic field; where as in a hopping system, the carrier "samples" the magnetic field in between quantum transitions. In order to see the net effects in the hopping system, the carrier has to have at least two available paths by which to hop (3-site model), so that the effects of the magnetic field can be distinguished.(*138*)

4.2 Observed Phenomenon Unique to Hopping Transport

Because of the fundamental difference in the mechanism of transport between extended state and thermally activated materials, there are, not surprisingly, divergences from the familiar classical behavior. For one, increasing the carrier density actually increases carrier mobility rather than suppressing it. A larger number of polarons diminishes self-trapping because they compete to displace the same atoms (i.e. large η destabilizes self-trapping).(*135*) Or, from another point of view, creates more sites of comparable energy to hop to. Furthermore, as already mentioned, the rate of transport scales proportional to temperature. This is because in the case of small polarons (carriers

localized and strongly coupled to atomic displacements), atomic motion/vibrations *facilitate* carrier transport by providing the energy needed to hop. Whereas for delocalized carriers, atomic vibrations *inhibit* carrier transport due to increased scattering of the free carrier. The Hall effect occurs when atomic vibrations cause an intermediate site to coincide with the energies of the initial and final sites.

Another interesting possible consequence of thermally activated transport is the "Hall sign anomaly." That is, the Hall coefficient sometimes expresses a different sign than that of the majority carrier, in disagreement with the sign of its Seebeck coefficient. An early example is chalcogenide glasses, which independent of the dopant, always exhibit a negative Hall coefficient.(*119*) This lead to theory suggesting that in a hopping model, the Hall coefficient would always be negative, until a "double sign anomaly" was observed in amorphous silicon, where phosphorous-doped "n-type" amorphous silicon (a-Si:P) showed a positive Hall coefficient and boron-doped "p-type" amorphous silicon (a-Si:B) showed a negative Hall sign.(*143*) Details of the derivation as to how this phenomenon can be explained are published elsewhere.(*144*) In summary, the sign of R_H depends on the sign of the product of the intersite transfer integral (J) around a closed loop of the available hop sites. The result is that if the number of sites is odd (i.e. 3-site), the Hall coefficient can be opposite that of the majority carrier (the Hall sign anomaly), but if the number of sites is even (i.e. 4-site), the sign of Hall coefficient is normal.(*136*, *138*, *144*)

For those attempted, calculations suggest that the Hall mobility should have a lower activation energy than conductivity mobility for polaron transport: $\epsilon_{AHall} < \epsilon_{A\sigma}$.(*138*, *144*, *145*). Generally speaking:

Equation 11

$$\mu_H \propto exp\left[\frac{-(\varepsilon_3 - \varepsilon_2)}{k_B T}\right]$$

Where ε_2 and ε_3 are the energies associated with two versus three sites of coinciding potentials.

For the specific case of a adiabatic hopping in a triangular lattice:

Equation 12

$$\mu_H = CF(T)exp\left[-\frac{\epsilon_2/3 - J}{kT}\right]$$

$$\mu_\sigma = 3CF(T)exp\left[-\frac{\epsilon_2 - J}{kT}\right]$$

Where *F(T)* is a dimensionless function of temperature. Taking the ratio of μ_H and μ_σ, we can get the Hall factor r_H and insert it into the equation for the Hall coefficient:

Equation 13

$$R_H = -\frac{1}{\eta q}\left[\frac{\mu_H}{\mu_\sigma}\right] = -\frac{1}{\eta q}\left[\left(\frac{F(T)}{3}\right)exp\left(\frac{2\epsilon_2}{3kT}\right)\right]$$

The plots of μ_σ and μ_H versus reciprocal temperature calculated from the above equations are shown in **Figure 4.4**,(*136*, *145*) where *J* is the transfer integral. The curves (a, b, c) represent decreasing ratios of the conductivity mobility thermal activation energy ($\epsilon_{A\sigma}$) over the transfer interal ($\epsilon_{A\sigma}/J$).

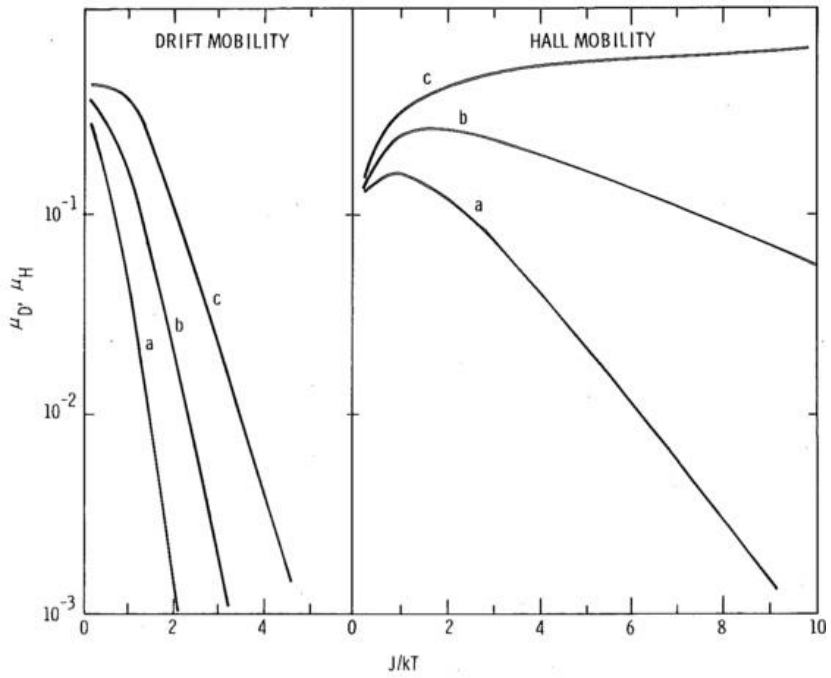

Figure 4.4: *Dependence of Hall and conductivity mobilities on inverse temperature.*(*136*)

4.3 Limitations of the DC Hall Measurement

In a traditional DC Hall measurement, an excitation current is applied across one diagonal of the film while a static magnetic field is applied normal to the film. The Hall voltage can then be measured as shown in **Figure 4.1**. Practically, though, the actual measured voltage (V_m) includes several erroneous voltages that must be cancelled out in order to obtain the true Hall voltage (Equation 14, Equation 15). These include the thermoelectric voltage (V_{TE}) and the misalignment voltage (V_O).

Equation 14

$$V_m = V_H + V_O + V_{TE}$$

Equation 15

$$V_O = \alpha \frac{\rho}{d} I$$

The thermoelectric voltage results from the thermocouple junction formed between two different materials, the nanocrystal thin film and the metal contact, and is independent of current. The misalignment voltage is dependent on resistivity (ρ), current, and a factor, α, that is related to the sample geometry. The factor α converts resistivity to resistance and has a value typically somewhere between 0 and 1.(*146*) The more symmetric the sample and the smaller the ratio of the contact size to sample length, the closer α is to zero. In a typical DC measurement, current reversal is used to eliminate the thermoelectric voltage and field reversal eliminates the misalignment voltage. However, in the case of low mobility, high resistivity materials where the induced Hall voltage is very small, the misalignment term can overwhelm the Hall signal to the point where field reversal is insufficient to cancel out its contribution. If we rewrite the Hall voltage in terms of mobility and resistivity, the measured voltage can be expressed as:

Equation 16

$$V_m = \frac{\rho I}{d}(\mu B + \alpha) + V_{TE}$$

Ideally, $\alpha/\mu B < 1$ so that the offset voltage is small relative to the Hall voltage. With mobility values in the 0.01 – 0.1 $cm^2/V{\cdot}s$ range, and a 1 T magnetic field, the misalignment voltage can easily be two to three orders of magnitude larger than the Hall voltage (see **Table 3** to see how α scales with geometry).(*146*) The resulting large offset voltage makes a Hall measurement difficult in practice through field and current reversal

alone. Attempted measurements frequently result in extracted Hall voltages that flip sign from one measurement to the next.(*146*)

4.4 Advantages of the AC Hall Method

Using an AC magnetic field paired with a lock-in amplifier, one can decouple the Hall voltage from the misalignment and thermoelectric voltages. Because both are independent of the magnetic field, they remain DC voltages while the Hall voltage is now alternating. Lock-in amplification allows the Hall voltage to be extracted exclusively. A diagram of the setup used for the measurement is shown in **Figure 4.5**.

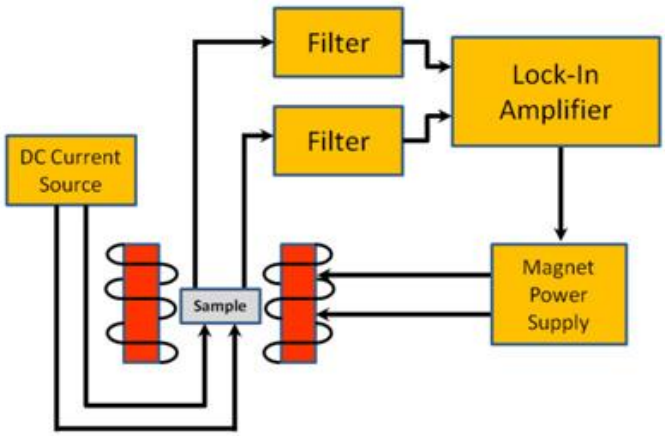

Figure 4.5: *Diagram of the AC Hall measurement setup.*

The measured voltage now becomes:

Equation 17

$$V_m = V_H + V_I + V_O + V_{TE}$$

Equation 18

$$V_m = \frac{R_H I}{d} B\cos(\omega t) - B\sin(\omega t) + \alpha \frac{\rho}{d} I + V_{TE}$$

An additional term, V_I, which is 90° out of phase with the Hall signal arises due to inductance of the sample and wiring. If there is no phase error in the system, the lock-in can distinguish the Hall signal from the inductance voltage comparing its x and y channels. This ideal case is not usually the reality and results in voltages shown in Equation 19a,b.

Equation 19

$$V_x = \frac{R_H I}{d} B_{RMS} cos(\varphi) + \beta\omega B_{RMS} sin(\varphi) \qquad \text{(a)}$$

$$V_y = \frac{R_H I}{d} B_{RMS} sin(\varphi) - \beta\omega B_{RMS} cos(\varphi) \qquad \text{(b)}$$

φ is defined as the phase error, B_{RMS} is the root mean square of the magnetic field. But because the induced voltage (second term in 9a,b) is independent of current, it can be eliminated using current reversal. Resistivity is calculated using the van der Pauw method with a square geometry as described in Section 4.8.

4.5 Structural and Optical Characterization

In order to correlate the electronic properties of the ligand treatments with the materials' structural and optical properties, we characterize the films using fourier transform infrared (FTIR) and UV-Vis spectroscopy, small angle x-ray scattering (SAXS) and wide angle x-ray scattering (WAXS), and transmission electron microscopy (TEM). We prepared films of 6.5 +/- 0.2 nm PbSe nanocrystals using either SCN, Na_2S, Na_2Se, TBAI, EDT, BDT, or $ZnCl_2$ as the displacing ligand. The films are prepared using a layer by layer approach *via* spin-coating. The PbSe nanocrystals are spin-coated from a

5:1 octane:hexane solution at a concentration of ~35 mg/mL onto a treated glass substrate. Details of the spin-coating process and individual ligand treatments are outlined in the Section 4.8. FTIR spectra demonstrate substantial (>90%) removal of the native oleic acid after ligand exchange (**Figure 4.6a**). UV-Vis show as deposited, nanocrystal films with native ligands have a first excitation peak at 1702 nm (0.729 eV) **Figure 4.6b**.

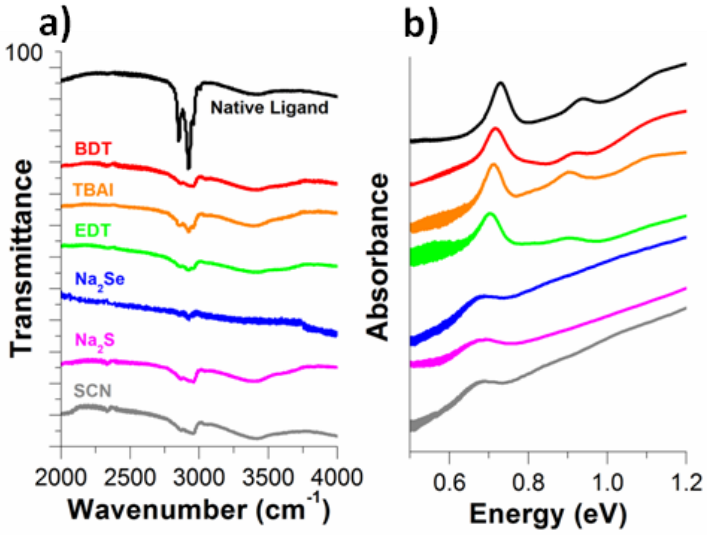

Figure 4.6: *Optical characterization of the films as a) FTIR showing ligand removal, stacked for clarity: native ligand (black), BDT (red), TBAI (orange), EDT (green), Na_2Se (blue), Na_2S (pink), SCN (grey) and b) absorption spectra, normalized and stacked for clarity (same color scheme).*

Ligand exchange results in a red shift and broadening of the peak. For BDT, TBAI, EDT, Na_2S, and SCN exchanged films, there is a red shift of 13, 17, 28, 35, 39, and 40 meV, respectively. These changes in the optical spectra have been attributed to a decrease in

nanocrystal spacing, increase of electronic coupling, and/or an increase in trap states.(*18*, *41*, *147*, *148*) SAXS data (left side of **Figure 4.7**) shows a shift of the first peak to a higher angle for the ligand-exchanged samples compared to the native ligand, indicating a decrease in the average inter-particle spacing, consistent with the optical data. The ringing pattern in the SAXS data also becomes less defined, particularly for Na_2Se, Na_2S, and SCN treated films, which suggests possible "necking" or loss of the uniform, discreet crystal size of the individual NCs.(*20*)

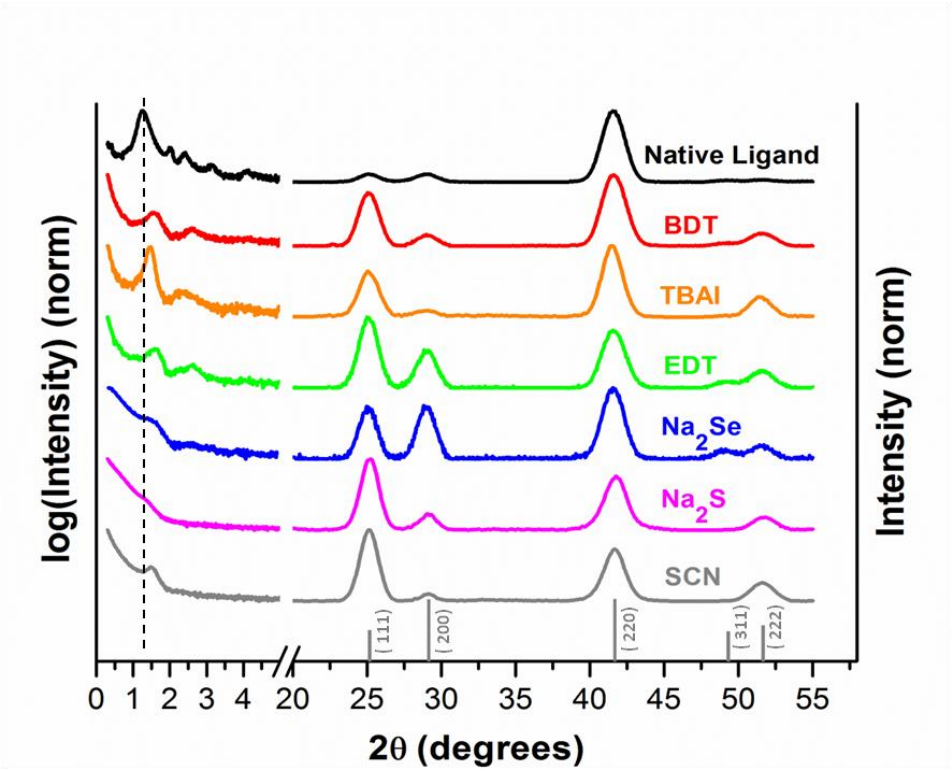

Figure 4.7: *SAXS and WAXS data taken for spin-coated films: native ligand (black), BDT (red), TBAI (orange), EDT (green), Na_2Se (blue), Na_2S (pink), SCN (grey). Grey lines are reference for rock salt galena PbSe.*(*149*) *Curves are normalized and stacked for clarity.*

WAXS measurements are also shown on the right side of **Figure 4.7**. Analysis of the FWHM of the (220) peaks show < 3% peak sharpening, suggesting little grain growth in this direction. However, the (111) peak shows two interesting features: 1) There is an increase in peak intensity relative to the native ligand film and database PbSe spectra, 2) for the Na_2S and SCN films, there is a notable sharpening of the peak, by 8% and 9%, respectively. This suggests that there is preferred orientation of all ligand exchanged NCs on the substrate as well as some degree of particle "necking" in the (111) direction for the Na_2S and SCN treatments. TEM images of the spin-coated films show a decrease in NC spacing upon ligand exchange along with varying degrees of structural order (**Figure 4.8**). Depending on the ligand treatment, the TEM images show some oriented attachment and/or fusing of NC facets. This is particularly pronounced for SCN, Na_2S, and Na_2Se which also show the most significant peak broadening in the absorption spectra and the most evidence for necking in SAXS and WAXS, though all films show a notable degree of order preservation. This oriented attachment (see **Figure 4.14**), has been demonstrated before in PbSe nanocrystal films after assembly on a liquid interface,(*150*) ligand displacement,(*34*) and several solid state ligand exchange treatments.(*41*, *151*) It is therefore apparent that the peak broadening and red shift in the absorption spectra cannot be soley contributed to either surface chalcogenide enrichment(*41*) or the "quantum coupling" effect, but could also partially be a result of a reduction of quantum confinement due to the onset of particle facet fusion.

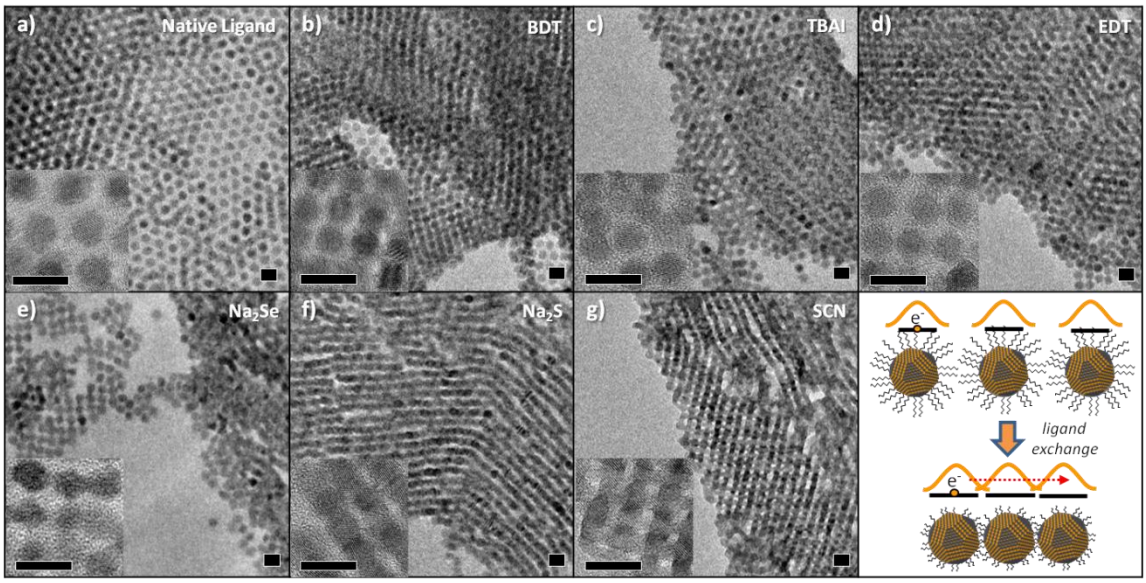

Figure 4.8: *TEM images of spin-coated films with higher resolution insets showing the degree of nanocrystal fusion: a) native ligand, b) BDT, c) TBAI, d) EDT, e) Na_2Se, f) Na_2S, and g) SCN. All scale bars are 10 nm.*

4.6 Applying the AC Hall Method

For AC Hall measurements, nanocrystal films with four top contact electrodes are prepared in the van der Pauw geometry (see Section 4.8 for details). All of the film preparation is done air-free within a nitrogen filled glovebox. AC Hall measurements are taken using a Lakeshore 8404 AC/DC Hall Effect Measurement System at a field of 1.25 T and frequency of 100 mHz. Before the actual AC Hall measurements are made, each sample was first confirmed to exhibit ohmic behavior (see example **Figure 4.12**). It is important to select the appropriate excitation current to be applied across the film. A higher current results in a larger Hall voltage, as evident from Equation 8. However, if the current is too high, it can cause Joule heating of the sample, creating thermal

fluctuations resulting in an unstable AC voltage. These fluctuations make it practically impossible to make an accurate measurement. Furthermore, lead chalcogenide NCs are known to undergo morphological changes at relatively low temperatures(*51*) or high DC electric fields,(*152*) and it is possible that local heating could become significant if too high of a current is applied in highly resistive films. Therefore, there is a balance in choosing the appropriate excitation current between maximizing signal, collection time and minimizing resistive heating. The magnitude of the excitation current was chosen to always result in a voltage less than 1 V, determined during the measurements to confirm ohmic behavior. These conditions were generally found to result in a stable Hall voltage. In **Figure 4.9** we compare examples of the Hall voltages for (a) an excitation current that is too high and results in transient dynamics when current is first applied in contrast to (b) an excitation current yielding a stable Hall signal after initial hysteresis.

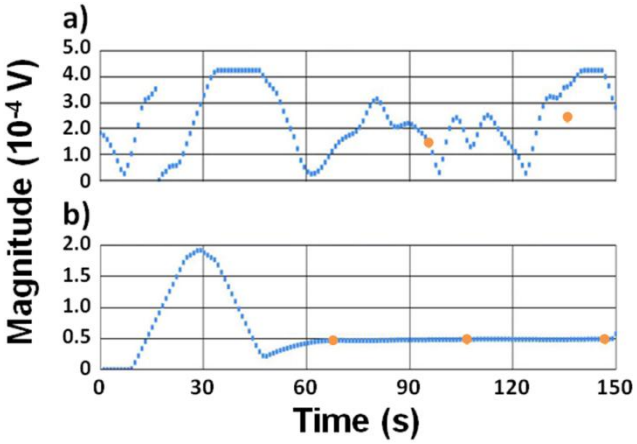

Figure 4.9: *Measured AC voltage with (a) too high excitation an current and (b) an appropriate excitation current.*

For each sample, the measured voltage was first checked to settle at the chosen excitation current before the actual measurement was conducted. The voltage is then sampled at specified intervals after the current is first applied and averaged. The higher the resistivity of the films, the longer the chosen settling time.

4.7 AC Hall Measurement Results

The resistivity, mobility, and estimated carrier concentration of the films from the van der Pauw resistivity and AC Hall measurements are displayed in **Figure 4.10**. The values calculated for the mobilities are summarized in **Table 2**. All films, except for $ZnCl_2$ treated, exhibited a positive Hall voltage, indicating holes are the majority carrier. Mobility values reported in the literature vary widely depending on the nanocrystal size,(*40*, *153*) ligand concentration used during exchange,(*154*) the method used to calculate mobility, and the device structure, such as the choice of gate dielectric in FETs,(*155*) therefore making it difficult to quantitatively compare. However, we've attempted to summarize mobility values previously published when they existed and included them in **Table 2** below our own results. The red bars in **Figure 4.10c** for the carrier density indicate a Hall factor (r_H) of up to 1.5.

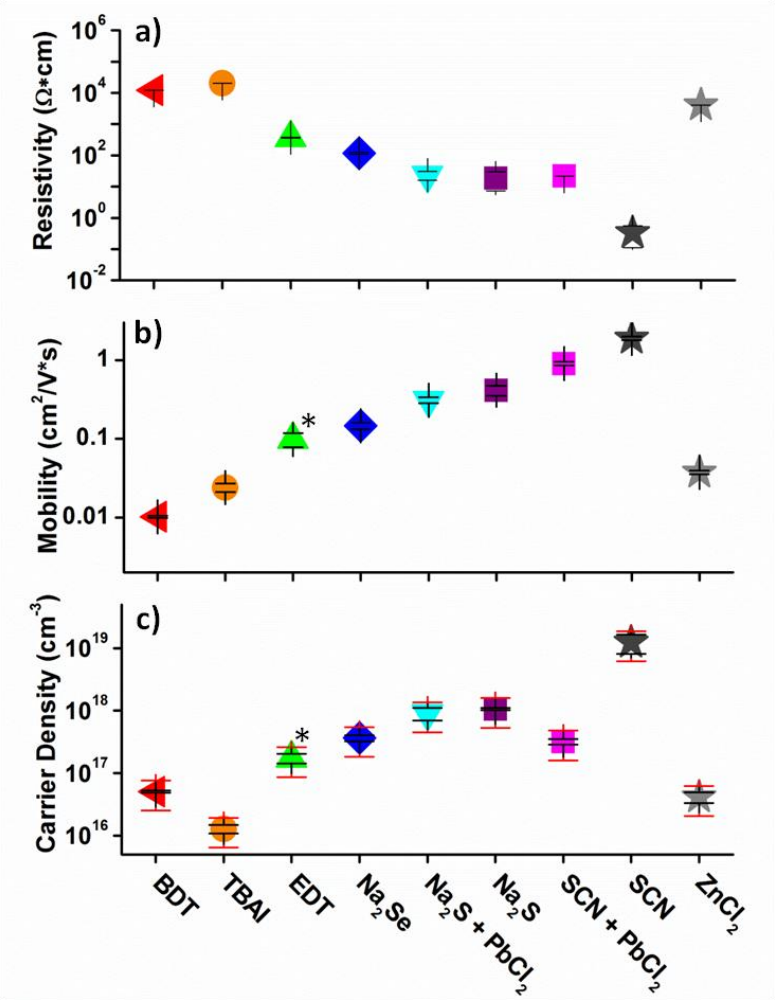

Figure 4.10: *Results from van der Pauw and AC Hall Measurements: a) resistivity, b) mobility, and c) estimated carrier density. The asterisk indicates that the Hall sign was negative.*

The only case in which unannealed PbSe nanocrystal films were measured air free using the Hall effect (DC) was where we previously reported a mobility for SCN exchanged films of 0.28 $cm^2/V{\cdot}s$.(*19*) Another report measured acetonitrile (4.1 $cm^2/V{\cdot}s$),

N,N-dimethylformamide (2.6 $cm^2/V{\cdot}s$), and hexamethylphosphoramide (2.5 $cm^2/V{\cdot}s$) treated PbSe films, which were measured in air.(*156*)

Ligand	**SCN**	**SCN + $PbCl_2$**	**Na_2S**	**Na_2S + $PbCl_2$**	**Na_2Se**	**EDT**	**$ZnCl_2$**	**TBAI**	**BDT**
μ_H	1.9 +/– 0.1	0.90 +/– 0.05	0.41 +/– 0.06	0.31 +/– 0.02	0.15 +/– 0.01	0.10 +/– 0.02	0.037 +/– 0.002	0.024 +/– 0.003	0.010 +/– 0.003
Hall Sign	+	+	+	+	+	+	-	+	+
Seebeck Sign	+	+	+	+	+	+	+	+	N/A
$\mu_{FET(h)}$	0.01-0.04 (*157*)		0.005 – 0.08 (*41*)		0.0075 (*41*)	0.001 – 0.008 (*112*)		0.0031 (*112*)	10^{-4} – 10^{-5} (*112*)
$\mu_{FET(e)}$	0.02 (*19*)	4(*112*)		1.8 (*41*)		0.001 – 0.008 (*112*)		0.08 – 0.5 (*112*)	10^{-4} – 10^{-5} (*112*)
TRMC					2.57 +/– 0.23 (*91*)	0.27 (*158*)			
THz	31(*127*)		25(*127*)			5.8 (*127*)		4.2 (*127*)	
CELIV									$2.4x10^{-3}$ (*36*)

Table 2: *Hall mobilities ($cm^2/V{\cdot}s$) calculated for this study along with mobility values sourced from other publications.*

Previous reports for TBAI treatment of lead chalcogenide NCs have demonstrated n-type,(*111*, *112*) p-type,(*52*) and ambipolar(*154*) FET behavior. These differences could be attributed to pre-halide treatments typically used by the Sargent group,(*52*) and choice of top contact for the FET device, which can affect selectivity of the carrier injected into the channel due to difference in work function.(*112*, *159*) Further discrepancies between FET and the Hall carrier types could be explained by geometry (~ 20 nm thick) and

operation (gated transport) of an FET, particularly if the material has a high density of low mobility holes and a low density of high mobility electrons. Additionally, the FET curves reported for Na_2S and Na_2Se show very poor gating associated with high carrier density therefore resulting in artificially low mobility from the FET calculations.(*41*) On the other end, films with longer ligands such as EDT or BDT tend to have very large hysteresis, also calling into question the accuracy of the FET measurement in determining mobility.(*35*, *100*) To eliminate the ambiguity of the carrier type, we conducted Seebeck measurements, which is the method generally accepted to reflect the true majority carrier.(*141*) All of the films had positive Seebeck coefficients, indicating holes as the majority carrier, with values ranging from 669 μV/K for SCN to 891 μV/K for TBAI. BDT was too resistive for the measurement system.

The trends we see in the Hall mobility when comparing the various ligands generally reflect those in literature, with BDT having very low mobilities and SCN some of the highest, relatively speaking. The trends are also what one would expect based on the decrease of inter-particle spacing shown in the SAXS data. The fact that Na_2S and SCN exhibit the highest mobilities is also in agreement with the larger degree of absorption peak broadening and apparent oriented attachment and crystallographic fusion of nanocrystals revealed by TEM.

Mobility values of << 1 $cm^2/V{\cdot}s$ are usually an indication of thermally activated transport, as discussed above. These models are based upon amorphous systems, which in many ways are analogous to QD solid films because of the localization introduced by

quantum confinement. Relatively recent measurements of amorphous semiconductors show mobility values of μ_H(295K) = 0.07 cm^2/V·s with the activation energy for conduction in the range of $\epsilon_{A\sigma}$ = 360 – 430 meV for amorphous $Ge_2Sb_2Te_5$,(*160*) and μ_H(295K) = 0.13 cm^2/V·s, with $\epsilon_{A\sigma}$ = 240 – 300 meV compared to ϵ_{AHall} = 50 meV for amorphous Sb_2Te_3.(*141*) In the Sb_2Te_3 study, the Hall mobility shows a weak inverse temperature dependence. This, together with the low value of the Hall mobility and $\epsilon_{AHall} < \epsilon_{A\sigma}$ is in agreement with the small polaron hopping model.

In comparison, temperature dependent transport studies on PbSe nanocrystal films have shown that the activation energy for conductivity is ligand dependent, with MPA and EDT having $\epsilon_{A\sigma}$ ~ 24 meV, and SCN and TBAI showing little temperature dependence on conductivity between 200-300K and $\epsilon_{A\sigma}$ ~10 meV at low temperatures. For SCN followed by a $PbCl_2$ treatment, the electron conductivity increases slightly from 300 to 200 K and below 200K, $\epsilon_{A\sigma}$ ~10 meV.(*112*) In nanocrystalline pyrite films, there is a flip of the Hall sign from normal to anomalous at lower temperatures, with $\epsilon_{A\sigma}$= 5 meV and μ_H = 0.1 – 1 cm^2/V·s.(*115*)

The only study to thus far measure the temperature dependence of Hall mobility for quantum dot NC films is on InAs NCs.(*116*) The study compares the temperature dependence of FET and Hall mobilities. For the films still within the realm of thermally activated transport (~1 cm^2/V·s), ϵ_{AFET} = 10.4 meV, ϵ_{AHall} = 10.8 meV (300-120K) and 2.0 meV (50-10K). Hall and FET mobilities at room temperature were comparable, but diverged at lower temperatures with $\mu_H > \mu_{FET}$. Therefore, $\epsilon_{AHall} \approx \epsilon_{AFET}$ at higher

temperatures and $\epsilon_{AHall} < \epsilon_{AFET}$, though it should be noted that ϵ_{AFET} and $\epsilon_{A\sigma}$ are not necessarily comparable as conductivity in an FET is influenced by the gating effect. What is interesting, however, in the case of all the above transport studies on NC films is that though they are indicative of a thermally activated hopping transport mechanism due to the low Hall mobilities and thermally activated conduction, all of the activation energies are significantly lower (by about an order of magnitude) than the activation energies of the aforementioned amorphous semiconductors. This could suggest that NC films are in an intermediate state where there are combined effects of both strongly and weakly bound carriers.(*161*, *162*) The demonstration of measuring Hall mobilities in high resistivity, low mobility NC films via the AC Hall method provides a framework of empirical data for a specific regime of transport which appears to be somewhere in between strongly localized carrier transport in atomically amorphous systems and classic, delocalized systems.

In conclusion, we use the AC magnetic-field, Hall measurement coupled with the Seebeck measurement to determine the mobility, carrier type, and an estimation of the carrier concentration within high resistivity, low mobility NC films. The Hall measurement for all the treatments under investigation exhibited a positive Hall sign, with mobilities from 0.01 – 1.9 $cm^2/V{\cdot}s$, with the exception of $ZnCl_2$, which consistently had a negative Hall sign. We show that these measurements offer a complement to FET measurements, particularly for highly doped films. Furthermore, we compare the magnitude of mobilities we calculated with those in the literature on amorphous

semiconductors and other NC film systems as well as their activation energies. We conclude that although the low Hall mobilities (<< 1 $cm^2/V{\cdot}s$) are indicative of heat activated, hopping transport, the complementary activation energies for conduction are an order of magnitude less than an atomically amorphous system. Therefore, the mechanism of transport is likely a combination of both strong and weakly bound carriers. Data from these measurements, coupled with optical data from absorption measurements and structural data from XRD and TEM, shows that the choice of ligand treatment dramatically affects mobility, carrier concentration, and film resistivity *via* contributions from particle spacing, particle orientation and/or degree of crystallographic fusion, degree of electronic coupling. Furthermore, this work establishes motivation for a revitalization of the theoretical models to describe Hall mobility transport in these materials, including a need for additional temperature dependent Hall mobility measurements, ideally coupled with experiments to determine the conductivity mobility so that and appropriate Hall factor (r_H) can be defined for these systems.

4.8 Experimental Details Specific to Work Presented in Chapter 4

4.8.1 Van der Pauw Calculations

Resistivity is calculated using the van der Pauw method. The setup is shown in **Figure 4.11**.

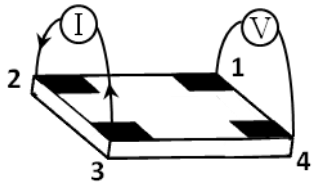

Figure 4.11: *A representation of the van der Pauw measurement setup.*

The van der Pauw equation (Equation 20) is used for a series of eight measurements total that are averaged together to calculate the final resistivity (ρ). $R_{21,34}^{CR}$ means the resistance calculated (using Ohm's Law) from the average of the current reversal (Equation 21) measurement where current is applied positive, then negative across electrodes 1 and 2 while the voltage is measured across electrodes 3 and 4.

Equation 20

$$\rho_A = \frac{\pi F\left(R_{21,34}^{CR} + R_{32,41}^{CR}\right)}{2ln(2)} \qquad \rho_B = \frac{\pi F\left(R_{43,12}^{CR} + R_{14,23}^{CR}\right)}{2ln(2)}$$

Equation 21

$$R_{21,34}^{CR} = \frac{R_{21,34}^{I+} + R_{12,34}^{I-}}{2}$$

F is a factor that takes into account sample asymmetry and has the relationship shown in Equation 22, where R_r is the greater of the ratios $R_{21,34}/ R_{23,14}$ and $R_{23,14}/R_{21,34}$ (and analog for ρ_B).

Equation 22

$$\frac{R_r - 1}{R_r + 1} = \frac{F}{ln(2)} \cos^{-1}\left(\frac{e^{\frac{ln(2)}{F}}}{2}\right)$$

Equation 23

$$\rho = \frac{\rho_A + \rho_B}{2}$$

4.8.2 Table of Alpha Values

Table 3 shows how sensitivity of the DC Hall measurement scales with α, which contributes to the misalignment voltage (V_O) as described in Equation 15 above. The value of α becomes more significant with decreasing film symmetry, where *w/l* is the ratio of sample width to length. The values calculated for mobility (μ) assumes a 1 T magnetic field (*B*). Even with an alpha value of 0.014, corresponding to a sample length to width ratio of 0.99, if the magnetic field is 1 T and the mobility is 0.14 $cm^2/V*s$, the misalignment voltage is already three orders of magnitude larger than the Hall voltage: 0.014/(0.000014 $m^2/V*s$ x 1 T) = 1000.

w/l	α	μ ($cm^2/V*s$) = α/B = (1/1T)
1	0	
0.99	0.014	140
0.9	0.14	1400
0.5	1.11	11100

Table 3: *Alpha values for a rectangular film with point contacts.*(*146*)

4.8.3 Ohmic Checks

Each sample was confirmed to exhibit ohmic behavior before performing the AC Hall measurement (**Figure 4.12**). At set intervals over a selected range, an excitation current was applied separately across each diagonal (1-3, 2-4) at set intervals over a selected range from negative to positive. For the Hall measurement, an excitation current that resulted in less than 1 V was generally found to be an appropriate balance between signal and noise. The excitation current value used for each sample was selected from within the region displaying ohmic behavior.

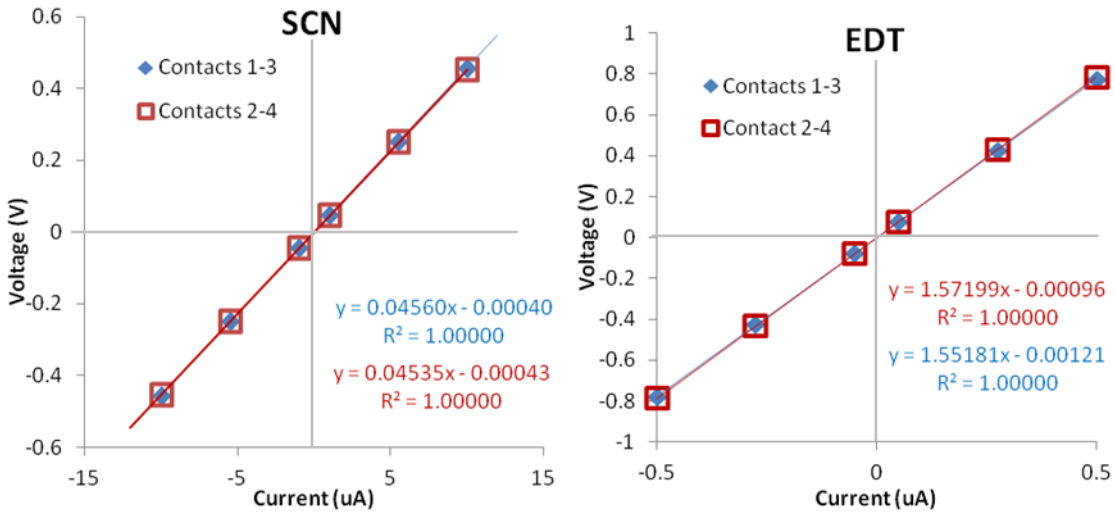

Figure 4.12: *Example I-V curves showing ohmic behavior in the films before AC Hall measurement.*

4.8.4 Film Imaging

A JEOL 7500F SEM was used to study the surface of the films. **Figure 4.13** shows the surface of a spin coated PbSe NC film exchanged with TBAI taken. Cracks are caused by the decrease in overall volume due to the solid phase ligand exchange process and are infilled by sequential film depositions.

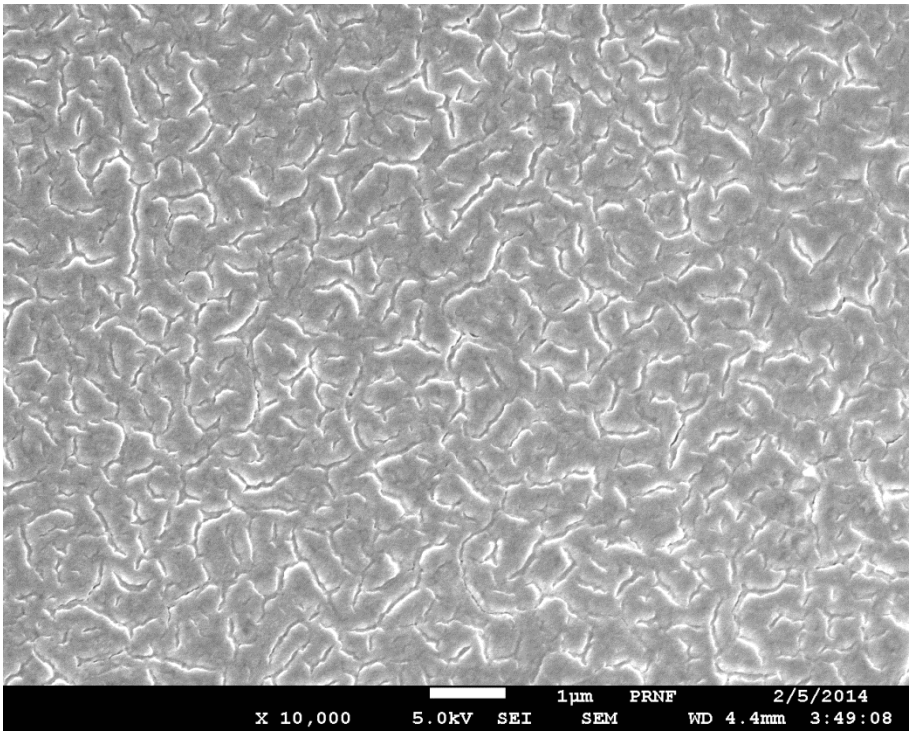

Figure 4.13: *SEM of the surface of TBAI exchanged NC film.*

Figure 4.14 is a HR-TEM image of a SCN treated PbSe nanocrystal film. Particles appear to orient in along the <100> direction, consistent with similar work done by Hanrath *et al*(*34*).

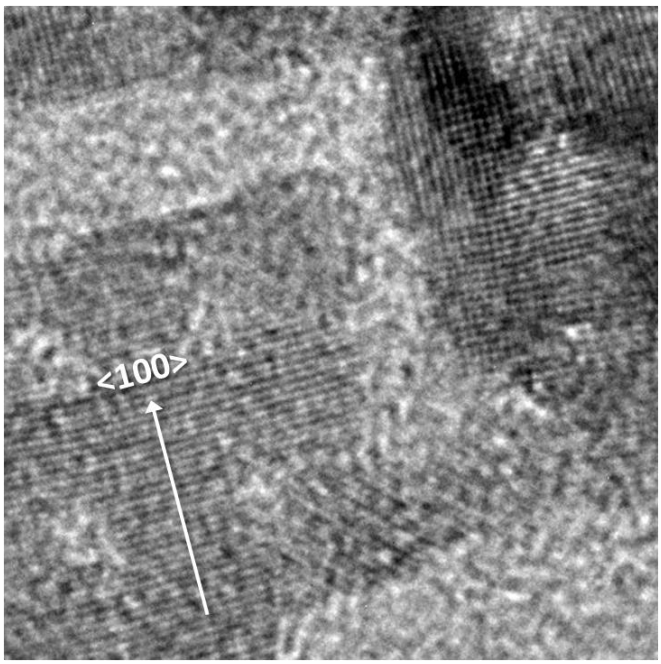

Figure 4.14: *High resolution TEM image showing oriented attachment and fusing of {100} facets in a SCN treated PbSe NC film.*

4.8.5 PbSe NC Synthesis

Synthesis of 6.0 nm PbSe nanocrystals used a previously published method with a slight modification to improve yield(*46*, *47*). Synthesis was performed under nitrogen using a Schlenk line system and transfer of the reaction solution to a Schlenk tube *via* cannula. A solution of 892 mg PbO, 3 mL of oleic acid, and 20 mL of ODE was heated to 120 °C and degassed for 1.5 hours under vacuum. Afterward, the temperature was raised to 160 °C, at which 8 mL of 1M TOP-Se combined with 69 μL of DPP was rapidly injected into the solution. After 80 sec of reaction time, the solution was quenched to room temperature using an ice bath. The nanocrystals were purified within a nitrogen glove box by first adding 2 mL of hexane to the reaction solution, then precipitating the solution

with 1:1 ethanol/butanol and centrifuging at 8000 rpm for 3 min and then redispersing in 4 mL of hexane. The wash process was repeated two more times before the nanocrystals were dispersed in 10 mL of hexane and stored in the glove box in the dark. Before deposition, the nanocrystal solution was dried under vacuum to remove the hexane, and then re-dispersed in octane at the desired concentration.

4.8.6 Film Deposition and Ligand Exchange

Coverglass slides were pretreated by first sonicating in a DI water/detergent solution for 20 min, followed by sonication in a 1:1:1 mixture of DI water:acetone:ethanol solution, treatment under UV-ozone with pure O_2 for 30 min, then finally submerged in a 1 vol% mixture of MPTS in anhydrous toluene for ~12 hours. Substrates were then rinsed with toluene and sonicated in ethanol for 5 min. The coverglass was fixed to a ~1x1 inch piece of glass with a gel-pack square and mounted on the spin coater. The ligand solutions were prepared as: 10 mM BDT in ACN, 27 mM (10.1 mg/mL) TBAI in methanol, 0.01M EDT in ACN, 1 mM Na_2S in methanol, 1 mM Na_2Se in methanol, 130 mM (10 mg/mL) SCN in ACN, 100 mM $ZnCl_2$ in ethylene glycol (also soluble in acetone), 50 mM $PbCl_2$ in or olyelamine. 2 drops of the nanocrystal solution (~35 mg/mL in 5:1 octane:hexane) were dispensed on the surface and immediately spun at a rate of 800-1500 rpm until the film dried. 6 drops (~300 uL) of the ligand exchange solution were dispensed onto the film surface, enough to completely cover, and allowed to sit for 30 sec, except for 3 min for EDT and $ZnCl_2$. The solution was then spun off until dry, then rinsed with ~6 drops of pure solvent (same as the dispersive solvent except for the $ZnCl_2$ treatment, which was

rinsed first with ethylene glycol, then twice with acetone), then pure octane. For the Na_2S and SCN exchanges followed by $PbCl_2$ treatments, the films were soaked in the $PbCl_2$/oleylamine solution at 85°C for 24 hours, then immediately rinsed twice with hexane followed by acetone while drying with a nitrogen stream after each rinse. This procedure was repeated twice for optical measurements, 5 times for the x-ray measurements, and 8 times for AC Hall measurements. AC Hall films were individually measured by AFM for carrier density calculations and had thicknesses 120-280 nm.

4.8.7 Measurement and Characterization

Seebeck – Measurements were taken using an MMR SB-100 sontroller with MMR K-20 temperature controller.

Van der Pauw/AC Hall – 50 nm thick Au or Ag electrodes 1 mm^2 were deposited in a square geometry 2.5 mm apart *via* thermal evaporation (Angstrom). The edges of the film to be measured were then defined by carefully scratching away a perimeter. In order to prepare the films for the AC Hall measurement system, which is out in air, silver paste was used to draw out leads from the contacts of the films so that the film could then be sealed using a coverglass slip and epoxy. **Figure 4.15** shows the as prepared films with deposited electrodes and encapsulation.

Figure 4.15: *Photo of prepared film for AC Hall measurement.*

Samples where then stored in sealed jars under nitrogen during transport, and not opened until the measurement was to be made. Measurements were performed using a Lakeshore 8404 AC/DC Hall Effect Measurement System at a field of 1.25 T and frequency of 100 mHz located in the Center for Functional Nanomaterials (CFN) at Brookhaven National Laboratory (BNL).

5 APPENDIX: CHEMICALS USED IN THIS WORK

Tri-n-octylphosphine (TOP, 90%), diphenylphosphine (DPP, 98%), lead oxide (PbO, 99.999%), lead chloride ($PbCl_2$, 99.999%), zinc chloride ($ZnCl_2$, 99.999%), selenium pellets (Se, 99.999%), (3-mercaptopropyl)trimethoxysilane (MPTS, 95%), ammonium thiocyanate (99+%), 1,2- ethanedithiol (EDT, >98%), 1,3-benzenedithiol (BDT, >98%), Oleic acid (OA, 90%), oleylamine (OLA, 70%), hexamethyldisilathiane (HMDS, 98%), anhydrous methanol, anhydrous ethanol, anhydrous 2-propanol, anhydrous acetonitrile (ACN), anhydrous hexane, and anhydrous toluene were purchased from Aldrich. The ammonium thiocyanate was further dried by dissolving in methanol, recrystallizing, and drying under vacuum on a schlenk line. Anhydrous hexane, anhydrous toluene, and anhydrous acetonitrile (ACN) were dried using an alumina column. Ethanol was dried using standard procedures. Anhydrous acetone, 1-octadecene (ODE, 90%), bis-(trimethylsilyl) sulfide (TMS, 95%), n-octyltriethoxysilane (OTS, 97%), Dodecanethiol (DDT, 98%), tetrabutylammonium iodide (TBAI, 98%), 1.6 M solution of butyl lithium in THF were purchased from Acros. N-octadecylphosphonic acid (ODPA, PCI synthesis, 99%) was purchased from PCI synthesis. Anhydrous sodium sulfide (Na_2S) and sodium selenide (Na_2Se, 99.8%) was purchased from Alfa Aesar. Silver paste (Leitsilber 200) and coverglass substrates (Gold Seal No. 2, 22x22 mm) were from Ted Pella. Epoxy used for sealing is a 5 minute, 2 part epoxy from ITW Devcon.

6 BIBLIOGRAPHY

(1) Moreels, I.; Lambert, K.; Smeets, D.; De Muynck, D.; Nollet, T.; Martins, J. C.; Vanhaecke, F.; Vantomme, A.; Delerue, C.; Allan, G.; Hens, Z. Size-dependent optical properties of colloidal PbS quantum dots. *ACS Nano* **2009**, *3*, 3023–30.

(2) Murray, C. B.; Kagan, C. R.; Bawendi, M. G. Synthesis and Characterization of Monodisperse Nanocrystals and Close-Packed Nanocrystal Assemblies. *Annu. Rev. Mater. Sci.* **2000**, *30*, 545–610.

(3) Khare, A.; Wills, A. W.; Ammerman, L. M.; Norris, D. J.; Aydil, E. S. Size control and quantum confinement in Cu2ZnSnS4 nanocrystals. *Chem. Commun. (Camb).* **2011**, *47*, 11721–3.

(4) Talgorn, E.; Gao, Y.; Aerts, M.; Kunneman, L. T.; Schins, J. M.; Savenije, T. J.; van Huis, M. a; van der Zant, H. S. J.; Houtepen, A. J.; Siebbeles, L. D. a Unity quantum yield of photogenerated charges and band-like transport in quantum-dot solids. *Nat. Nanotechnol.* **2011**, *6*, 733–9.

(5) Beard, M. C.; Midgett, A. G.; Law, M.; Semonin, O. E.; Ellingson, R. J.; Nozik, A. J. Variations in the quantum efficiency of multiple exciton generation for a series of chemically treated PbSe nanocrystal films. *Nano Lett.* **2009**, *9*, 836–45.

(6) Ellingson, R. J.; Beard, M. C.; Johnson, J. C.; Yu, P.; Micic, O. I.; Nozik, A. J.; Shabaev, A.; Efros, A. L. Highly efficient multiple exciton generation in colloidal PbSe and PbS quantum dots. *Nano Lett.* **2005**, *5*, 865–871.

(7) Semonin, O. E.; Luther, J. M.; Choi, S.; Chen, H.-Y.; Gao, J.; Nozik, a. J.; Beard, M. C. Peak External Photocurrent Quantum Efficiency Exceeding 100% via MEG in a Quantum Dot Solar Cell. *Science (80-.).* **2011**, *334*, 1530–1533.

(8) Tisdale, W. a; Williams, K. J.; Timp, B. a; Norris, D. J.; Aydil, E. S.; Zhu, X.-Y. Hot-electron transfer from semiconductor nanocrystals. *Science* **2010**, *328*, 1543–7.

(9) Murray, C. B.; Norris, D. J.; Bawendi, M. G. Synthesis and characterization of nearly monodisperse CdE (E = sulfur, selenium, tellurium) semiconductor nanocrystallites. *J. Am. Chem. Soc.* **1993**, *115*, 8706–8715.

(10) Hines, M. A.; Scholes, G. D. Colloidal PbS Nanocrystals with Size-Tunable Near-Infrared Emission: Observation of Post-Synthesis Self-Narrowing of the Particle Size Distribution. *Adv. Mater.* **2003**, *15*, 1844–1849.

(11) Cox, J. A quantum paintbox. www.rsc.org/chemistryworld/Issues/2003/September/paintbox.asp.

(12) Smith, A. M.; Nie, S. Semiconductor Nanocrystals: Structure, Properties, and Band Gap Engineering. *Acc. Chem. Res.* **2010**, *43*, 190–200.

(13) Han, M.; Gao, X.; Su, J. Z.; Nie, S. Quantum-dot-tagged microbeads for multiplexed optical coding of biomolecules. *Nat. Biotechnol.* **2001**, *19*, 631–5.

(14) Chou, K.; Dennis, A. Förster Resonance Energy Transfer between Quantum Dot Donors and Quantum Dot Acceptors. *Sensors* **2015**, *15*, 13288–13325.

(15) Kim, T.-H.; Cho, K.-S.; Lee, E. K.; Lee, S. J.; Chae, J.; Kim, J. W.; Kim, D. H.; Kwon, J.-Y.; Amaratunga, G.; Lee, S. Y.; Choi, B. L.; Kuk, Y.; Kim, J. M.; Kim, K. Full-colour quantum dot displays fabricated by transfer printing. *Nat. Photonics* **2011**, *5*, 176–182.

(16) Konstantatos, G.; Howard, I.; Fischer, A.; Hoogland, S.; Clifford, J.; Klem, E.; Levina, L.; Sargent, E. H. Ultrasensitive solution-cast quantum dot photodetectors. *Nature* **2006**, *442*, 180–3.

(17) Zrazhevskiy, P.; Gao, X. Quantum dot imaging platform for single-cell molecular profiling. *Nat. Commun.* **2013**, *4*, 1619.

(18) Talapin, D. V; Murray, C. B. PbSe nanocrystal solids for n- and p-channel thin film field-effect transistors. *Science* **2005**, *310*, 86–9.

(19) Oh, S. J.; Berry, N. E.; Choi, J.-H.; Gaulding, E. A.; Paik, T.; Hong, S.-H.; Murray, C. B.; Kagan, C. R. Stoichiometric control of lead chalcogenide nanocrystal solids to enhance their electronic and optoelectronic device performance. *ACS Nano* **2013**, *7*, 2413–21.

(20) Liu, Y.; Tolentino, J.; Gibbs, M.; Ihly, R.; Perkins, C. L.; Liu, Y.; Crawford, N.; Hemminger, J. C.; Law, M. PbSe quantum dot field-effect transistors with air-stable electron mobilities above 7 cm2 V(-1) s(-1). *Nano Lett.* **2013**, *13*, 1578–87.

(21) Ko, D.-K.; Kang, Y.; Murray, C. B. Enhanced thermopower via carrier energy filtering in solution-processable Pt-Sb2Te3 nanocomposites. *Nano Lett.* **2011**, *11*, 2841–4.

(22) Ong, W.-L.; Rupich, S. M.; Talapin, D. V; McGaughey, A. J. H.; Malen, J. a Surface chemistry mediates thermal transport in three-dimensional nanocrystal arrays. *Nat. Mater.* **2013**, *12*, 410–5.

(23) Scheele, M.; Oeschler, N.; Veremchuk, I.; Peters, S.-O.; Littig, A.; Kornowski, A.; Klinke, C.; Weller, H. Thermoelectric properties of lead chalcogenide core-shell nanostructures. *ACS Nano* **2011**, *5*, 8541–51.

(24) Luther, J. M.; Law, M.; Beard, M. C.; Song, Q.; Reese, M. O.; Ellingson, R. J.; Nozik, A. J. Schottky solar cells based on colloidal nanocrystal films. *Nano Lett.* **2008**, *8*, 3488–92.

(25) Ma, W.; Swisher, S. L.; Ewers, T.; Engel, J.; Ferry, V. E.; Atwater, H. a; Alivisatos, a P. Photovoltaic performance of ultrasmall PbSe quantum dots. *ACS Nano* **2011**, *5*, 8140–7.

(26) Ip, A. H.; Thon, S. M.; Hoogland, S.; Voznyy, O.; Zhitomirsky, D.; Debnath, R.; Levina, L.; Rollny, L. R.; Carey, G. H.; Fischer, A.; Kemp, K. W.; Kramer, I. J.; Ning, Z.; Labelle, A. J.; Chou, K. W.; Amassian, A.; Sargent, E. H. Hybrid passivated colloidal quantum dot solids. *Nat. Nanotechnol.* **2012**, *7*, 577–82.

(27) Zhang, J.; Gao, J.; Miller, E. M.; Luther, J. M.; Beard, M. C. Diffusion-Controlled Synthesis of PbS and PbSe Quantum Dots with in Situ Halide Passivation for Quantum Dot Solar Cells. *ACS Nano* **2014**, *8*, 614–22.

(28) Wang, X.; Koleilat, G. I.; Tang, J.; Liu, H.; Kramer, I. J.; Debnath, R.; Brzozowski, L.; Barkhouse, D. A. R.; Levina, L.; Hoogland, S.; Sargent, E. H. Tandem colloidal quantum dot solar cells employing a graded recombination layer. *Nat. Photonics* **2011**, *5*, 480–484.

(29) Kim, D. K.; Lai, Y.; Diroll, B. T.; Murray, C. B.; Kagan, C. R. Flexible and low-voltage integrated circuits constructed from high-performance nanocrystal transistors. *Nat. Commun.* **2012**, *3*, 1216.

(30) Yu, W. W.; Falkner, J. C.; Shih, B. S.; Colvin, V. L. Preparation and Characterization of Monodisperse PbSe Semiconductor Nanocrystals in a Noncoordinating Solvent. *Chem. Mater.* **2004**, *16*, 3318–3322.

(31) Fafarman, A. T.; Koh, W.; Diroll, B. T.; Kim, D. K.; Ko, D.; Oh, S. J.; Ye, X.; Doan-Nguyen, V.; Crump, M. R.; Reifsnyder, D. C.; Murray, C. B.; Kagan, C. R. Thiocyanate-capped nanocrystal colloids: vibrational reporter of surface chemistry and solution-based route to enhanced coupling in nanocrystal solids. *J. Am. Chem. Soc.* **2011**, *133*, 15753–61.

(32) Ning, Z.; Ren, Y.; Hoogland, S.; Voznyy, O.; Levina, L.; Stadler, P.; Lan, X.; Zhitomirsky, D.; Sargent, E. H. All-inorganic colloidal quantum dot photovoltaics employing solution-phase halide passivation. *Adv. Mater.* **2012**, *24*, 6295–9.

(33) Lee, J.-S.; Kovalenko, M. V; Huang, J.; Chung, D. S.; Talapin, D. V Band-like transport, high electron mobility and high photoconductivity in all-inorganic nanocrystal arrays. *Nat. Nanotechnol.* **2011**, *6*, 348–52.

(34) Hanrath, T.; Veldman, D.; Choi, J. J.; Christova, C. G.; Wienk, M. M.; Janssen, R. a J. PbSe nanocrystal network formation during pyridine ligand displacement. *ACS Appl. Mater. Interfaces* **2009**, *1*, 244–50.

(35) Luther, J. M.; Law, M.; Song, Q.; Perkins, C. L.; Beard, M. C.; Nozik, A. J. Structural, optical, and electrical properties of self-assembled films of PbSe nanocrystals treated with 1,2-ethanedithiol. *ACS Nano* **2008**, *2*, 271–80.

(36) Koleilat, G. I.; Levina, L.; Shukla, H.; Myrskog, S. H.; Hinds, S.; Pattantyus-Abraham, A. G.; Sargent, E. H. Efficient, stable infrared photovoltaics based on solution-cast colloidal quantum dots. *ACS Nano* **2008**, *2*, 833–40.

(37) Leschkies, K. S.; Divakar, R.; Basu, J.; Enache-Pommer, E.; Boercker, J. E.; Carter, C. B.; Kortshagen, U. R.; Norris, D. J.; Aydil, E. S. Photosensitization of ZnO nanowires with CdSe quantum dots for photovoltaic devices. *Nano Lett.* **2007**, *7*, 1793–8.

(38) Lazarenkova, O. L.; Balandin, A. a. Miniband formation in a quantum dot crystal. *J. Appl. Phys.* **2001**, *89*, 5509.

(39) Shabaev, A.; Efros, A. L.; Efros, A. L. Dark and photo-conductivity in ordered array of nanocrystals. *Nano Lett.* **2013**, *13*, 5454–61.

(40) Liu, Y.; Gibbs, M.; Puthussery, J.; Gaik, S.; Ihly, R.; Hillhouse, H. W.; Law, M. Dependence of carrier mobility on nanocrystal size and ligand length in PbSe nanocrystal solids. *Nano Lett.* **2010**, *10*, 1960–9.

(41) Oh, S. J.; Berry, N. E.; Choi, J.-H.; Gaulding, E. A.; Lin, H.; Paik, T.; Diroll, B. T.; Muramoto, S.; Murray, C. B.; Kagan, C. R. Designing high-performance PbS and PbSe nanocrystal electronic devices through stepwise, post-synthesis, colloidal atomic layer deposition. *Nano Lett.* **2014**, *14*, 1559–66.

(42) Moreels, I.; Fritzinger, B.; Martins, J. C.; Hens, Z. Surface chemistry of colloidal PbSe nanocrystals. *J. Am. Chem. Soc.* **2008**, *130*, 15081–15086.

(43) Cargnello, M.; Diroll, B. T.; Gaulding, E. A.; Murray, C. B. Enhanced energy transfer in quasi-quaternary nanocrystal superlattices. *Adv. Mater.* **2014**, *26*, 2419–23.

(44) Dong, A.; Jiao, Y.; Milliron, D. J. Electronically Coupled Nanocrystal Superlattice Films by in Situ Ligand Exchange at the Liquid-Air Interface. *ACS Nano* **2013**.

(45) Urban, J. J.; Talapin, D. V; Shevchenko, E. V; Kagan, C. R.; Murray, C. B. Synergism in binary nanocrystal superlattices leads to enhanced p-type

conductivity in self-assembled PbTe/Ag2Te thin films. *Nat. Mater.* **2007**, *6*, 115–121.

(46) Steckel, J. S.; Yen, B. K. H.; Oertel, D. C.; Bawendi, M. G. On the mechanism of lead chalcogenide nanocrystal formation. *J. Am. Chem. Soc.* **2006**, *128*, 13032–3.

(47) Yu, W. W.; Falkner, J. C.; Shih, B. S.; Colvin, V. L. Preparation and Characterization of Monodisperse PbSe Semiconductor Nanocrystals in a Noncoordinating Solvent. *Chem. Mater.* **2004**, *16*, 3318–3322.

(48) Yarema, M.; Kovalenko, M. V; Hesser, G.; Talapin, D. V; Heiss, W. Highly monodisperse bismuth nanoparticles and their three-dimensional superlattices. *J. Am. Chem. Soc.* **2010**, *132*, 15158–9.

(49) Bao, N.; Shen, L.; Wang, Y.; Padhan, P.; Gupta, A. A facile thermolysis route to monodisperse ferrite nanocrystals. *J. Am. Chem. Soc.* **2007**, *129*, 12374–5.

(50) Akhavan, V. A.; Goodfellow, B. W.; Panthani, M. G.; Reid, D. K.; Hellebusch, D. J.; Adachi, T.; Korgel, B. A. Spray-deposited CuInSe2 nanocrystal photovoltaics. *Energy Environ. Sci.* **2010**, *3*, 1600.

(51) Law, M.; Luther, J. M.; Song, Q.; Hughes, B. K.; Perkins, C. L.; Nozik, A. J. Structural, optical, and electrical properties of PbSe nanocrystal solids treated thermally or with simple amines. *J. Am. Chem. Soc.* **2008**, *130*, 5974–85.

(52) Tang, J.; Kemp, K. W.; Hoogland, S.; Jeong, K. S.; Liu, H.; Levina, L.; Furukawa, M.; Wang, X.; Debnath, R.; Cha, D.; Chou, K. W.; Fischer, A.; Amassian, A.; Asbury, J. B.; Sargent, E. H. Colloidal-quantum-dot photovoltaics using atomic-ligand passivation. *Nat. Mater.* **2011**, *10*, 765–71.

(53) Talapin, D. V.; Shevchenko, E. V; Kornowski, A.; Gaponik, N.; Haase, M.; Rogach, A. L.; Weller, H. A New Approach to Crystallization of CdSe Nanoparticles into Ordered Three-Dimensional Superlattices. *Adv. Mater.* **2001**, *13*, 1868.

(54) Murray, C. B.; Kagan, C. R.; Bawendi, M. G. Self-Organization of CdSe

Nanocrystallites into Three-Dimensional Quantum Dot Superlattices. *Science (80-.).* **1995**, *270*, 1335–1338.

(55) de Nijs, B.; Dussi, S.; Smallenburg, F.; Meeldijk, J. D.; Groenendijk, D. J.; Filion, L.; Imhof, A.; van Blaaderen, A.; Dijkstra, M. Entropy-driven formation of large icosahedral colloidal clusters by spherical confinement. *Nat. Mater.* **2014**, 1–5.

(56) Baranov, D.; Fiore, A.; van Huis, M.; Giannini, C.; Falqui, A.; Lafont, U.; Zandbergen, H.; Zanella, M.; Cingolani, R.; Manna, L. Assembly of colloidal semiconductor nanorods in solution by depletion attraction. *Nano Lett.* **2010**, *10*, 743–9.

(57) Wang, T.; Zhuang, J.; Lynch, J.; Chen, O.; Wang, Z.; Wang, X.; LaMontagne, D.; Wu, H.; Wang, Z.; Cao, Y. C. Self-assembled colloidal superparticles from nanorods. *Science* **2012**, *338*, 358–63.

(58) Nagaoka, Y.; Chen, O.; Wang, Z.; Cao, Y. C. Structural control of nanocrystal superlattices using organic guest molecules. *J. Am. Chem. Soc.* **2012**, *134*, 2868–71.

(59) Shevchenko, E. V; Talapin, D. V; Kotov, N. A.; O'Brien, S.; Murray, C. B. Structural diversity in binary nanoparticle superlattices. *Nature* **2006**, *439*, 55–9.

(60) Sun, S.; Murray, C. B. Synthesis of monodisperse cobalt nanocrystals and their assembly into magnetic superlattices (invited). *J. Appl. Phys.* **1999**, *85*, 4325.

(61) Boles, M. A.; Talapin, D. V Self-assembly of tetrahedral CdSe nanocrystals: effective "patchiness" via anisotropic steric interaction. *J. Am. Chem. Soc.* **2014**, *136*, 5868–71.

(62) Smith, D. K.; Goodfellow, B.; Smilgies, D.; Korgel, B. A. Self-assembled simple hexagonal AB(2) binary nanocrystal superlattices: SEM, GISAXS, and defects. *J. Am. Chem. Soc.* **2009**, *131*, 3281–90.

(63) Disch, S.; Wetterskog, E.; Hermann, R. P.; Salazar-Alvarez, G.; Busch, P.; Brückel, T.; Bergström, L.; Kamali, S. Shape induced symmetry in self-assembled

mesocrystals of iron oxide nanocubes. *Nano Lett.* **2011**, *11*, 1651–6.

(64) Disch, S.; Wetterskog, E.; Hermann, R. P.; Korolkov, D.; Busch, P.; Boesecke, P.; Lyon, O.; Vainio, U.; Salazar-Alvarez, G.; Bergström, L.; Brückel, T. Structural diversity in iron oxide nanoparticle assemblies as directed by particle morphology and orientation. *Nanoscale* **2013**, *5*, 3969–75.

(65) Park, S. Y.; Lytton-Jean, A. K. R.; Lee, B.; Weigand, S.; Schatz, G. C.; Mirkin, C. a DNA-programmable nanoparticle crystallization. *Nature* **2008**, *451*, 553–6.

(66) Macfarlane, R. J.; Jones, M. R.; Lee, B.; Auyeung, E.; Mirkin, C. a Topotactic interconversion of nanoparticle superlattices. *Science* **2013**, *341*, 1222–5.

(67) Nykypanchuk, D.; Maye, M. M.; van der Lelie, D.; Gang, O. DNA-guided crystallization of colloidal nanoparticles. *Nature* **2008**, *451*, 549–52.

(68) Zhang, Y.; Lu, F.; Yager, K. G.; van der Lelie, D.; Gang, O. A general strategy for the DNA-mediated self-assembly of functional nanoparticles into heterogeneous systems. *Nat. Nanotechnol.* **2013**, *8*, 865–72.

(69) Boneschanscher, M. P.; Evers, W. H.; Geuchies, J. J.; Altantzis, T.; Goris, B.; Rabouw, F. T.; van Rossum, S. A. P.; van der Zant, H. S. J.; Siebbeles, L. D. A.; Van Tendeloo, G.; Swart, I.; Hilhorst, J.; Petukhov, A. V; Bals, S.; Vanmaekelbergh, D. Long-range orientation and atomic attachment of nanocrystals in 2D honeycomb superlattices. *Science* **2014**, *344*, 1377–80.

(70) Dabbousi, B. O.; Murray, C. B.; Rubner, M. F.; Bawendi, M. G. Langmuir-Blodgett Manipulation of Size-Selected CdSe Nanocrystallites. *Chem. Mater.* **1994**, *6*, 216–219.

(71) Dong, A.; Chen, J.; Vora, P. M.; Kikkawa, J. M.; Murray, C. B. Binary nanocrystal superlattice membranes self-assembled at the liquid-air interface. *Nature* **2010**, *466*, 474–7.

(72) Tao, A.; Sinsermsuksakul, P.; Yang, P. Tunable plasmonic lattices of silver nanocrystals. *Nat. Nanotechnol.* **2007**, *2*, 435–40.

(73) Lau, C. Y.; Duan, H.; Wang, F.; He, C. Bin; Low, H. Y.; Yang, J. K. W. Enhanced ordering in gold nanoparticles self-assembly through excess free ligands. *Langmuir* **2011**, *27*, 3355–60.

(74) Bodnarchuk, M. I.; Kovalenko, M. V; Pichler, S.; Fritz-Popovski, G.; Hesser, G.; Heiss, W. Large-area ordered superlattices from magnetic Wustite/cobalt ferrite core/shell nanocrystals by doctor blade casting. *ACS Nano* **2010**, *4*, 423–31.

(75) Talgorn, E.; de Vries, M. a; Siebbeles, L. D. A.; Houtepen, A. J. Photoconductivity Enhancement in Multilayers of CdSe and CdTe Quantum Dots. *ACS Nano* **2011**, *5*, 3552–8.

(76) Gao, Y.; Aerts, M.; Sandeep, C. S. S.; Talgorn, E.; Savenije, T. J.; Kinge, S.; Siebbeles, L. D. A.; Houtepen, A. J. Photoconductivity of PbSe quantum-dot solids: dependence on ligand anchor group and length. *ACS Nano* **2012**, *6*, 9606–14.

(77) Dalmaschio, C. J.; da Silveira Firmiano, E. G.; Pinheiro, A. N.; Sobrinho, D. G.; Farias de Moura, A.; Leite, E. R. Nanocrystals self-assembled in superlattices directed by the solvent-organic capping interaction. *Nanoscale* **2013**, *5*, 5602–10.

(78) Perlich, J.; Schwartzkopf, M.; Körstgens, V.; Erb, D.; Risch, J. F. H.; Müller-Buschbaum, P.; Röhlsberger, R.; Roth, S. V.; Gehrke, R. Pattern formation of colloidal suspensions by dip-coating: An in situ grazing incidence X-ray scattering study. *Phys. status solidi - Rapid Res. Lett.* **2012**, *6*, 253–255.

(79) Kim, D. K.; Lai, Y.; Vemulkar, T. R.; Kagan, C. R. Flexible, low-voltage, and low-hysteresis PbSe nanowire field-effect transistors. *ACS Nano* **2011**, *5*, 10074–83.

(80) Ning, Z.; Voznyy, O.; Pan, J.; Hoogland, S.; Adinolfi, V.; Xu, J.; Li, M.; Kirmani, A. R.; Sun, J.; Minor, J.; Kemp, K. W.; Dong, H.; Rollny, L.; Labelle, A.; Carey, G.; Sutherland, B.; Hill, I.; Amassian, A.; Liu, H.; Tang, J.; Bakr, O. M.; Sargent, E. H. Air-stable n-type colloidal quantum dot solids. *Nat. Mater.* **2014**, *13*, 822–8.

(81) Chuang, C. M.; Brown, P. R.; Bulović, V.; Bawendi, M. G. Improved performance and stability in quantum dot solar cells through band alignment engineering. *Nat. Mater.* **2014**, *13*, 796–801.

(82) Evers, W. H.; De Nijs, B.; Filion, L.; Castillo, S.; Dijkstra, M.; Vanmaekelbergh, D. Entropy-driven formation of binary semiconductor-nanocrystal superlattices. *Nano Lett.* **2010**, *10*, 4235–41.

(83) Hynninen, A.-P.; Filion, L.; Dijkstra, M. Stability of LS and LS2 crystal structures in binary mixtures of hard and charged spheres. *J. Chem. Phys.* **2009**, *131*, 064902.

(84) Ye, X.; Chen, J.; Murray, C. B. Polymorphism in self-assembled AB6 binary nanocrystal superlattices. *J. Am. Chem. Soc.* **2011**, *133*, 2613–20.

(85) Lalatonne, Y.; Richardi, J.; Pileni, M. P. Van der Waals versus dipolar forces controlling mesoscopic organizations of magnetic nanocrystals. *Nat. Mater.* **2004**, *3*, 121–5.

(86) Bodnarchuk, M. I.; Kovalenko, M. V; Heiss, W.; Talapin, D. V Energetic and entropic contributions to self-assembly of binary nanocrystal superlattices: temperature as the structure-directing factor. *J. Am. Chem. Soc.* **2010**, *132*, 11967–77.

(87) Schapotschnikow, P.; Pool, R.; Vlugt, T. J. H. Molecular simulations of interacting nanocrystals. *Nano Lett.* **2008**, *8*, 2930–4.

(88) Acharya, S.; Pradhan, N. Insertion/Ejection of Dopant Ions in Composition Tunable Semiconductor Nanocrystals. *J. Phys. Chem. C* **2011**, *115*, 19513–19519.

(89) Norris, D. J.; Efros, A. L.; Erwin, S. C. Doped nanocrystals. *Science* **2008**, *319*, 1776–9.

(90) Diroll, B. T.; Gordon, T. R.; Gaulding, E. A.; Klein, D. R.; Paik, T.; Yun, H. J.; Goodwin, E. D.; Damodhar, D.; Kagan, C. R.; Murray, C. B. Synthesis of N-Type Plasmonic Oxide Nanocrystals and the Optical and Electrical Characterization of their Transparent Conducting Films. *Chem. Mater.* **2014**, *26*, 4579–4588.

(91) Goodwin, E. D.; Straus, D. B.; Gaulding, E. A.; Murray, C. B.; Kagan, C. R. The effects of inorganic surface treatments on photogenerated carrier mobility and lifetime in PbSe quantum dot thin films. *Chem. Phys.* **2015**.

(92) Wanger, D. D.; Correa, R. E.; Dauler, E. A.; Bawendi, M. G. The dominant role of exciton quenching in PbS quantum-dot-based photovoltaic devices. *Nano Lett.* **2013**, *13*, 5907–12.

(93) Goodwin, E. D.; Diroll, B. T.; Oh, S. J.; Paik, T.; Murray, C. B.; Kagan, C. R. Effects of Post-Synthesis Processing on CdSe Nanocrystals and Their Solids: Correlation between Surface Chemistry and Optoelectronic Properties. *J. Phys. Chem. C* **2014**, *118*, 27097–27105.

(94) Sykora, M.; Koposov, A. Y.; Mcguire, J. A.; Schulze, R. K.; Tretiak, O.; Pietryga, J. M.; Klimov, V. I. Effect of Air Exposure on Surface Properties , Electronic Structure , and. **2010**, *4*, 2021–2034.

(95) Luther, J. M.; Gao, J.; Lloyd, M. T.; Semonin, O. E.; Beard, M. C.; Nozik, A. J. Stability assessment on a 3% bilayer PbS/ZnO quantum dot heterojunction solar cell. *Adv. Mater.* **2010**, *22*, 3704–7.

(96) Crisp, R. W.; Kroupa, D. M.; Marshall, A. R.; Miller, E. M.; Zhang, J.; Beard, M. C.; Luther, J. M. Metal Halide Solid-State Surface Treatment for High Efficiency PbS and PbSe QD Solar Cells. *Sci. Rep.* **2015**, *5*, 9945.

(97) Ip, A. H.; Thon, S. M.; Hoogland, S.; Voznyy, O.; Zhitomirsky, D.; Debnath, R.; Levina, L.; Rollny, L. R.; Carey, G. H.; Fischer, A.; Kemp, K. W.; Kramer, I. J.; Ning, Z.; Labelle, A. J.; Chou, K. W.; Amassian, A.; Sargent, E. H. Hybrid passivated colloidal quantum dot solids. *Nat. Nanotechnol.* **2012**, *7*, 577–82.

(98) Brown, P. R.; Kim, D.; Lunt, R. R.; Zhao, N.; Bawendi, M. G.; Grossman, J. C.; Bulović, V. Energy Level Modification in Lead Sulfide Quantum Dot Thin Films through Ligand Exchange. *ACS Nano* **2014**, *8*, 5863–72.

(99) Santra, P. K.; Kamat, P. V Tandem-layered quantum dot solar cells: tuning the

photovoltaic response with luminescent ternary cadmium chalcogenides. *J. Am. Chem. Soc.* **2013**, *135*, 877–85.

(100) Oh, S. J.; Wang, Z.; Berry, N. E.; Choi, J.-H.; Zhao, T.; Gaulding, E. A.; Paik, T.; Lai, Y.; Murray, C. B.; Kagan, C. R. Engineering charge injection and charge transport for high performance PbSe nanocrystal thin film devices and circuits. *Nano Lett.* **2014**, *14*, 6210–6.

(101) Kasap, S. *THERMOELECTRIC EFFECTS IN METALS: THERMOCOUPLES*; 2001.

(102) Fujita, S.; Suzuki, A. Quantum Theory of Thermoelectric Power (Seebeck Coefficient), Electromotive Force and Measurement in Several Systems. In; 2011.

(103) de Boor, J.; Müller, E. Data analysis for Seebeck coefficient measurements. *Rev. Sci. Instrum.* **2013**, *84*, 065102.

(104) Ko, D.-K.; Murray, C. B. Probing the Fermi energy level and the density of states distribution in PbTe nanocrystal (quantum dot) solids by temperature-dependent thermopower measurements. *ACS Nano* **2011**, *5*, 4810–7.

(105) Ning, Z.; Ren, Y.; Hoogland, S.; Voznyy, O.; Levina, L.; Stadler, P.; Lan, X.; Zhitomirsky, D.; Sargent, E. H. All-inorganic colloidal quantum dot photovoltaics employing solution-phase halide passivation. *Adv. Mater.* **2012**, *24*, 6295–9.

(106) Dey, P.; Paul, J.; Bylsma, J.; Karaiskaj, D.; Luther, J. M.; Beard, M. C.; Romero, A. H. Origin of the temperature dependence of the band gap of PbS and PbSe quantum dots. *Solid State Commun.* **2013**, *165*, 49–54.

(107) Dai, Q.; Zhang, Y.; Wang, Y.; Hu, M. Z.; Zou, B.; Wang, Y.; Yu, W. W. Size-dependent temperature effects on PbSe nanocrystals. *Langmuir* **2010**, *26*, 11435–40.

(108) Pastor-moreno, G.; Riley, D. J. Electrochemical studies of moderately boron doped polycrystalline diamond in non-aqueous solvent. *Electrochim. Acta* **2002**, *47*, 2589–2595.

(109) Choi, J. J.; Lim, Y.-F.; Santiago-Berrios, M. B.; Oh, M.; Hyun, B.-R.; Sun, L.; Bartnik, A. C.; Goedhart, A.; Malliaras, G. G.; Abruña, H. D.; Wise, F. W.; Hanrath, T. PbSe nanocrystal excitonic solar cells. *Nano Lett.* **2009**, *9*, 3749–55.

(110) Hyun, B.; Zhong, Y.; Bartnik, A. C.; Sun, L.; Abrun, H. D.; Wise, F. W.; Goodreau, J. D.; Matthews, J. R.; Leslie, T. M.; Borrelli, N. F. Electron Injection from Colloidal PbS Nanoparticles. *2*.

(111) Zhitomirsky, D.; Furukawa, M.; Tang, J.; Stadler, P.; Hoogland, S.; Voznyy, O.; Liu, H.; Sargent, E. H. N-type colloidal-quantum-dot solids for photovoltaics. *Adv. Mater.* **2012**, *24*, 6181–5.

(112) Oh, S. J.; Wang, Z.; Berry, N. E.; Choi, J.-H.; Zhao, T.; Gaulding, E. A.; Paik, T.; Lai, Y.; Murray, C. B.; Kagan, C. R. Engineering Charge Injection and Charge Transport for High Performance PbSe Nanocrystal Thin Film Devices and Circuits. *Nano Lett.* **2014**, *14*, 6210–6216.

(113) Emin, D. *The Hall Effect and Its Applications*; Chien, C. L.; Westgate, C. R., Eds.; Springer US: Boston, MA, 1980.

(114) Stadler, P.; Sutherland, B. R.; Ren, Y.; Ning, Z.; Simchi, A.; Thon, S. M.; Hoogland, S.; Sargent, E. H. Joint mapping of mobility and trap density in colloidal quantum dot solids. *ACS Nano* **2013**, *7*, 5757–62.

(115) Zhang, X.; Manno, M.; Baruth, A.; Johnson, M.; Aydil, E. S.; Leighton, C. Crossover from nanoscopic intergranular hopping to conventional charge transport in pyrite thin films. *ACS Nano* **2013**, *7*, 2781–9.

(116) Jang, J.; Liu, W.; Son, J. S.; Talapin, D. V Temperature-Dependent Hall and Field-Effect Mobility in Strongly Coupled All-Inorganic Nanocrystal Arrays. *Nano Lett.* **2014**.

(117) Nagaosa, N. Anomalous Hall effect. **2009**.

(118) Le Comber, P. G.; Spear, W. E. Electronic Transport in Amorphous Silicon Films. *Phys. Rev. Lett.* **1970**, *25*, 509–511.

(119) Cohen, M. H.; Fritzsche, H.; Ovshinsky, S. R. Simple Band Model for Amorphous Semiconducting Alloys. *Phys. Rev. Lett.* **1969**, *22*, 1065–1068.

(120) Jeong, K. S.; Tang, J.; Liu, H.; Kim, J.; Schaefer, A. W.; Kemp, K.; Levina, L.; Wang, X.; Hoogland, S.; Debnath, R.; Brzozowski, L.; Sargent, E. H.; Asbury, J. B. Enhanced Mobility-Lifetime Products in PbS Colloidal Quantum Dot Photovoltaics. *ACS Nano* **2011**, *6*, 89–99.

(121) Tang, J.; Kemp, K. W.; Hoogland, S.; Jeong, K. S.; Liu, H.; Levina, L.; Furukawa, M.; Wang, X.; Debnath, R.; Cha, D.; Chou, K. W.; Fischer, A.; Amassian, A.; Asbury, J. B.; Sargent, E. H. Colloidal-quantum-dot photovoltaics using atomic-ligand passivation. *Nat. Mater.* **2011**, *10*, 765–771.

(122) Wang, R. Y.; Feser, J. P.; Lee, J.-S.; Talapin, D. V; Segalman, R.; Majumdar, A. Enhanced thermopower in PbSe nanocrystal quantum dot superlattices. *Nano Lett.* **2008**, *8*, 2283–8.

(123) Kang, M. S.; Sahu, A.; Norris, D. J.; Frisbie, C. D. Size- and temperature-dependent charge transport in PbSe nanocrystal thin films. *Nano Lett.* **2011**, *11*, 3887–92.

(124) Otto, T.; Miller, C.; Tolentino, J.; Liu, Y.; Law, M.; Yu, D. Gate-dependent carrier diffusion length in lead selenide quantum dot field-effect transistors. *Nano Lett.* **2013**, *13*, 3463–9.

(125) Nagpal, P.; Klimov, V. I. Role of mid-gap states in charge transport and photoconductivity in semiconductor nanocrystal films. *Nat. Commun.* **2011**, *2*, 486.

(126) Murphy, J. E.; Beard, M. C.; Nozik, A. J. Time-resolved photoconductivity of PbSe nanocrystal arrays. *J. Phys. Chem. B* **2006**, *110*, 25455–61.

(127) Guglietta, G. W.; Diroll, B. T.; Gaulding, E. A.; Fordham, J. L.; Li, S.; Murray, C.

B.; Baxter, J. B. Lifetime, mobility, and diffusion of photoexcited carriers in ligand-exchanged lead selenide nanocrystal films measured by time-resolved terahertz spectroscopy. *ACS Nano* **2015**, *9*, 1820–8.

(128) Brown, P. R.; Lunt, R. R.; Zhao, N.; Osedach, T. P.; Wanger, D. D.; Chang, L.-Y.; Bawendi, M. G.; Bulović, V. Improved current extraction from ZnO/PbS quantum dot heterojunction photovoltaics using a MoO3 interfacial layer. *Nano Lett.* **2011**, *11*, 2955–61.

(129) Ihly, R.; Tolentino, J.; Liu, Y.; Gibbs, M.; Law, M. The photothermal stability of PbS quantum dot solids. *ACS Nano* **2011**, *5*, 8175–86.

(130) Chang, L.-Y.; Lunt, R. R.; Brown, P. R.; Bulović, V.; Bawendi, M. G. Low-Temperature Solution-Processed Solar Cells Based on PbS Colloidal Quantum Dot/CdS Heterojunctions. *Nano Lett.* **2013**, *13*, 994–9.

(131) Zhao, N.; Osedach, T. P.; Chang, L.-Y.; Geyer, S. M.; Wanger, D.; Binda, M. T.; Arango, A. C.; Bawendi, M. G.; Bulovic, V. Colloidal PbS quantum dot solar cells with high fill factor. *ACS Nano* **2010**, *4*, 3743–52.

(132) Fafarman, A. T.; Koh, W.; Diroll, B. T.; Kim, D. K.; Ko, D.-K.; Oh, S. J.; Ye, X.; Doan-Nguyen, V.; Crump, M. R.; Reifsnyder, D. C.; Murray, C. B.; Kagan, C. R. Thiocyanate-capped nanocrystal colloids: vibrational reporter of surface chemistry and solution-based route to enhanced coupling in nanocrystal solids. *J. Am. Chem. Soc.* **2011**, *133*, 15753–61.

(133) Koh, W.-K.; Saudari, S. R.; Fafarman, A. T.; Kagan, C. R.; Murray, C. B. Thiocyanate-capped PbS nanocubes: ambipolar transport enables quantum dot based circuits on a flexible substrate. *Nano Lett.* **2011**, *11*, 4764–7.

(134) Nag, A.; Kovalenko, M. V; Lee, J.-S.; Liu, W.; Spokoyny, B.; Talapin, D. V Metal-free inorganic ligands for colloidal nanocrystals: S2-, HS-, Se2-, HSe-, Te2-, HTe-, TeS3(2-), OH-, and NH2- as surface ligands. *J. Am. Chem. Soc.* **2011**, *133*, 10612–20.

(135) Emin, D. *Polarons*; Cambridge University Press: New York, 2013.

(136) Emin, D. The Hall Effect in Hopping Conduction. In *The Hall Effect and Its Applications*; Chien, C. L.; Westgate, C. R., Ed.; Plenum Publishing Coorporation: New York, 1980; pp. 281–298.

(137) Pierret, R. F. *Volume VI: Advanced Semiconductor Fundamentals*; Pierret, R. F.; Neudeck, G. W., Ed.; 2nd ed.; Prentice Hall: Upper Saddle River, New Jersey, 2002.

(138) Friedman, L. The Hall Effect in Low Mobility and Amorphous Solids. In *Physics of Disordered Materials*; Adler, D.;Fritzsche, F.; Ovshinsky, S. R., Ed.; Plenum Publishing Coorporation: New York, 1985; pp. 413–422.

(139) Taylor, P.; Comber, P. G. Le; Jones, D. I.; Spear, W. E. Hall effect and impurity conduction in substitutionally doped amorphous silicon. **1977**, 37–41.

(140) Mott, N. F. Conduction in non-crystalline materials. *Philos. Mag.* **1969**, *19*, 835–852.

(141) Baily, S. a.; Emin, D. Transport properties of amorphous antimony telluride. *Phys. Rev. B* **2006**, *73*, 165211.

(142) Friedman, L. Hall conductivity of amorphous semiconductors in the random phase model. *J. Non. Cryst. Solids* **1971**, *6*, 329–341.

(143) Le Comber, P. G.; Jones, D. I.; Spear, W. E. Hall effect and impurity conduction in substitutionally doped amorphous silicon. *Philos. Mag.* **1977**, *35*, 1173–1187.

(144) Emin, D. The sign of the Hall effect in hopping conduction. *Philos. Mag.* **1977**, *35*, 1189–1198.

(145) Emin, D.; Holstein, T. Studies of small-polaron motion IV. Adiabatic theory of the Hall effect. *Ann. Phys. (N. Y).* **1969**, *53*, 439–520.

(146) Lindemuth, J.; Mizuta, S.-I. Hall measurements on low mobility materials and high resistivity materials. In; Eldada, L. A., Ed.; 2011; Vol. 8110, p. 81100I–81100I–7.

(147) Kim, D.; Kim, D.-H.; Lee, J.-H.; Grossman, J. C. Impact of Stoichiometry on the Electronic Structure of PbS Quantum Dots. *Phys. Rev. Lett.* **2013**, *110*, 196802.

(148) Steckel, J. S.; Coe-Sullivan, S.; Bulović, V.; Bawendi, M. G. 1.3μm to 1.55μm Tunable Electroluminescence from PbSe Quantum Dots Embedded within an Organic Device. *Adv. Mater.* **2003**, *15*, 1862–1866.

(149) PDF#98-000-0164

(150) Evers, W. H.; Goris, B.; Bals, S.; Casavola, M.; de Graaf, J.; van Roij, R.; Dijkstra, M.; Vanmaekelbergh, D. Low-dimensional semiconductor superlattices formed by geometric control over nanocrystal attachment. *Nano Lett.* **2013**, *13*, 2317–23.

(151) Baumgardner, W. J.; Whitham, K.; Hanrath, T. Confined-but-Connected Quantum Solids via Controlled Ligand Displacement. *Nano Lett.* **2013**, *13*, 3225–31.

(152) Talapin, D. V.; Black, C. T.; Kagan, C. R.; Shevchenko, E. V.; Afzali, A.; Murray, C. B. Alignment, Electronic Properties, Doping, and On-Chip Growth of Colloidal PbSe Nanowires. *J. Phys. Chem. C* **2007**, *111*, 13244–13249.

(153) Gao, J.; Luther, J. M.; Semonin, O. E.; Ellingson, R. J.; Nozik, A. J.; Beard, M. C. Quantum dot size dependent J-V characteristics in heterojunction ZnO/PbS quantum dot solar cells. *Nano Lett.* **2011**, *11*, 1002–1008.

(154) Wanger, D. D.; Correa, R. E.; Dauler, E. a; Bawendi, M. G. The dominant role of exciton quenching in PbS quantum-dot-based photovoltaic devices. *Nano Lett.* **2013**, *13*, 5907–12.

(155) Choi, J.-H.; Fafarman, A. T.; Oh, S. J.; Ko, D.-K.; Kim, D. K.; Diroll, B. T.; Muramoto, S.; Gillen, J. G.; Murray, C. B.; Kagan, C. R. Bandlike transport in strongly coupled and doped quantum dot solids: a route to high-performance thin-film electronics. *Nano Lett.* **2012**, *12*, 2631–8.

(156) Rosen, E. L.; Buonsanti, R.; Llordes, A.; Sawvel, A. M.; Milliron, D. J.; Helms, B.

a Exceptionally mild reactive stripping of native ligands from nanocrystal surfaces by using Meerwein's salt. *Angew. Chemie* **2012**, *51*, 684–9.

(157) Oh, S. J.; Wang, Z.; Berry, N. E.; Choi, J.; Zhao, T.; Ashley, E.; Paik, T.; Lai, Y.; Murray, C. B.; Kagan, C. R. Supporting Information for Engineering Charge Injection and Charge Transport for High Performance PbSe NC Thin Film Devices and Circuits. 1–23.

(158) Aerts, M.; Sandeep, C. S. S.; Talgorn, E.; Tom, J.; Kinge, S.; Siebbeles, L. D. A.; Houtepen, A. J. Photoconductivity of PbSe Quantum-Dot Solids : Dependence on Ligand Anchor Group and Length. *Mater. Res.* **2012**.

(159) Mora-Sero, I.; Bertoluzzi, L.; Gonzalez-Pedro, V.; Gimenez, S.; Fabregat-Santiago, F.; Kemp, K. W.; Sargent, E. H.; Bisquert, J. Selective contacts drive charge extraction in quantum dot solids via asymmetry in carrier transfer kinetics. *Nat. Commun.* **2013**, *4*, 3272.

(160) Baily, S. a.; Emin, D.; Li, H. Hall mobility of amorphous Ge2Sb2Te5. *Solid State Commun.* **2006**, *139*, 161–164.

(161) Liu, W.; Lee, J.-S.; Talapin, D. V III–V Nanocrystals Capped with Molecular Metal Chalcogenide Ligands: High Electron Mobility and Ambipolar Photoresponse. *J. Am. Chem. Soc.* **2013**, *135*, 1349–1357.

(162) Beloborodov, I. S.; Lopatin, A. V.; Vinokur, V. M.; Efetov, K. B. Granular electronic systems. *Rev. Mod. Phys.* **2007**, *79*, 469–518.

7 LIST OF PUBLICATIONS AS A RESULT OF THIS DISSERTATION WORK

1) **Gaulding, E. A.**; Diroll, B. T.; Goodwin, E. D.; Vrtis, Z. J.; Kagan, C. R.; Murray, C. B. Deposition of Wafer-Scale Single-Component and Binary Nanocrystal Superlattice Thin Films Via Dip-Coating. *Adv. Mater.* 2015.

(2) **Gaulding, E. A.** ; Zhao, T.; Kagan, C. R.; Murray, C. B. Using Temperature Dependent Seebeck Measurements to Investigate How Surface Treatments Tune the Fermi Level in Quantum Dot Films. (To Be Submitted)

(3) **Gaulding, E. A.** ; Vrtis, Z. J.; Fordham, J. L.; Diroll, B. T.; Kagan, C. R.; Murray, C. B. Applying AC Hall and Seebeck Measurements to Probe the Electronic Properties of Lead Selenide Nanocrystal Films. (To Be Submitted)

(4) Goodwin, E. D.*; Straus, D. B.*; **Gaulding, E. A.**; Murray, C. B.; Kagan, C. R. The Effects of Inorganic Surface Treatments on Photogenerated Carrier Mobility and Lifetime in PbSe Quantum Dot Thin Films. *Chem. Phys.* 2015.

(5) Diroll, B. T.; **Gaulding, E. A.**; Kagan, C. R.; Murray, C. B. Spectrally-Resolved Dielectric Functions of Solution- Cast Quantum Dot Thin Films. *Chem. Mater.* 2015

(6) Guglietta, G. W.*; Diroll, B. T.*; **Gaulding, E. A.**; Fordham, J. L.; Li, S.; Murray, C. B.; Baxter, J. B. Lifetime, mobility, and diffusion of photoexcited carriers in ligand-exchanged lead selenide nanocrystal films measured by time-resolved terahertz spectroscopy. *ACS Nano* 2015, *9*, 1820–8.

(7) Gordon, T. R.; Diroll, B. T.; Paik, T.; Doan-Nguyen, V. V. T.; **Gaulding, E. A.**; Murray, C. B. Characterization of Shape and Monodispersity of Anisotropic Nanocrystals through Atomistic X-ray Scattering Simulation. *Chem. Mater.* 2015, *27*, 2502-2506.

(8) Cargnello, M.; Diroll, B. T.; **Gaulding, E. A.**; Murray, C. B. Enhanced energy transfer in quasi-quaternary nanocrystal superlattices. *Adv. Mater.* 2014, *26*, 2419–23.

(9) Oh, S. J.; Berry, N. E.; Choi, J.-H.; **Gaulding, E. A.**; Lin, H.; Paik, T.; Diroll, B. T.; Muramoto, S.; Murray, C. B.; Kagan, C. R. Designing high-performance PbS and PbSe nanocrystal electronic devices through stepwise, post-synthesis, colloidal atomic layer deposition. *Nano Lett.* 2014, *14*, 1559–66.

(10) Paik, T.; Hong, S.-H.; **Gaulding, E. A.**; Caglayan, H.; Gordon, T. R.; Engheta, N.; Kagan, C. R.; Murray, C. B. Solution-processed phase-change VO(2) metamaterials from colloidal vanadium oxide (VO(x)) nanocrystals. *ACS Nano* 2014, *8*, 797–806.

(11) Diroll, B. T.; Gordon, T. R.; **Gaulding, E. A.**; Klein, D. R.; Paik, T.; Yun, H. J.; Goodwin, E. D.; Damodhar, D.; Kagan, C. R.; Murray, C. B. Synthesis of N-Type Plasmonic Oxide

Nanocrystals and the Optical and Electrical Characterization of their Transparent Conducting Films. *Chem. Mater.* 2014, *26*, 4579–4588.

(12) Oh, S. J.; Wang, Z.; Berry, N. E.; Choi, J.-H.; Zhao, T.; **Gaulding, E. A.**; Paik, T.; Lai, Y.; Murray, C. B.; Kagan, C. R. Engineering charge injection and charge transport for high performance PbSe nanocrystal thin film devices and circuits. *Nano Lett.* 2014, *14*, 6210–6.

(13) Diroll, B. T.; Doan-Nguyen, V. V. T.; Cargnello, M.; **Gaulding, E. A.**; Kagan, C. R.; Murray, C. B. X-ray mapping of nanoparticle superlattice thin films. *ACS Nano* 2014, *8*, 12843–50.

(14) Oh, S. J.; Berry, N. E.; Choi, J.-H.; **Gaulding, E. A.**; Paik, T.; Hong, S.-H.; Murray, C. B.; Kagan, C. R. Stoichiometric control of lead chalcogenide nanocrystal solids to enhance their electronic and optoelectronic device performance. *ACS Nano* 2013, *7*, 2413–21.